# Subwavelength Dielectric Grating-based Broadband Reflectors and Narrowband Transmission Filters

by

Justin M. Foley

A dissertation submitted in partial fulfillment
of the requirements for the degree of
Doctor of Philosophy
(Applied Physics)
in the University of Michigan
2014

Doctoral Committee:

Professor Jamie D. Phillips, Chair
Associate Professor Mona Jarrahi, University of California-Los Angeles
Associate Professor Pei-Cheng Ku
Professor Çagliyan Kurdak

# ACKNOWLEDGEMENTS

I have received endless support and insight from colleagues and friends at, and outside of, the University of Michigan. I would like to express a small portion of my gratitude for all of the help I have received over the last five years.

Professor Phillips gave me a position in his lab and the freedom to pursue many different aspects of my project. He provided enough pressure to ensure I continued to publish, while giving me space to develop my techniques and problem solving skills as an independent researcher. More than just a technical advisor, Professor Phillips also involved me in education research. He introduced me to data analytics, as well as more direct studies on information retention in classrooms. He allowed me to work as an Office of Technology Fellow, and supported my participation and leadership of the student chapter of the American Society for Engineering Education at the University of Michigan. For all of the freedom, opportunities, and support he has given me, I will always be grateful.

Professor Mona Jarrahi, Professor P.C. Ku, and Professor Çagliyan Kurdak have devoted significant time over the past three years serving on my committee. Each member provided critical feedback on my results and methods and made suggestions I was able to incorporate into my research. Despite their many other time commitments, they were always available to meet and discuss my research, and they accommodated the timing of both my preliminary examination and oral defense.

Steve Young has been a tremendous colleague who has developed much of our physical understanding of the grating operation. He calculated the grating dispersion

relations, which provided an intuitive explanation for the system operation, and he strongly urged me to consider, and helped me perform, the group theoretical analysis of mode coupling in the grating system. I cannot express enough thanks for how much his insight and prodding helped my progress.

I would also like to thank current and past members of both the Phillips and Guo Groups at the University of Michigan for insightful discussions and feedback. Particularly I would like to thank Chihyu Chen, Anne Itsuno, Alan Teran, Jinyoung Wang, and Connor Field from the Phillips Group, and Jing Zhou, Tau Ling, Yi-Kuei Wu, Cheng Zhang, and Andrew Hollowell from the Guo Group. Without their input and expertise I would not have been able to make the advances I was able to make during my time at Michigan.

Several other individuals from the Maldonado Group made my early years at Michigan rewarding and productive, namely, Jeremy Feldblyum, Michelle Price, Eli Fahrenkrug, Junsi Guo, Azhar Carim, Sean Collins, Sabrina Peczonczyk and Wen Wen. They have all been great friends and important sounding boards for my earliest studies.

Many staff members, as part of the Lurie Nanofabrication Facility and the chemistry department helped tremendously with processing and characterization requirements for this project. I would like to thank Dr. Pilar Herrera Fierro, Dr. Nadine Wang, Matt Oonk, Russ Clifford, Brian Armstrong, and Kevin Owen for all of their help with fabrication. In the chemistry department, I would like to thank Dr. James Windak and Roy Wentz for their characterization support.

The road to receiving my doctorate would have been more tumultuous and painstaking without the incessant support of Christina Jones. She read every paper, every cover letter, and every essay required during my doctoral work. Furthermore she was understanding of the demands on my time, and she supported me when difficult decisions had to be made. I am grateful for her companionship and help, which she

is always willing to offer.

Finally, I would like to thank my parents for giving me every opportunity to succeed in many different aspects of life. They taught me to take pride in my work and that perseverence is often rewarded. They serve as excellent role models for how to be supportive parents, where they have provided a nurturing environment and endless trust.

# TABLE OF CONTENTS

**ACKNOWLEDGEMENTS** . . . . . ii

**LIST OF FIGURES** . . . . . vii

**LIST OF TABLES** . . . . . xiii

**ABSTRACT** . . . . . xiv

**CHAPTER**

**I. Introduction and Background** . . . . . 1

1.1 Introduction . . . . . 1
1.1.1 Long-wavelength Infrared Imaging . . . . . 2
1.1.2 Dielectric-based Optical Elements . . . . . 4
1.2 Background . . . . . 5
1.2.1 Fabry-Pérot Etalons . . . . . 5
1.2.2 Distributed Bragg Reflectors . . . . . 8
1.2.3 High Contrast Gratings . . . . . 11
1.2.4 Photonic Crystal Slabs and Guided Mode Resonance 14
1.2.5 Dielectric Grating-based Filtering Capabilities . . . 19
1.2.6 Metallic Grating-based Filtering Capabilities . . . . 19
1.3 Thesis Organization . . . . . 20

**II. Methods** . . . . . 23

2.1 Computational Analysis . . . . . 23
2.1.1 Structure Optimization . . . . . 27
2.1.2 Modal Analysis . . . . . 29
2.2 Fabrication Procedures . . . . . 30
2.2.1 Mask Design . . . . . 30
2.2.2 Photolithography . . . . . 31
2.2.3 Reactive Ion Etching and Hydrofluoric Acid Suspension 32
2.3 Fourier Transform Infrared Spectroscopic Characterization . . 33

2.3.1 Experimental Setup . . . . . 36

**III. Normal Incidence Broadband Reflectors** . . . . . 40

3.1 $Si/SiO_2$ Grating System . . . . . 41
3.2 Suspended Silicon Grating System . . . . . 46
3.3 Summary . . . . . 50

**IV. Oblique Incidence Broadband Reflector** . . . . . 51

4.1 Polarization Dependence . . . . . 53
4.2 Finite Element Simulation Analysis . . . . . 54
4.3 Fabrication Tolerances . . . . . 55
4.4 Summary . . . . . 56

**V. Group Theoretical Analysis of Mode Coupling and its Application to Transmission Filtering in Dielectric Gratings** . . . . 58

5.1 Group Theoretical Analysis . . . . . 60
5.2 Transmission Filtering Capabilities . . . . . 65
5.2.1 Fano Resonance Fitting . . . . . 69
5.3 Summary . . . . . 70

**VI. Experimental Demonstration of Transmission Filters** . . . . . 72

6.1 Angular Dependence . . . . . 76
6.2 Quality Factor Analysis . . . . . 79
6.3 Wavelength Selection . . . . . 82
6.4 Material Absorption . . . . . 83
6.5 Further Discussion . . . . . 84
6.6 Summary . . . . . 85
6.7 Filter Appendix . . . . . 87

**VII. Future Work and Conclusions** . . . . . 92

7.1 Future Studies . . . . . 92
7.1.1 Improved Characterization Capabilities . . . . . 92
7.1.2 Normal Incidence Filters . . . . . 93
7.1.3 Polarization Independent Broadband Reflectors . . . 94
7.1.4 System Integration . . . . . 95
7.2 Conclusion . . . . . 96

**BIBLIOGRAPHY** . . . . . 98

# LIST OF FIGURES

**Figure**


1.1 Atmospheric transmittance in the mid-infrared with overlaid emissivity of a blackbody at 300 K. . . . . 2

1.2 Hypothetical spectra for a forest, a mountain and an ocean, collected using a hyperspectral imaging system. . . . . 3

1.3 a) A schematic of a Fabry-Pérot etalon composed of two mirrors with reflectivities $R_1$ and $R_2$ separated by distance $d$. b) Fabry-Pérot etalon transmittance with $d = 5$ $\mu$m and varying mirror reflectivity, $R_1 = R_2 = R$. The two transmission bands are designated by (*) and (**). c) Standing wave configurations responsible for filtering bands of b). . . . . 6

1.4 Fabry-Pérot etalon wavelength selection with $R = 95\%$ as $d$ is varied between 4 and 6 $\mu$m. . . . . 7

1.5 DBR structure and response. a) High- and low-index bilayer with thicknesses and material properties defined. b) Schematic of a 10 bilayer DBR. c) Associated 10 bilayer DBR response using $n_{\text{high}}/n_{\text{low}} = 3.42/1.5$ with scales from 0-100% and 99-100%. . . . . 8

1.6 DBR schematics and associated responses for stacks of a) 0, b) 1, c) 5, and d) 10 bilayers of $Si/SiO_2$: $n_{\text{Si}}/n_{\text{SiO2}} = 3.42/1.5$. . . . . 9

1.7 Index contrast dependence on DBR response for $n_{\text{low}} = 1.5$ and $1.5 < n_{\text{high}} < 3.5$ shown for a) reflectance from 0 to 100% and b) reflectance greater than 99%. . . . . 10

1.8 High contrast grating schematic with dimensions, material properties and exciting field defined. . . . . 11

1.9 High contrast grating schematic used by Karagodsky *et al.* to solve for the modes responsible for the broadband reflectance response.[53] 13

1.10 a) Slab waveguide schematic operating under TM polarization conditions and b) the dispersion curves of a symmetric slab waveguide where $TM_{1e}$ and $TM_{1o}$ are the first even and odd solutions to the governing transcendental equations and $TM_{2o}$ is the second odd solution to the transcendental equations, where even is defined with respect to the mirror reflection across the $xz$-plane. . . . . 16

1.11 a) Slab waveguide dispersions represented in reduced-zone configuration. The intersections between the red light line and the dispersion curves ((i), (ii) and (iii)) indicate where coupling between the guided modes of the waveguide and incident light may occur. b) The dispersion relations for a silicon grating. . . . . 17
1.12 The effects of coupling strength on a resonance bandwidth. . . . . 18
2.1 The index of refraction ($n$) and extinction coefficient ($\kappa$) for silicon and $SiO_2$ from literature.[87] . . . . . 24
2.2 Grating schematic with computational domain indicated. The grating is defined by its period $\Lambda$, layer thicknesses ($t_{grating}$ and $t_{low}$), layer indices of refraction ($n_{grating}$, $n_{low}$, and $n_{substrate}$), and FF (defined as the ratio of the width of the grating ($w$) to the period ($\Lambda$)). The computational domain includes periodic boundary conditions (red) and port boundary conditions (green) for excitation and extraction of the reflectance $|S_{11}|^2$ and transmittance ($|S_{21}|^2$). . . . . 25
2.3 Representative COMSOL data showing a) a contour plot of extracted transmittance data, b) line plots of associated transmittance data, and c) $H_z$ field profile. . . . . 27
2.4 Illustration of the iterative optimization procedure used to design the gratings. The series corresponds to the optimization of a germanium grating on a ZnSe substrate. . . . . 28
2.5 Representative TM modal analysis results for a Si/air grating. . . . 30
2.6 Photolithography mask design with grating dimensions. a) Mask layout. b) portion of mask showing dimensions of each grating. c) Fabricated matrix element. . . . . 31
2.7 SEM micrographs showing He/HBr reactive ion etch profiles. a) Etch rate dependence on open area. Smaller open areas ($\Lambda = 4.6$ $\mu$m) exhibit over etching while larger periods ($\Lambda = 5.0$ $\mu$m and $\Lambda = 5.5$ $\mu$m) exhibit vertical etch profiles. b) Sidewall roughness. . . . . 32
2.8 SEM images of suspended silicon structures. . . . . 32
2.9 Michelson interferometer schematic. . . . . 34
2.10 The conceptual operation of an FTIR. a) The requirements for constructive and destructive interference and the resulting intensity measured by the detector and b) the interferograms of monochromatic and polychromatic light and their resulting $I(\omega)$ spectra. . . . . 35
2.11 Pictorial representation of commercial FTIR spectrometer with microscope attachment operating in reflectance mode with different components of the general characterization method. . . . . 37
2.12 Incident light configurations for reflectance and transmittance measurements. . . . . 38
3.1 Schematic illustration of the dielectric grating geometry with definition of incident field polarization. . . . . 40
3.2 a) Simulated reflectance results of the $Si/SiO_2$ grating with $t = 3.4$ $\mu$m, $h = 3.9$ $\mu$m, $\Lambda = 5.1$ $\mu$m varying the fill factor, and b) the corresponding reflectance spectrum for FF=72%. . . . . 41

3.3 SEM micrograph of fabricated $Si/SiO_2$ grating. . . . . 42
3.4 Polarization dependent FTIR reflectance of a $Si/SiO_2$ grating with dimensions: $t = 3.9$ $\mu$m, $h = 3.9$ $\mu$m, $\Lambda = 5$ $\mu$m and FF=72%. . . . 43
3.5 Measured and simulated reflectance for a) unpatterned SOI wafer and b) patterned $Si/SiO_2$ grating. . . . . 44
3.6 Re-optimization of the $Si/SiO_2$ grating integrating complex indices of refraction for the materials. . . . . 45
3.7 A suspended grating schematic including a) a cross section with dimensions and computational domain defined and b) a three-dimensional schematic with field and incident angle defined. . . . . 46
3.8 a) Reflectance profile dependence on the height of the grating and b) the corresponding optimized normal incidence response: $\Lambda = 5$ $\mu$m, $t = 3$ $\mu$m, $h = 4$ $\mu$m, and $FF = 72\%$. . . . . 47
3.9 a) Fabricated single matrix element. b) Transverse cross sectional SEM micrographs of structures with over etched and optimally etched profiles resulting from open area etch dependence. c) Longitudinal oblique incident cross section of fabricated suspended structure. d) Sidewall roughness with striation pitch <100 nm. . . . . 48
3.10 Experimental demonstration of broadband reflector at normal incidence for TM polarization and the accompanying response for TE polarization. . . . . 49
4.1 A three-dimensional schematic of a suspended silicon grating with field and incident angle ($\theta$) defined. . . . . 51
4.2 Polarization dependent field response of a suspended silicon grating with dimensions: $\Lambda = 4.15$ $\mu$m, $t = 3.05$ $\mu$m, $h = 4.1$ $\mu$m, and $FF = 61\%$. . . . . 52
4.3 Experimental polarization dependent field response of the suspended silicon grating with 0° and 90° corresponding to TE and TM polarizations, respectively and dimensions: $\Lambda = 4.15$ $\mu$m, $t = 3.05$ $\mu$m, $h = 4.1$ $\mu$m, and $FF = 61\%$ for a) the LWIR spectrum and b) the maximum deviation within the LWIR at 9.3 $\mu$m. . . . . 53
4.4 Comparison between experiment and as-built simulations at $\theta = 15°$ oblique incidence for a grating with: $\Lambda = 4.15$ $\mu$m, $t = 3.05$ $\mu$m, $h = 4.1$ $\mu$m, and $FF = 61\%$. . . . . 54
4.5 Simulated angular dependence of the grating reflectance with a) a contour plot from 0 to 20°, and b) line plots at select angles. . . . . 55
4.6 a) Representative grating profiles used for over etching analysis. b) Field response dependence on the over etched radius profile ($r/w$). . 56
4.7 a) Simulated and b) experimental grating reflectance with changing fill factor. . . . . 57
5.1 a) Grating schematic and b) its corresponding Brillouin zone with incident fields, dimensions, and material properties defined. . . . . 59

5.2 TM dispersion relations and field profiles for a grating with $\frac{t}{\Lambda} = 0.6$, $FF = 0.72$, $\epsilon_g = 11.7$, and $\epsilon_s = 1$. a) The dispersion relations include even (blue) and odd (green) bands with respect to a mirror reflection across the $xz$-plane. Solid bands were calculated using finite element modal analysis and dashed bands were estimated from scattering analysis. The modes at $k_x = 0$ are labeled with their Γ-point ($D_{2h}$ symmetry) irreducible representations and band definitions. The light cone is shown in light gray. b) TM mode field profiles at $k_x = 0$ with a black line indicating the boundary between high and low permittivity regions. Below: grating simulation element, and directions defined. . . . . 61

5.3 TE dispersion relations and select field profiles for a grating with $\frac{t}{\Lambda} = 0.6$, $FF = 0.72$, $\epsilon_g = 11.7$, and $\epsilon_s = 1$. a) The dispersion relations include even (blue) and odd (green) bands with respect to a mirror reflection across the $xz$-plane. The modes at $k_x = 0$ are labeled with their Γ-point ($D_{2h}$ symmetry) irreducible representations and band definitions. The light cone is shown in light gray. b) TE mode field profiles at $k_x = 0$ with a black line indicating the boundary between high and low permittivity regions. Below: grating simulation element, and directions defined. . . . . 64

5.4 Simulated grating transmittance profile at normal and off-normal incidence. $k_x = 0$, $|k_x| > 0$, and $|k_z| > 0$ correlates to Points I, II, and III, respectively. The top scale shows increasing $\theta$ and $\varphi$ directions corresponding to $|k_x| > 0$, and $|k_z| > 0$, respectively. Transmission bands are labeled with the mode associated with the resonance. . . 66

5.5 Simulated response of the optimized suspended silicon grating: $\Lambda = 5$ $\mu$m, $FF = 72\%$, $t = 3$ $\mu$m and $h = 4$ $\mu$m with a) a contour plot of transmittance as a function of increasing angle from normal, $\theta$ and b) respective line plots at normal incidence and $\theta = 5°$, with transmitted bands designated (i) and (ii). c) Magnetic field profiles, $H_z$, on each resonance showing the supported modes at $\theta = 5°$. . . . . 68

5.6 TM resonances fit with Fano-lineshapes at 5° from normal incidence. 70

6.1 SEM micrographs of a suspended silicon grating with $\Lambda = 5.1$ $\mu$m, $t = 2.85$ $\mu$m, $h = 4.05$ $\mu$m and $FF = 76\%$ in a) cross sectional view, b) oblique incidence view, and c) plan view. . . . . 73

6.2 Experimental and associated simulated transmittance of a grating with various incident wave configurations. The as-built dimensions were $\Lambda = 4.9$ $\mu$m, $t = 2.85$ $\mu$m, $h = 4.05$ $\mu$m and $FF = 72\%$. Broadband reflectance, TM selective filtering, TE selective filtering and mixed TE and TM filtering associated with the incident wave vector at various points in the Brillouin zone: Point I ($\theta = \varphi = 0°$, Point II ($\theta = 7°$, $\varphi = 0°$), Point III ($\theta = 0°$, $\varphi = 14°$), and Point IV ($\theta = 7°$, $\varphi = 14°$), respectively. . . . . 74

6.3 Angular dependence of transmission filtering capabilities. The response is shown for (top-left) $\theta$ increasing with $\varphi = 0°$, (top-right) $\theta > 0°$ with increasing $\varphi$, (bottom-right) $\theta$ decreasing with $\varphi > 0°$, and (bottom-left) $\theta = 0°$ with $\varphi$ decreasing. The as-built dimensions were $\Lambda = 4.9$ $\mu$m, $t = 2.85$ $\mu$m, $h = 4.05$ $\mu$m and $FF = 0.72$. . . . . 77
6.4 Transmission filtering response illustrating the FWHM, peak wavelength and extracted quality factor at a) $\theta = 10.5°$ and $\varphi = 0°$ and b) $\theta = 0°$ and $\varphi = 14°$ for a grating with dimensions $\Lambda = 4.9$ $\mu$m, $t = 2.85$ $\mu$m, $h = 4.05$ $\mu$m and $FF = 0.72$. . . . . 78
6.5 a) Peak wavelength and b) quality factor dependence on incident angle for transmission bands associated with $TM_1^-$ and $TE_2^-$ modes. The corresponding simulated parameters are also included for the as-characterized parameters: $\theta = 7°$ and $\varphi = 14°$ and structure dimensions: $\Lambda = 4.9$ $\mu$m, $t = 2.85$ $\mu$m, $h = 4.05$ $\mu$m and $FF = 0.72$. . . . . 79
6.6 Effects of angular extent ($\theta \pm 3°$) allowed by iris. The experimental demonstration at $\theta = 9°$ is shown with the corresponding simulated response at a) $\theta = 6°$, b) $\theta = 9°$, and c) $\theta = 12°$ for a grating with dimensions: $\Lambda = 4.9$ $\mu$m, $t = 2.85$ $\mu$m, $h = 4.05$ $\mu$m and $FF = 0.72$. 80
6.7 Simulated contour plots with experimental peak wavelength locations overlaid (*) for suspended silicon gratings with $FF = 72\%$, $t = 2.85$ $\mu$m and $h = 4.05$ $\mu$m and 4.7 $\mu$m$\leq \Lambda \leq 5.1$ $\mu$m with (left) $\theta = 7°$ and (right) $\varphi = 14°$. . . . . 82
6.8 Comparison of wavelength selection between $TM_1^-$ and $TE_2^-$ associated transmission bands as a function of grating period. The grating dimensions were $FF = 72\%$, $t = 2.85$ $\mu$m and $h = 4.05$ $\mu$m and 4.7 $\mu$m$\leq \Lambda \leq 5.1$ $\mu$m with data collected at $\theta = 9°$ and $\varphi = 14°$ for the TM and TE datasets, respectively. . . . . 83
6.9 Simulated peak transmittance dependence on extinction coefficients for the grating and the grating with underlying substrate. The simulations were performed on a grating with: $\Lambda = 4.9$ $\mu$m, $t = 2.85$ $\mu$m, $h = 4.05$ $\mu$m and $FF = 0.72$ and an angle of $\theta = 7°$. . . . . 84
6.10 Line plots for TM modes increasing the incident angle $\theta$ with extracted peak transmittance, peak wavelength, resonance quality factor, and resonance FWHM. . . . . 87
6.11 Line plots for TE modes increasing the incident angle $\varphi$ with extracted peak transmittance, peak wavelength, resonance quality factor, and resonance FWHM. . . . . 88
6.12 Line plots for TM modes at $\theta = 9°$ for gratings with different periods with extracted peak transmittance, peak wavelength, resonance quality factor, and resonance FWHM. . . . . 89
6.13 Line plots for TE modes at $\varphi = 14°$ for gratings with different periods with extracted peak transmittance, peak wavelength, resonance quality factor, and resonance FWHM. . . . . 90

6.14 Experimental and simulated responses at $\theta = 9^\circ$ with peak experimental wavelength indicated. . . . . 91
6.15 Experimental and simulated responses at $\varphi = 14^\circ$ with peak experimental wavelength indicated. . . . . 91
7.1 Possible cross-sections that break the $x$-symmetry of the grating to enable normal incidence filtering and accompanying simulated transmittance. The simulated grating dimensions were $\Lambda = 5$ $\mu$m, $t = 3$ $\mu$m, $h = 4.0$ $\mu$m and $FF = 0.72$. . . . . 94
7.2 a) A schematic of a prospective two-dimensional grating reflector and b) corresponding preliminary reflectance for an InP two-dimensional grating with dimensions $\Lambda = 1.2$ $\mu$m, $t = 420$ nm, and $r = 400$ nm.[19] 95
7.3 A schematic of possible filter integration in a focal plane array. . . . 96

# LIST OF TABLES

**Table**


5.1 $D_{2h}$ character table corresponding to the Γ-point of the grating's reciprocal lattice. . . . . 60

5.2 a) $C_{2v}^{y}$ character table and b) the compatibility relations between Point I and the Γ-point. . . . . 62

5.3 a) $C_{s}^{xy}$ character table and b) the compatibility relations between Point II and the Γ-point. . . . . 63

5.4 a) $C_{s}^{yz}$ character table and b) the compatibility relations between Point III and the Γ-point. . . . . 63

5.5 Summary of the allowable mode coupling for a TM polarized plane wave with various incident wave vectors. 'X' indicates relatively strong coupling, while 'x' indicates relatively weak coupling. . . . . 65

# ABSTRACT

Subwavelength Dielectric Grating-based Broadband Reflectors and Narrowband Transmission Filters

by

Justin M. Foley

Chair: Jamie D. Phillips

Optical components including lenses, filters, and mirrors are ubiquitously used in society, from applications that include the computers we use to the automobiles we drive. While visible spectrum optical elements are generally well developed and provide adequate means of achieving desired spectral response, similar elements operating in the long-wavelength infrared (LWIR, 8-15 $\mu$m) have not seen the same advancement, despite having large technological implications. The LWIR is extensively used in thermal imaging, with applications including remote sensing and surveillance. The next generation of thermal imaging systems includes hyperspectral capabilities where the electromagnetic spectrum of each pixel in a viewing plane is collected. This ability can increase object discrimination in surveillance and enable spectroscopic capabilities in remote sensing. Unfortunately, many systems are expensive to produce and they possess cumbersome form factors.

This dissertation includes investigations on infrared mirrors and filters for next generation thermal imaging and spectrometer-on-a-chip applications operating in the LWIR spectral region. Using the concept of high index-contrast gratings, which have

been studied in the near-infrared (0.75-1.4 $\mu$m) spectrum, we have demonstrated broadband reflectors and narrowband transmission filters using Si/$SiO_2$ and Si/air grating structures. Using finite element method simulations, photolithography and Fourier transform infrared spectroscopy, we designed, fabricated, characterized and analyzed structure response.

We provide the first demonstration of broadband reflectance in the LWIR using a high contrast grating, with the Si/$SiO_2$ grating exhibiting reflectance greater than 70% between 13 and 16 $\mu$m. We subsequently developed a suspended Si/air grating to eliminate the lossy $SiO_2$ layer, which was limiting the reflectance of the Si/$SiO_2$ system. LWIR broadband reflectors operating at normal and oblique incidence (15°) with reflectances greater than 85% and 90%, respectively, are demonstrated.

These studies are followed with a group theoretical analysis showing strong plane wave coupling to guided modes supported by the grating is responsible for the broadband reflectance at normal incidence. We show that other modes are symmetry protected at normal incidence, preventing plane wave coupling. Off-normal incidence relaxes the selection rules and enables weak coupling to these previously protected modes. We use this analysis to predict narrowband transmission filtering capabilities by coupling to transverse magnetic and transverse electric mode sets supported by the grating.

Finally, we experimentally demonstrate and characterize narrowband transmission filtering capabilities based on the optimized broadband reflector and the group theoretical analysis. We use finite element modal analysis to determine the grating dispersion relations and show the transmission bands agree with the grating's supported mode frequencies. Furthermore, the filtered wavelength is demonstrated to predictably change with the grating period, making it attractive for possible hyperspectral imaging applications.

# CHAPTER I

# Introduction and Background

## 1.1 Introduction

As computation is pushed to faster speeds and smaller form factors, and imaging systems are pressed to achieve greater resolution, innovation and the breaking of conventional paradigms becomes a necessity. Electrical interconnects are beginning to limit computational speeds, conventional patient and environmental diagnostics are limited by cumbersome and time-consuming analyses, and infrared imaging is often limited to intensity-based capabilities, losing much important information for surveillance and remote sensing applications. To mitigate these shortcomings, new optical elements and optical engineering technologies must be developed.

We are now approaching computational speeds that are limited by the electrical interconnects between components. To overcome this barrier, intensive effort has focused on integrating optical elements that promise faster system response.[1] However, this integration requires significant innovation to incorporate such elements into conventional fabrication flow, as well as to ensure their reliable operation.

Chemical and biological system monitoring similarly requires significant advances to improve diagnostic and characterization capabilities that are not confined to designated laboratories. The requirement of sending samples to a laboratory to be analyzed severely limits the real-time diagnostic capabilities needed in patient care[2,3] as well

as environmental monitoring.[4,5] However, developing spectrometers and other characterization equipment that are cost-effective while being portable requires imaging and detection capabilities that have yet to be developed.

Finally, increasing the resolution and achieving advanced capabilities in imaging systems requires reducing the pixel size while maintaining or improving the spectral selectivity of each pixel. Adaptive focal plane arrays,[6,7] and hyperspectral imaging capabilities[7–9] are attractive advancements to conventional imaging systems that could augment their utility in many applications,[9–12] yet their development relies on engineering novel optics.

### 1.1.1 Long-wavelength Infrared Imaging

Infrared detection and imaging is used in many industries including food processing, remote sensing, and surveillance, among others.[8,9,13–16] The long wavelength infrared (LWIR, 8-15 $\mu$m) spectral region, in particular, is used in remote sensing and surveillance as there is little atmospheric absorption within this range, as illustrated in Figure 1.1. Much of the infrared spectrum is absorbed by different constituents in the atmosphere including $CO_2$ and $H_2O$, among others. Between 8 and 15 $\mu$m, however, there is little absorption within the atmosphere. Consequently, this wavelength range is often used in surveillance and remote sensing applications, where imaging through clouds may be necessary. Overlaid on the transmittance is the emissivity of

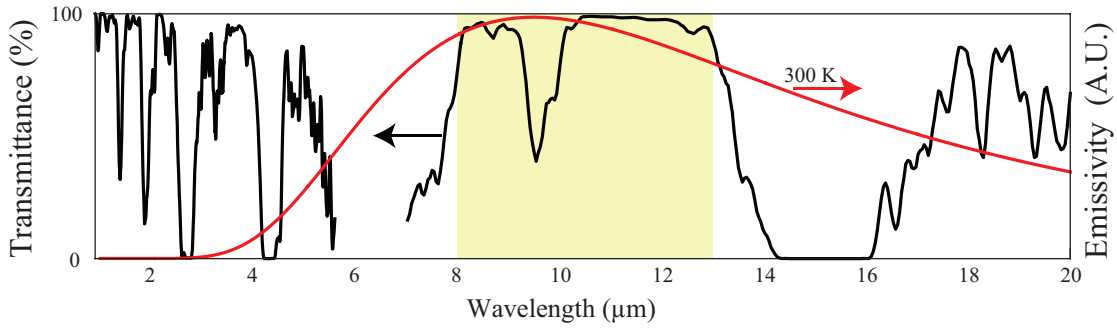


Figure 1.1: Atmospheric transmittance in the mid-infrared with overlaid emissivity of a blackbody at 300 K.

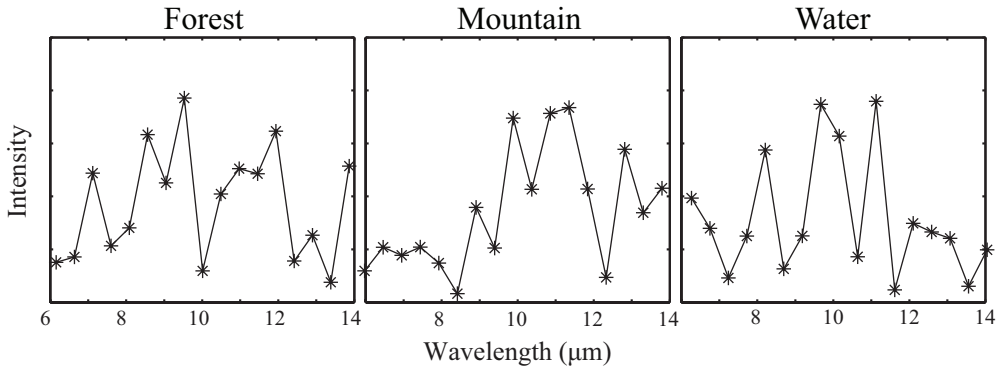


Figure 1.2: Hypothetical spectra for a forest, a mountain and an ocean, collected using a hyperspectral imaging system.

a blackbody at 300 K, or room temperature. The peak wavelength falls within the LWIR, which further motivates its use for studying human activities.

Emerging imaging systems, including those with hyperspectral capabilities[9,13] provide spectral information beyond conventional intensity-based imaging. In this method the electromagnetic spectrum of each point within a viewing plane is measured, providing a fingerprint for each. These spectra enable better discrimination between areas and objects, yielding more accurate characterization and surveillance capabilities. A series of hypothetical spectra is shown in Figure 1.2 to illustrate how hyperspectral "fingerprints" enable differentiation between objects. These three spectra have the same integrated intensity across the LWIR spectrum, which would result in identical images from an intensity-based imaging system. Introducing wavelength selectivity provides spectra that are unique from each other, leading to better characterization of imaged objects.

To obtain the spectral information necessary to construct each object's spectrum, narrowband filters are required. Improving filtering capabilities by reducing the filter bandwidth promotes more precise measurement of the electromagnetic signatures for objects, which can further enhance discrimination. However, LWIR spectral filtering is challenging due to inefficient absorption-based filters and the intensive fabrication requirements to produce interference-based filters such as Fabry-Pérot etalons. New

platforms for achieving these filtering capabilities are thus needed.

### 1.1.2 Dielectric-based Optical Elements

All of the systems mentioned above rely on efficient spectral filtering capabilities at the chip or even pixel level. For computing, the number of bands within the telecommunications window dictates the achievable speed of a system,[1] while chip-level spectral filters may enable spectrometer-on-a-chip applications and low-cost hyperspectral imaging capabilities.[7,11,17] However, to demonstrate such advancements, traditional optics based on lossy materials, including metals, are unattractive for achieving desired filtering capabilities.

Dielectric-based optical elements can be nearly lossless, and hence can improve filtering response. Fabry-Pérot etalons incorporating dielectric mirrors, including distributed Bragg reflectors (DBR), enable real-time wavelength tuning that can be used for spectroscopy and possibly computing applications. While DBRs are extensively used in near-infrared and visible spectral regions to achieve broadband reflectance and filtering capabilities, fabricating such structures in the mid-infrared is much more challenging. For LWIR sensing, for instance, DBR stacks require individual layer thicknesses of 1 $\mu$m or greater, where surface roughness, wafer uniformity, and wafer curvature become major concerns for the film deposition.

Subwavelength gratings provide further capabilities for broadband reflection,[18,19] spectral filtering,[20,21] and general spectral shaping.[22] These elements have been demonstrated in the near-infrared spectral range and applied to vertical cavity surface emitting lasers.[23] Their use in mid-infrared applications is similarly desired.[6,24] Previously, broadband reflectors have been utilized in Fabry-Pérot etalons to achieve adaptive infrared focal plane arrays with tunable narrow-band spectral selectivity.[6,7,25] In this dissertation, these demonstrations form the foundation for developing optical elements that operate in the mid-infrared spectral region, where surveillance, remote

sensing, thermal imaging, and other applications operate.

## 1.2 Background

The following sections introduce relevant background for understanding the current limitations in transmission filtering capabilities in the LWIR, and the future demonstrations using dielectric gratings.

### 1.2.1 Fabry-Pérot Etalons

A propagating electromagnetic wave incident on an interface between materials with different refractive indices is partially reflected by and partially transmitted across the interface.[26,27] At normal incidence the reflected intensity is

$$R = r^2 = \left| \frac{(n_1 - n_2)}{(n_1 + n_2)} \right|^2 , \tag{1.1}$$

where $n_1$ and $n_2$ are the indices of refraction for the two materials composing either side of the interface. The relationship between the reflectance ($R$) and the transmittance ($T$) is

$$R + T + L = 100\% , \tag{1.2}$$

where $L$ is any loss associated with the system, including absorption. If instead, the incident propagating wave meets two parallel interfaces, there will be reflected and transmitted components from each interface that will result in interference between the various propagating waves.

Dichroic filters exploit the interference between reflected and transmitted waves to achieve spectral filtering capabilities. A Fabry-Pérot etalon is a common filtering cavity composed of two mirrors or interfaces with reflectivity $R_1$ and $R_2$ that are separated by a distance $d$, as shown in Figure 1.3a. When the distance $d$ is equal

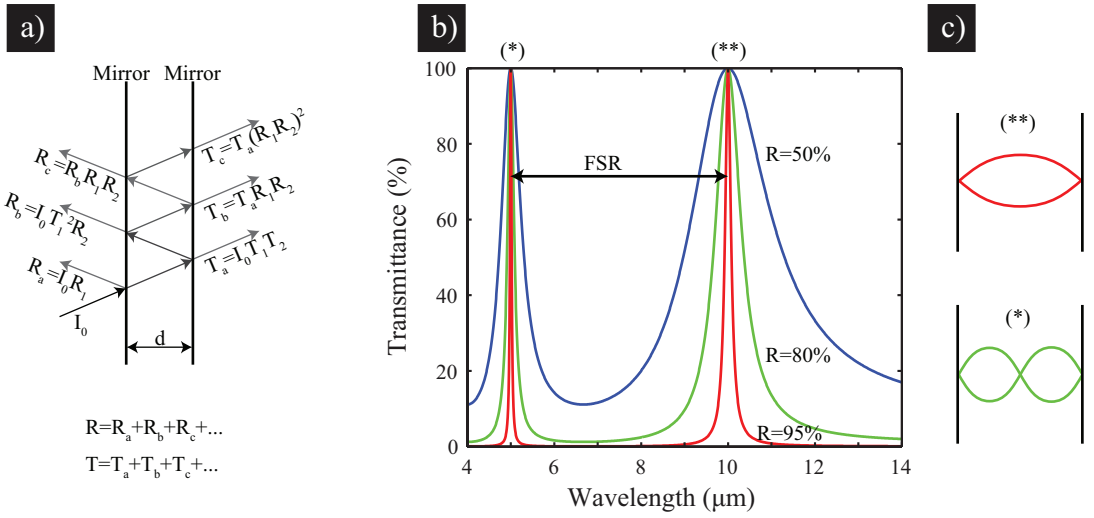


Figure 1.3: a) A schematic of a Fabry-Pérot etalon composed of two mirrors with reflectivities $R_1$ and $R_2$ separated by distance $d$. b) Fabry-Pérot etalon transmittance with $d = 5$ $\mu$m and varying mirror reflectivity, $R_1 = R_2 = R$. The two transmission bands are designated by (*) and (**). c) Standing wave configurations responsible for filtering bands of b).

to an integer multiple of half wavelengths ($d = m\frac{\lambda}{2}$, $m = 1, 2, 3, ..$), a standing wave is formed within the cavity that enhances the field intensity and results in complete transmission of the light through both mirrors.

One can solve for the transmittance and reflectance profiles associated with a Fabry-Pérot etalon by accounting for the reflected and transmitted components of light at each mirror interface (Figure 1.3a), where the phase must also be tracked. The total phase accumulated as the wave propagates between the two mirrors at normal incidence is

$$\delta = k_0 d = \frac{2\pi}{\lambda} d \ , \tag{1.3}$$

where $k_0 = \frac{2\pi}{\lambda}$ is the free space propagation constant. The resulting transmittance after summing all of the individual components is

$$T = \frac{(1-R)^2}{1 + R^2 - 2R\cos\delta} \ , \tag{1.4}$$

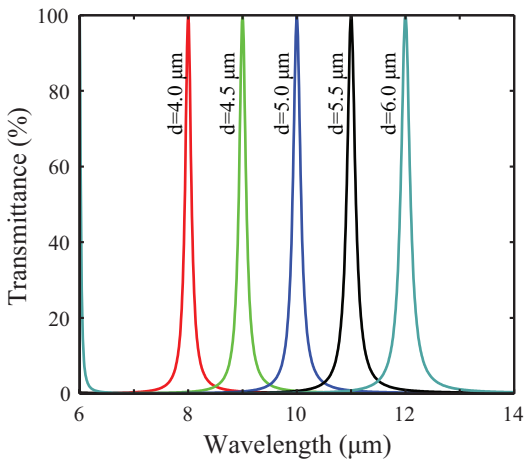


Figure 1.4: Fabry-Pérot etalon wavelength selection with $R = 95\%$ as $d$ is varied between 4 and 6 $\mu$m.

where $R_1 = R_2 = R$ is the reflectance of the mirrors. This response is illustrated in Figure 1.3b for a Fabry-Pérot etalon with $d = 5$ $\mu$m. The effects of changing the mirror reflectivity are included to illustrate the improvement in filtering capabilities when the mirror reflectivity is increased. The two resonances, designated (*) and (**), correspond to full-wavelength and half-wavelength standing waves, respectively, as shown in Figure 1.3c. The spectral distance between the transmittance peaks is called the free spectral range (FSR) and is given, in the case of a Fabry-Pérot etalon, by

$$FSR = \frac{\lambda_0^2}{2d + \lambda_0} \ , \tag{1.5}$$

where $\lambda_0$ is the wavelength of an adjacent transmission peak. This range dictates the bandwidth over which such a filter can operate without introducing a second peak.

Wavelength selection using a Fabry-Pérot etalon is accomplished by varying $d$, as shown in Figure 1.4. Although only five transmission bands are depicted, real-time manipulation of $d$ using electrostatic actuation can lead to continuous wavelength selection across the FSR. Fabry-Pérot etalons have been realized in mid-infrared filtering using both static and dynamic cavities.[7,8,11,17,24,28]

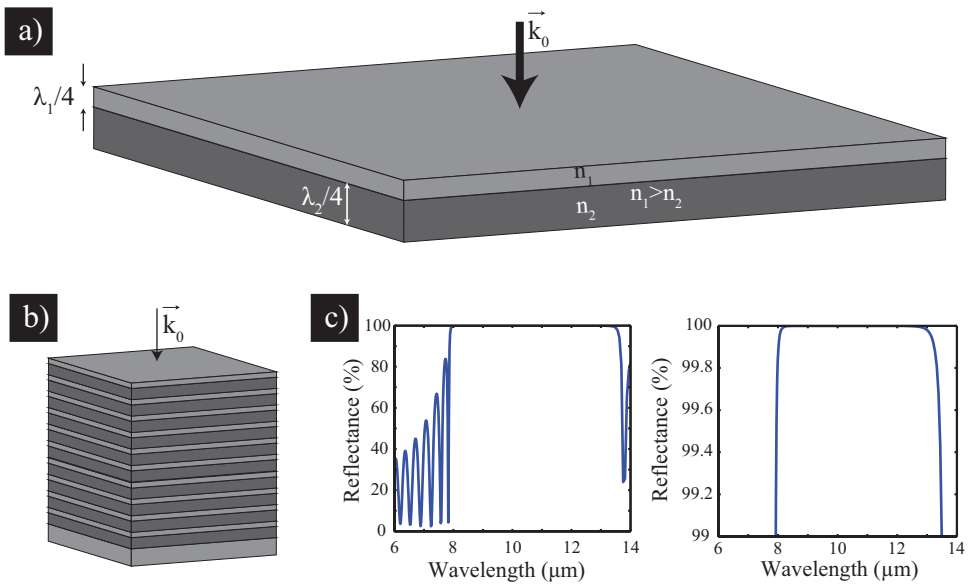


Figure 1.5: DBR structure and response. a) High- and low-index bilayer with thicknesses and material properties defined. b) Schematic of a 10 bilayer DBR. c) Associated 10 bilayer DBR response using $n_{\text{high}}/n_{\text{low}} = 3.42/1.5$ with scales from 0-100% and 99-100%.

One of the main requirements for an efficient Fabry-Pérot filter is the use of broadband, highly reflective mirrors. DBRs have been developed to achieve very broadband reflectance greater than 99% that overcomes the limitations of conventional metallic mirrors.

### 1.2.2 Distributed Bragg Reflectors

A DBR, or quarter-wave stack, is composed of alternating layers of high ($n_{\text{high}}$) and low ($n_{\text{low}}$) refractive index materials, each with thickness $\lambda_m/4$, where $\lambda_m = \frac{\lambda_0}{n_m}$ is the wavelength of light within material $m$. Figure 1.5 shows a schematic of a DBR with an accompanying 10 bilayer simulated response. The response exhibits reflectance greater than 99% over a broad spectral range, which is attractive for many cavity applications.[24,29,30] The resulting broadband reflectance is a consequence of destructive interference for forward propagating waves,[31] which can also be analyzed using photonic crystal theory.[32]

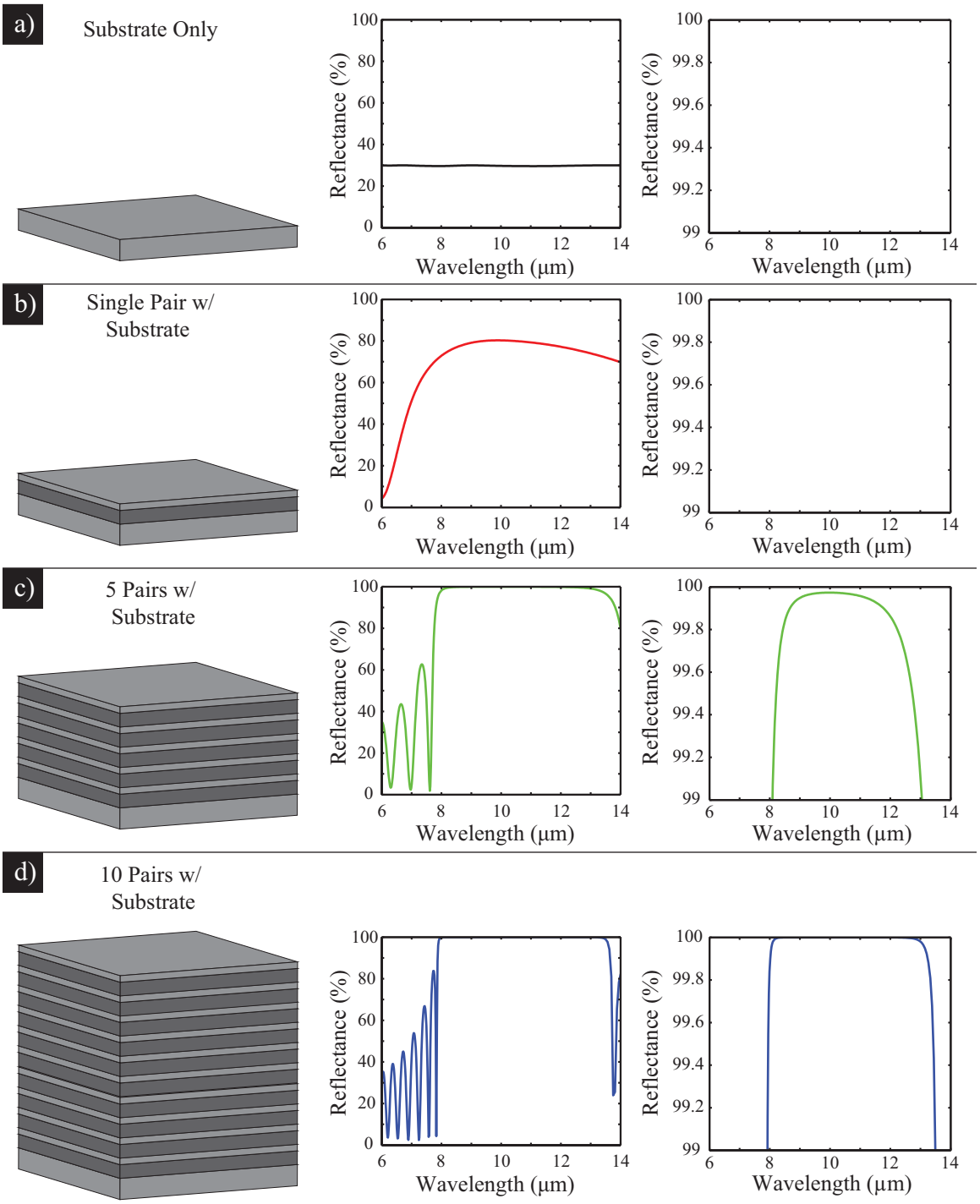


Figure 1.6: DBR schematics and associated responses for stacks of a) 0, b) 1, c) 5, and d) 10 bilayers of $Si/SiO_2$: $n_{Si}/n_{SiO2} = 3.42/1.5$.

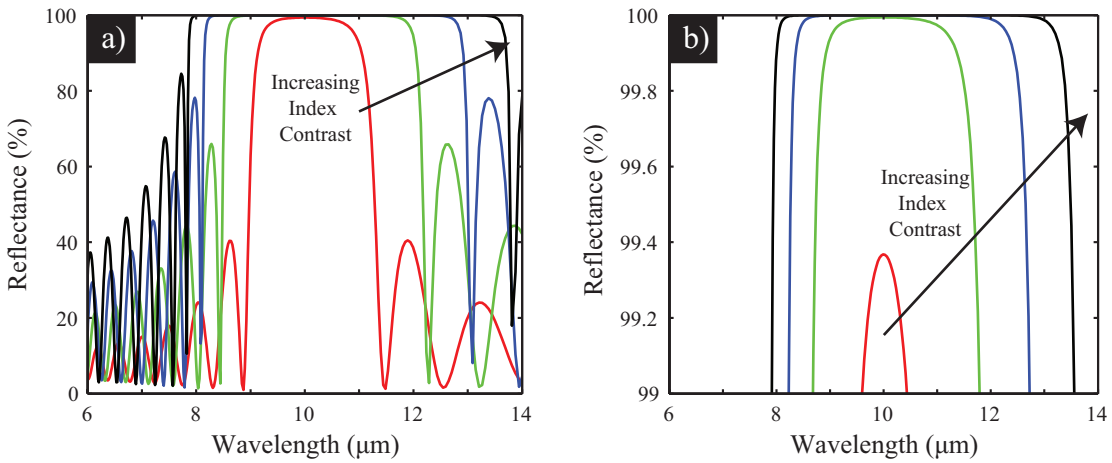


Figure 1.7: Index contrast dependence on DBR response for $n_{\text{low}} = 1.5$ and $1.5 < n_{\text{high}} < 3.5$ shown for a) reflectance from 0 to 100% and b) reflectance greater than 99%.

A DBR's reflectance and bandwidth is a function of the number of bilayers present in the system as well as the index contrast between the layers. Figure 1.6 shows the response of an $n_{\text{Si}}/n_{\text{SiO2}} = 3.42/1.5$ DBR with 0, 1, 5, and 10 bilayers. To achieve reflectance greater than that of metals, 99% , many bilayers are required, which limits their use in some applications. Figure 1.7 shows the response as the high-index material is varied between $2.0 < n_{\text{high}} < 3.5$ while keeping $n_{\text{low}} = 1.5$. A lower index-contrast system requires more bilayers to achieve comparable reflectance magnitude as a high index-contrast system. Furthermore, the attainable bandwidth is reduced for low index-contrast systems.

Although DBRs are widely used in laser and other cavity applications,[23,24,30] fabricating the structures can be challenging. Precise dielectric material deposition and access to compatible materials with different refractive indices are both strict requirements for DBR realization. Controlling the deposition such that each layer in the multi-layer stack has an accurate thickness is difficult, as uniformity, curvature, and surface roughness become larger concerns as the film thickness increases. Additionally, the index-contrast between available materials is often limited in crystal growth systems such as molecular beam epitaxy, where a finite number of materials

are available. For these reasons, developing spectrum-scalable lossless reflectors without the requirement of having many layers of deposited material could greatly ease fabrication and material requirements.

### 1.2.3 High Contrast Gratings

In 2004 Mateus *et al.* proposed a dielectric grating that promises ultra-broadband reflectance using a two layer structure,[18] shown schematically in Figure 1.8, in contrast to the multi-layer requirements of DBRs. The grating is simply composed of a single layer high refractive index grating surrounded by lower index materials. In the seminal theoretical study, the authors showed that optimizing the grating's dimensions, including its period ($\Lambda$), fill factor ($FF$, defined as the ratio of the high-index ridge width ($w$) to the period), layer thicknesses ($t$ and $h$) and material indices of refraction ($n_{\text{high}}$ and $n_{\text{low}}$), broadband reflectance similar to that of a DBR could be achieved. They studied a silicon ($n_{\text{high}} = 3.48$) grating on a $SiO_2$ ($n_{\text{low}} = 1.47$) layer that was surrounded by air ($n_{\text{air}} = 1$).The grating's reflectance was predicted to be greater than 99% with a bandwidth $\Delta\lambda/\lambda > 30\%$. Furthermore, they showed by scaling the grating dimensions, the operating wavelength range can be manipulated. Experimental demonstration soon followed with greater than 98.5% reflectance over a bandwidth of $\Delta\lambda/\lambda > 35\%$ achieved.[33]

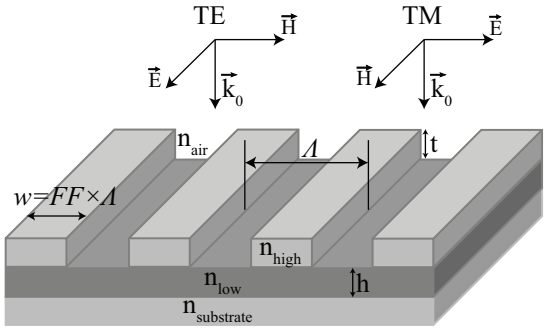


Figure 1.8: High contrast grating schematic with dimensions, material properties and exciting field defined.

The broadband reflectance in a single- or two-layer system is an attractive alternative to conventional DBR systems. For the grating system, the strict requirement of having compatible materials is loosened since etching a single layer provides the maximum index contrast for that material ($n_m/n_{\text{air}}$). The ability to obtain a large index contrast can provide broader reflectance bands than are often achieved with DBR material systems, enabling a larger tuning range for Fabry-Pérot etalon filters. Although their fabrication requires defining the grating, the multiple layer deposition, which can limit DBR use in longer wavelength applications, is no longer necessary.

The many unique characteristics of high contrast gratings have spurred their use in vast array of planar optical components. Since the early work of Mateus *et al.*, many researchers have used high contrast gratings to demonstrate broadband reflectors,[18,19,30,34–38] lensing capabilities,[39,40] hollow-core waveguides,[41] high-$Q$ resonators,[42,43] as well as other spectral engineering responses.[44–46] Furthermore, they have been integrated as the top reflector in vertical cavity surface emitting lasers,[23,30,41,47–51] enabling tunable lasing capabilities through electrostatic actuation.[52]

#### 1.2.3.1 Physics of Broadband Reflectance using Dielectric Gratings

Karagodsky *et al.* proposed a theoretical explanation for the broadband reflectance response exhibited by optimized high contrast gratings, which provides an intuitive picture for their operation.[53] The grating theory treats the periodic structure as an array of slab waveguides with propagation normal to the grating surface. Figure 1.9 shows the three regions of the grating for which Maxwell's equations and corresponding boundary conditions were applied. Region I and Region III are infinite half spaces of uniform media with plane waves accessible as supported modes. Region II is treated as a periodic set of slab waveguides with field components for TM polarization ($\boldsymbol{E} = E_x\hat{\boldsymbol{x}}$),

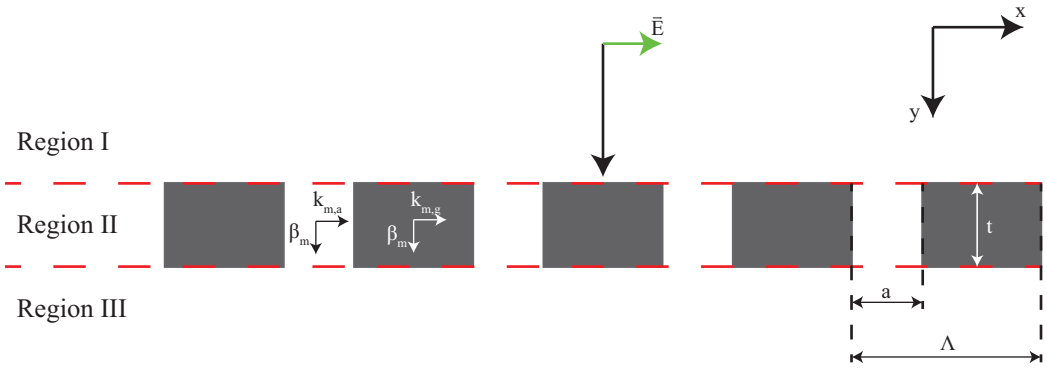


Figure 1.9: High contrast grating schematic used by Karagodsky *et al.* to solve for the modes responsible for the broadband reflectance response.[53]

$$H_z^{II}(x) = \sum_{m=1}^{\infty} h_{z,m}(x) \left[a_m \exp(-i\beta_m y) - a_m^{\rho} \exp(+i\beta_m y)\right] \ , \tag{1.6}$$

$$E_x^{II}(x) = \sum_{m=1}^{\infty} e_{x,m}(x) \left[a_m \exp(-i\beta_m y) + a_m^{\rho} \exp(+i\beta_m y)\right] \ , \tag{1.7}$$

where $a_m$ and $a_m^{\rho}$ are the coefficients of the forward propagating $(y)$ and backward propagating $(-y)$ waves, $\beta_m$ is the propagation constant in the $y$-direction, and $h_{z,m}$ and $e_{x,m}$ are the magnetic and electric field profiles in the lateral direction $(x)$:

$$h_{z,m}(0 < x < a) = \cos\left(k_{g,m}\frac{a}{2}\right) \cos\left[k_{a,m}(x - \frac{a}{2})\right] \ , \tag{1.8}$$

$$e_{x,m}(0 < x < a) = \sqrt{\frac{\mu_0}{\epsilon_0}} \frac{\beta_m}{k_0} h_{z,m} \ , \tag{1.9}$$

$$h_{z,m}(a < x < \Lambda) = \cos\left(k_{a,m}\frac{a}{2}\right) \cos\left\{k_{g,m}\left[x - \frac{(a+\Lambda)}{2}\right]\right\} \ , \tag{1.10}$$

$$e_{x,m}(a < x < \Lambda) = \frac{1}{n_g^2}\sqrt{\frac{\mu_0}{\epsilon_0}} \frac{\beta_m}{k_0} h_{z,m} \ . \tag{1.11}$$

In these equations, $\Lambda$ is the period of the grating, and $k_{g,m}$ and $k_{a,m}$ are the propagation constants in the $x$-direction for the high-index and low-index sections of the grating, respectively. The domain $(0 < x < a)$ represents the portion of the waveg-

uide with a low refractive index, while the domain $a < x < \Lambda$ represents the portion of the grating with a high refractive index. Periodic boundary conditions are used such that $h_{z,m}(x) = h_{z,m}(x+\Lambda)$ and $e_{x,m}(x) = e_{x,m}(x+\Lambda)$. The propagation constant $\beta_m$ for supported modes is

$$\beta_m^2 = k_0^2 - k_{a,m}^2 = n_g^2 k_0^2 - k_{g,m}^2 \ , \tag{1.12}$$

where $k_0 = 2\pi/\lambda$, the free space propagation constant for the incident light.

For an optimized reflector, the response is a consequence of interference between the lowest supported waveguide modes. Specifically, when the average field across a grating element of the first and second order modes cancel each other at the output plane, broadband reflectance results. This is summarized in the following equation,

$$|\boldsymbol{R_{00}}| = 100\% \rightarrow \frac{a_1 + a_1^\rho}{\Lambda} \int_0^\Lambda h_{y,1}^i n(x)\, dx + \frac{a_2 + a_2^\rho}{\Lambda} \int_0^\Lambda h_{y,2}^i n(x)\, dx = 0 \ . \tag{1.13}$$

The ability to realize this requirement is a consequence of the subwavelength nature of the grating where only the zeroeth order diffraction order needs to be considered. If the grating were not subwavelength, higher diffraction orders would result and the simultaneous cancellation of all terms would be more difficult.

### 1.2.4 Photonic Crystal Slabs and Guided Mode Resonance

Because the period of the gratings presented above is on the order of the wavelength of incident light, their operation can be discussed using photonic crystal theory.[32,54–56] In 1902, Wood observed anomalous rapid changes in reflectance from a diffraction grating that could not be explained with the conventional optical theory of the time.[57] Many explanations were subsequently offered to explain the anomalous behavior, including those of Rayleigh,[58] Hessel,[59] and Peng.[60] These explanations

provided a basis for how incident light can couple into modes supported by a dielectric grating. Later study of these systems in the context of photonic crystal theory has led to better understanding of the physics underlying the electromagnetic response of dielectric grating systems.[32,54,61,62]

In guided mode and photonic crystal theory, the grating's supported modes propagate in the plane of the grating, in contrast to the theory presented by Karagodsky *et al.* We will first discuss the supported modes of a slab waveguide to illustrate the physics of coupling between a grating's supported modes and incident plane waves. A slab waveguide is shown in Figure 1.10a; it includes a high-index guiding region ($n_1$) with thickness $d$ surrounded by a low-index region ($n_2$). Because the indices of refraction above and below the slabs are equal, this is referred to as a symmetric slab waveguide. The guided modes within the slab are eigensolutions of Helmholtz' equation. For transverse magnetic (TM) polarized light, where the magnetic field is maintained in a plane parallel to the $z$-direction, Helmholtz' equation takes the form,

$$\nabla \times \nabla \times \frac{1}{n^2}\boldsymbol{H} - \omega^2 \mu \boldsymbol{H} = 0 \ , \tag{1.14}$$

where $\boldsymbol{H} = H_z \hat{z}$ is the magnetic field, $n$ is the index of refraction, and $\mu$ is the permeability, with the constraint that $|H_z|$ decays exponentially with distance from the grating ($e^{i\omega t}$ time dependence is assumed throughout). The resulting transcendental equations, assuming nonmagnetic materials ($\mu_r = 1$), for the allowable propagation constants $k_x$ at a given frequency $\omega$ are

$$\tan(k_x d) = \frac{n_1^2}{n_2^2}\sqrt{\frac{\omega^2 \mu_0 (n_1^2 - n_2^2) d^2}{(k_x d)^2} - 1} \ , \tag{1.15}$$

$$-\cot(k_x d) = \frac{n_1^2}{n_2^2}\sqrt{\frac{\omega^2 \mu_0 (n_1^2 - n_2^2) d^2}{(k_x d)^2} - 1} \ , \tag{1.16}$$

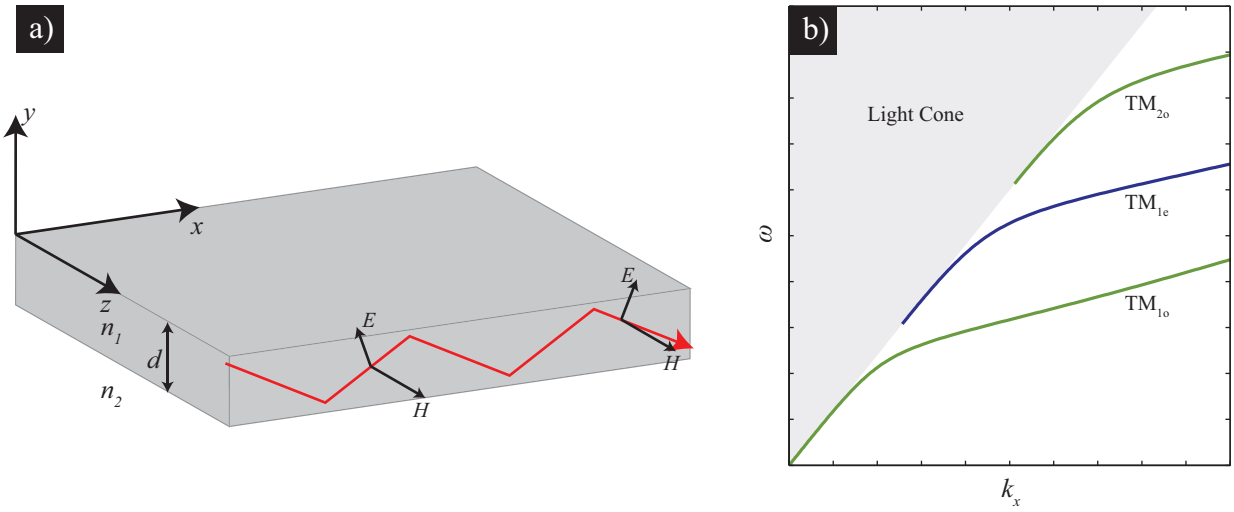


Figure 1.10: a) Slab waveguide schematic operating under TM polarization conditions and b) the dispersion curves of a symmetric slab waveguide where $TM_{1e}$ and $TM_{1o}$ are the first even and odd solutions to the governing transcendental equations and $TM_{2o}$ is the second odd solution to the transcendental equations, where even is defined with respect to the mirror reflection across the $xz$-plane.

where $\mu_0$ is the magnetic permeability of free space. The top equation provides the solutions for modes anti-symmetric upon reflection across the $xz$-plane, while the bottom equation provides the solutions to modes symmetric across this plane. The dispersion relations summarize the solutions to these equations, which are shown in Figure 1.10b. The bands $TM_{1o}$, $TM_{1e}$, and $TM_{2o}$ are the first odd and even supported modes and the second odd supported mode of the grating. In this context, even and odd are defined with respect to the mirror reflection across the $xz$-plane. These eigensolutions dictate the allowable guided modes supported by the system. Because these bands all lie below the light cone (gray region), they cannot couple to outgoing plane waves and thus have an infinite lifetime.

Photonic crystal slabs introduce a periodicity to the slab waveguide, which enables engineering of its dispersion relations. For a slab periodic along $\hat{x}$, the modes can be further expressed using Bloch's theorem,

$$H_z(\boldsymbol{r}; k_z) = e^{-ik_x x} u_{mk}(\boldsymbol{r}) \ , \tag{1.17}$$

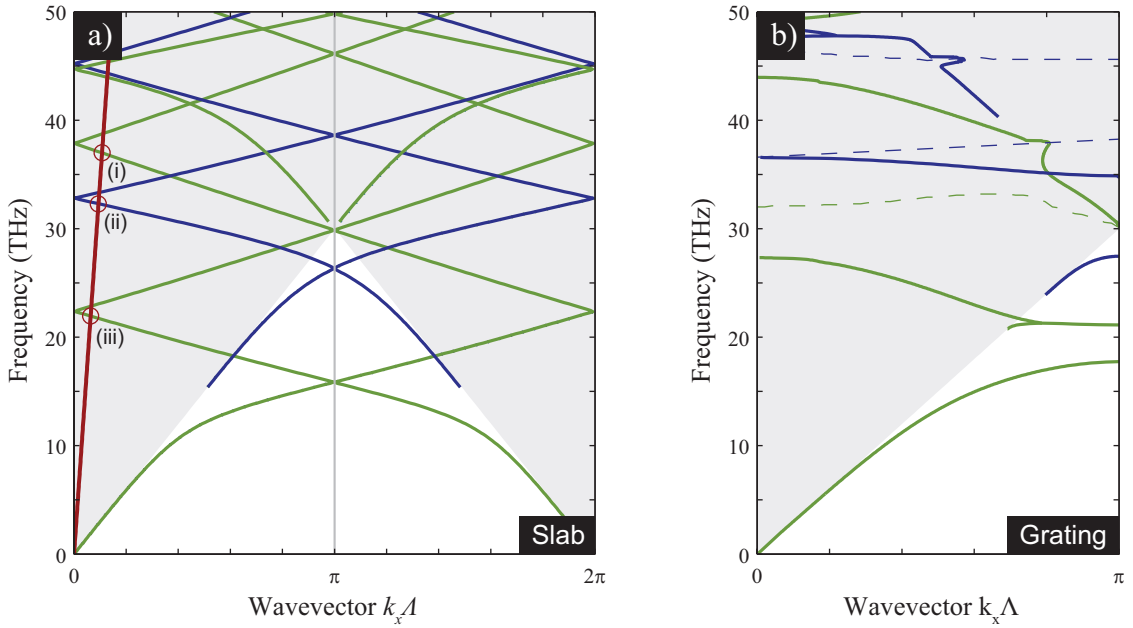


Figure 1.11: a) Slab waveguide dispersions represented in reduced-zone configuration. The intersections between the red light line and the dispersion curves ((i), (ii) and (iii)) indicate where coupling between the guided modes of the waveguide and incident light may occur. b) The dispersion relations for a silicon grating.

where $u_{mk}(\boldsymbol{r})$ has the same periodicity as the slab. With a small periodic modulation, the corresponding dispersion relations can be approximated as those of a uniform slab represented in a reduced zone scheme, shown in Figure 1.11a. This reduced zone scheme folds the slab waveguide dispersion bands about the $k_x\Lambda = \pi$ line, resulting in bands that lie within the light cone (gray region). Consequently, the modes within the light cone can couple to incident or outgoing plane waves, which is represented by the intersection of a guided mode band (blue (even) and green (odd)) with a light line (red). These modes have complex eigenvalues due to their decay into the continuum of radiative modes and are often called "leaky" modes. Increasing the modulation in the periodicity splits the bands at the zone edges ($|k_x| = \pi$) and zone center ($k_x = 0$), and shifts them to higher frequencies, as shown in Figure 1.11b.

Coupling between guided modes and plane waves results in signatures in the reflectance and transmittance spectra with bandwidths governed by the coupling strength to the continuum. The radiated power from an excited mode can be dis-

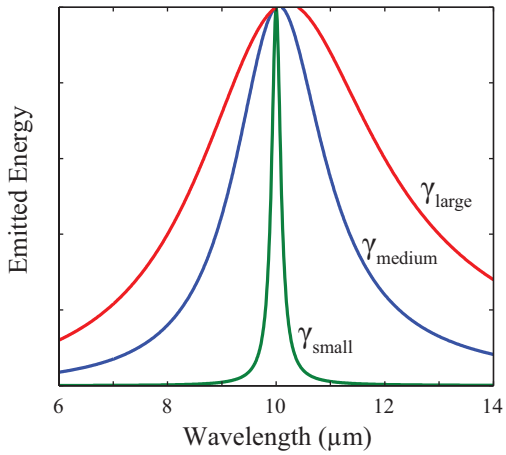


Figure 1.12: The effects of coupling strength on a resonance bandwidth.

cussed in the context of a damped oscillator,[26]

$$\frac{dI(\omega)}{d\omega} = I_0 \frac{\gamma}{2\pi} \frac{1}{(\omega - \omega_0 - \Delta\omega)^2 + (\gamma/2)^2} \ , \tag{1.18}$$

where $\omega$ is the frequency of light, $\omega_0$ is the frequency of the oscillator, $I_0$ is the intensity, $\Delta\omega$ is the frequency shift from due to the decay, and $\gamma$ is the decay constant. The energy decay of the oscillator follows $e^{-\gamma t}$ as a consequence of coupling to the continuum. Figure 1.12 illustrates the effects of the coupling strength to the resonance bandwidth. The coupling strength is dependent on the overlap between a guided mode and accessible propagating plane waves, where a larger overlap results in stronger coupling and hence, a broader response. From another perspective a larger $\gamma$ results in a shorter lifetime of the guided modes, as a consequence of being able to couple to a larger frequency band.

This analysis provides a second perspective for the operation of dielectric gratings, which will be used extensively in several of the studies in this thesis. Furthermore, it provides an alternative description of the broadband reflectance ascribed to high contrast gratings, where two strongly coupled guided modes have overlapping resonant profiles.[63]

### 1.2.5 Dielectric Grating-based Filtering Capabilities

Using dielectric gratings to achieve spectral filtering has potential to augment current LWIR hyperspectral imaging capabilities by reducing fabrication effort and improving filtering response. Furthermore, a grating operating in this spectral region has feature sizes amenable to photolithography. This is attractive for demonstrating proof-of-principle demonstrations, since the response is expected to be more tolerant of fabrication imperfections than studies in the near-infrared and visible spectral regions. Although dielectric grating-based filtering has been studied using both Fabry-Pérot type configurations,[21,30,64,65] and direct filtering using a grating alone,[20,66–69] few have operated in the LWIR.

In 1992 Magnusson proposed a reflection filter based on coupling to guided modes,[20] with experimental demonstration soon following.[70] Transmission filtering capabilities have seen less development, in part due to the difficulty obtaining an opaque background using a dielectric system. Multiple narrowband transmission filter designs have been proposed that are based on two interfering resonances, with one producing a broad high-reflectance background and the other producing a narrow transmission peak.[22,67,71–75] The sources of these resonances have included multiple adjacent gratings,[22,67,71] parallel gratings forming a cavity,[21,36] gratings coupled with quarter-wave reflector systems,[67,71–74] as well as multiple diffraction orders within a single grating.[75,76] While a few of the multilayer designs have been experimentally validated,[67,74] experimental demonstrations of narrowband transmission filters have generally been rare.[76,77]

### 1.2.6 Metallic Grating-based Filtering Capabilities

It is worthwhile to mention an alternative grating system that has yielded spectral manipulation demonstrations, namely those fabricated from metallic gratings. In 1998 Ebbeson *et al.* demonstrated extraordinary optical transmission through

subwavelength apertures, marked by greater than 100% transmittance, normalized to the open area.[78] Since this time, many studies have focused on realizing filtering capabilities across the electromagnetic spectrum.[79–81]

Similar to the mode coupling responsible for filtering capabilities in dielectric gratings, extraordinary optical transmission can occur when periodic arrays of small apertures in the metal allow light to couple to surface plasmon-polaritons on the metal surfaces. This modal coupling can result in much higher transmission than would be expected through uncoupled holes of the same size.[82] These transmission resonances operate similarly to those observed in dielectric gratings, with the high-reflectance background having a different origin for each system: a material plasma resonance in the perforated metal case, and a structural guided mode resonance in the case of dielectric gratings.

In addition to traveling surface plasmon modes, localized metal-insulator-metal modes can also yield resonant transmission and reflection filters through Fabry-Pérot type resonances.[83,84] Due to the localization of the modes, the response is fairly tolerant to changes in incident angle, making them additionally attractive for angle-insensitive filtering.

While metallic structures show potential to realize filtering capabilities, their linewidth and peak transmittance are often limited by absorption in the metal.[79,83,85] Lossless dielectrics, thus, have potential to provide narrower transmission bands and higher transmittance across the electromagnetic spectrum, provided lossless materials are available.

## 1.3 Thesis Organization

This thesis includes experimental and computational studies on dielectric grating-based broadband reflectors and narrowband transmission filters. It is organized into the following six chapters.

Chapter II contains the methods used in the studies. The fabrication of the gratings is discussed, which includes photolithography, dry etching and wet etching. This is followed by the techniques used to design and characterize the gratings, including finite element method simulations to model the system and Fourier transform infrared spectroscopy for experimental validation.

Chapter III includes experimental demonstrations of normal incidence broadband reflectors using $Si/SiO_2$ and Si/air gratings. While the $Si/SiO_2$ system is shown to exhibit broadband reflectance, its response is limited by absorption in the $SiO_2$ layer. Subsequent demonstration of a suspended silicon grating, which removes the lossy $SiO_2$ layer, exhibits greater than 90% reflectance across the entire LWIR spectrum.

Chapter IV summarizes the demonstration of a suspended silicon grating optimized to act as a broadband reflector at oblique incidence. Greater than 85% reflectance is achieved across the LWIR and the response is shown to be insensitive to polarization changes up to $10^\circ$ away from TM or TE polarization. Furthermore, over etching is determined to have little effect on the grating response.

Chapter V follows a group theoretical analysis of accessible mode coupling at normal and off-normal incidence. We show that at normal incidence several modes cannot couple to incident light because of mismatch in symmetry between the incident field and the grating's supported guided modes. Away from normal incidence, these selection rules are relaxed allowing weak coupling to the previously symmetry-protected modes. Two sets of modes (TE and TM) are independently coupled to a plane wave by changing the plane of incidence. We use this analysis to predict narrowband transmission filtering capabilities at off-normal incidence.

Chapter VI includes the experimental demonstration and characterization of narrowband transmission filters based on a suspended silicon grating operating at off-normal incidence. The grating exhibits transmission filtering capabilities that agree well with the simulated response and modal analysis. The filtered wavelength de-

pendence on the angle of incidence is studied and discussed to be a consequence of the slope of the dispersion relations. Wavelength selection is then demonstrated by changing the grating period.

Chapter VII summarizes the research and motivates future studies. In particular, narrowband transmission filters are discussed that break the symmetry of the grating instead of the incident light, as well as the integration of filters with detectors.

# CHAPTER II

# Methods

The methods used to simulate, fabricate, and characterize dielectric gratings will be discussed in the following sections and include: finite element analyses, photolithographic processing, and Fourier transform infrared (FTIR) spectroscopy. The depth of coverage is meant to promote duplication and understanding of the subsequent studies.

## 2.1 Computational Analysis

Finite element method (FEM) simulations were performed to predict the electromagnetic response of gratings to an incident plane wave. This method of computation casts the governing differential equation and boundary conditions into an integro-differential equation that can be solved numerically.[86]

We used the commercial FEM software package, COMSOL Multiphysics®, to simulate the electromagnetic response of proposed and as-built structures. The Helmholtz equation (Eq. 1.14) governs the response and is used by the software package to model the grating response. To define a simulated material, we generally used the complex index of refraction,

$$\tilde{n} = n - ik \ , \tag{2.1}$$

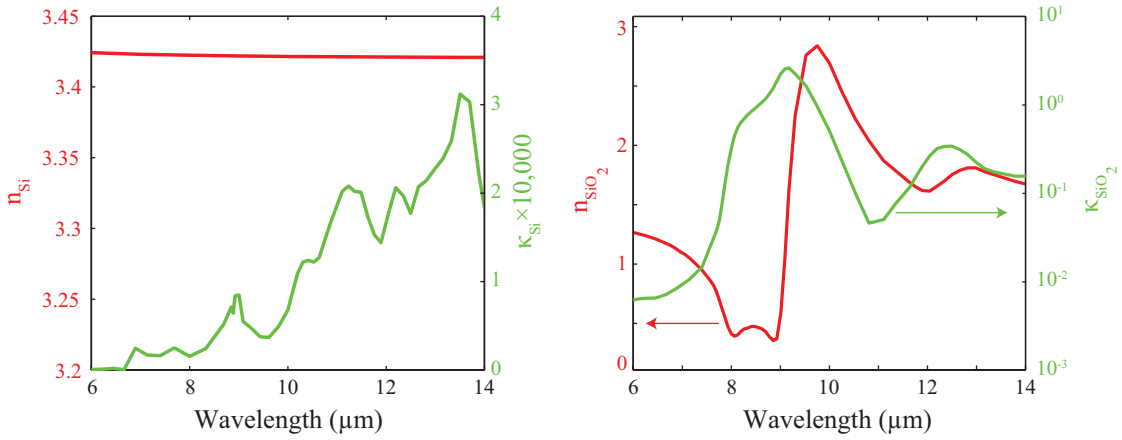


Figure 2.1: The index of refraction ($n$) and extinction coefficient ($\kappa$) for silicon and $SiO_2$ from literature.[87]

where $\tilde{n}$ is the complex index of refraction with $n$ and $\kappa$ being the refractive index and extinction coefficient, respectively. In general, the material optical properties were assumed to be equivalent to those from literature;[87] silicon and $SiO_2$'s indices of refraction and extinction coefficients are shown in Figure 2.1. We further assumed nonconducting ($\sigma = 0$) and nonmagnetic ($\mu_r = 1$) materials.

To simulate the grating response, a single period computational domain was used with periodic boundary conditions, as shown in Figure 2.2. The grating periodicity is in the $x$-direction while it is invariant in the $z$-direction. This invariance in $\hat{z}$ enables two-dimensional (2D) simulations, greatly reducing the computational demands compared to three-dimensional simulations. Both continuity and Bloch periodicity were used to define the boundary conditions. The Bloch periodicity is

$$\mathbf{E}(-\Lambda/2) = \mathbf{E}(\Lambda/2)e^{ik_x x} \ , \tag{2.2}$$

where $\mathbf{E}$ is the electric field at each boundary, and $k_x = k \sin\theta_m$ is the wave vector; $\theta_m$ is the angle from normal within each material, $m$.

The excitation as well as the reflection and transmission coefficients were managed using port boundary conditions with plane wave excitation. The incident port (Port

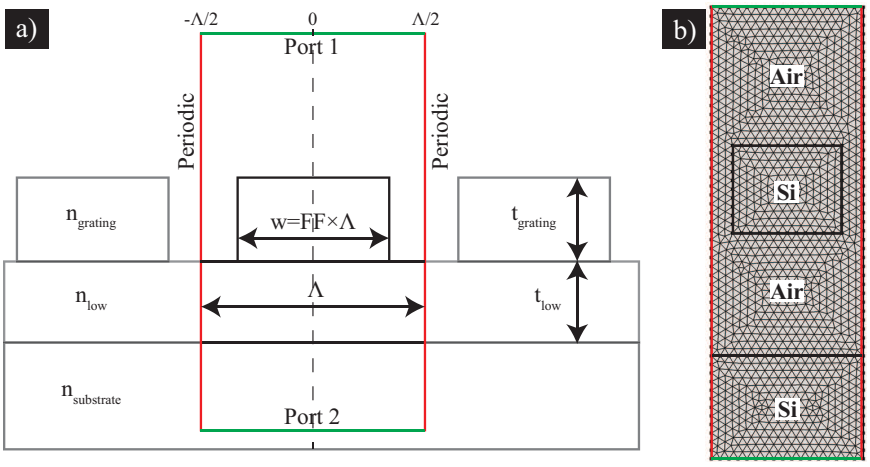


Figure 2.2: Grating schematic with computational domain indicated. The grating is defined by its period Λ, layer thicknesses ($t_{grating}$ and $t_{low}$), layer indices of refraction ($n_{grating}$, $n_{low}$, and $n_{substrate}$), and FF (defined as the ratio of the width of the grating ($w$) to the period (Λ)). The computational domain includes periodic boundary conditions (red) and port boundary conditions (green) for excitation and extraction of the reflectance $|S_{11}|^2$ and transmittance ($|S_{21}|^2$).

1) was located above the structure in air and the transmittance port (Port 2) was located within the substrate to alleviate the computational demands of simulating its entire 500 $\mu$m thickness. The reflection from the bottom interface of the substrate was accounted for by reducing the transmittance by 30% in subsequent analysis. The reflection and transmittance coefficients are given by the scattering matrix elements $S_{11}^2$ and $S_{21}^2$, respectively,

$$S_{11} = \sqrt{\frac{\text{power reflected by port 1}}{\text{power incident on port 1}}} = \frac{\int_{\text{port 1}} (\mathbf{E_c} - \mathbf{E_1}) \cdot \mathbf{E_1^*}\, dA_1}{\int_{\text{port 1}} \mathbf{E_1} \cdot \mathbf{E_1^*}\, dA_1}\,, \tag{2.3}$$

$$S_{21} = \sqrt{\frac{\text{power transmitted to port 2}}{\text{power incident on port 1}}} = \frac{\int_{\text{port 2}} \mathbf{E_c} \cdot \mathbf{E_2^*}\, dA_2}{\int_{\text{port 2}} \mathbf{E_2} \cdot \mathbf{E_2^*}\, dA_2}\,, \tag{2.4}$$

where the power is defined by the time-averaged Poynting vector,

$$\mathbf{S} = \frac{1}{2}\text{Re}(\mathbf{E} \times \mathbf{H}^*)\,. \tag{2.5}$$

The wave vector incident upon each port must match the stipulated port wave vector

to prevent unphysical reflections from occurring at these boundaries. Accordingly, the port wave vectors were

$$k_{\text{port1}} = \frac{2\pi}{\lambda_0} \cos(\theta_{\text{air}}) \ , \tag{2.6}$$

$$k_{\text{port2}} = \frac{2\pi}{\lambda_{\text{Si}}} \cos(\theta_{\text{Si}}) \ , \tag{2.7}$$

where $\lambda_{\text{Si}} = \lambda_0 / n_{\text{Si}}$ and Snell's law dictates the relationship between $\theta_{\text{air}}$ and $\theta_{\text{Si}}$,

$$n_{\text{air}} \sin\theta_{\text{air}} = n_{\text{Si}} \sin\theta_{\text{Si}} \ . \tag{2.8}$$

Because the studied gratings are subwavelength, only the zeroeth diffraction order contributes significantly to the electromagnetic response. Higher diffraction orders evanescently decay. On resonance, the zeroeth order transmittance and reflectance accounts for greater than 97% of the response. Accordingly, only the zeroeth diffraction order was included in many of the analyses.

The mesh density was chosen to enable efficient computation and adequate accuracy. The mesh was refined until the field profiles did not show the mesh geometry and the reflectance and transmittance coefficients did not show appreciable differences ($< 0.5\%$). An image of the resulting mesh density is shown in Figure 2.2b.

The data extracted from the simulations includes the reflectance and the transmittance coefficients as well as field profiles. Figure 2.3 shows representative data obtained from COMSOL simulations including a series of transmittance profiles displayed as a contour plot, several line plots associated with this data and a field profile ($H_z$) for the transmission band indicated by (i). These types of data were extensively used to understand the effects of changing various parameters of the grating, as well as for helping elucidate the physical basis for their operation. Specifically, the field profiles on resonance were used to extract the symmetries of the gratings' supported modes.

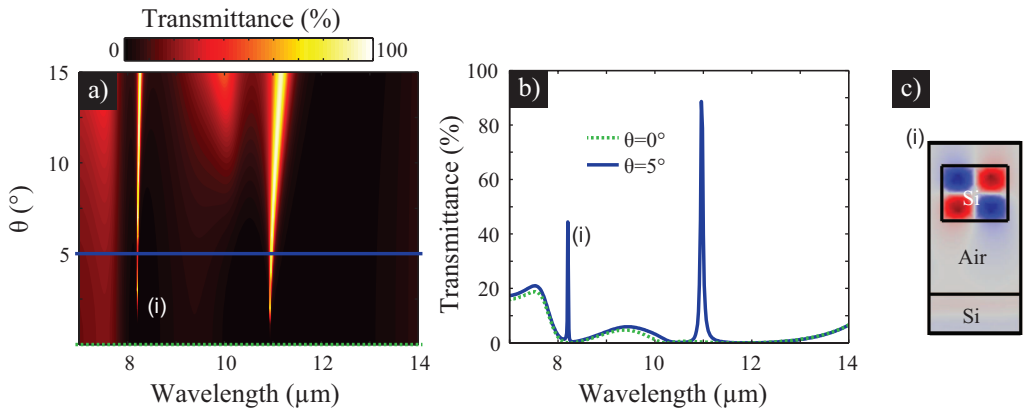


Figure 2.3: Representative COMSOL data showing a) a contour plot of extracted transmittance data, b) line plots of associated transmittance data, and c) $H_z$ field profile.

### 2.1.1 Structure Optimization

The grating response was optimized to achieve broadband reflectance across the LWIR by using an iterative process for finding the grating dimensions. Figure 2.4 illustrates the optimization flow for a germanium grating on top of a ZnSe substrate. Beginning with an unoptimized structure, the grating thickness was scanned to determine the thickness for which the most ideal broadband reflectance in the LWIR results. From the contour plot, $t = 2.6$ $\mu$m was selected, which was followed by a scan of the period. Again, the period corresponding to the best LWIR response was selected, $\Lambda = 3.9$ $\mu$m. This process is continued until the response does not change appreciably from further parametric scans, and the reflectance is centered about the LWIR region. The corresponding reflectance profile is also depicted for the optimized structure with $\Lambda = 3.9$ $\mu$m, $t = 2.3$ $\mu$m, and $FF = 69\%$. Broadband reflectance is achieved across the LWIR spectral region but is limited in its bandwidth due to the index contrast between the two materials Ge/ZnSe (4.1/2.4).

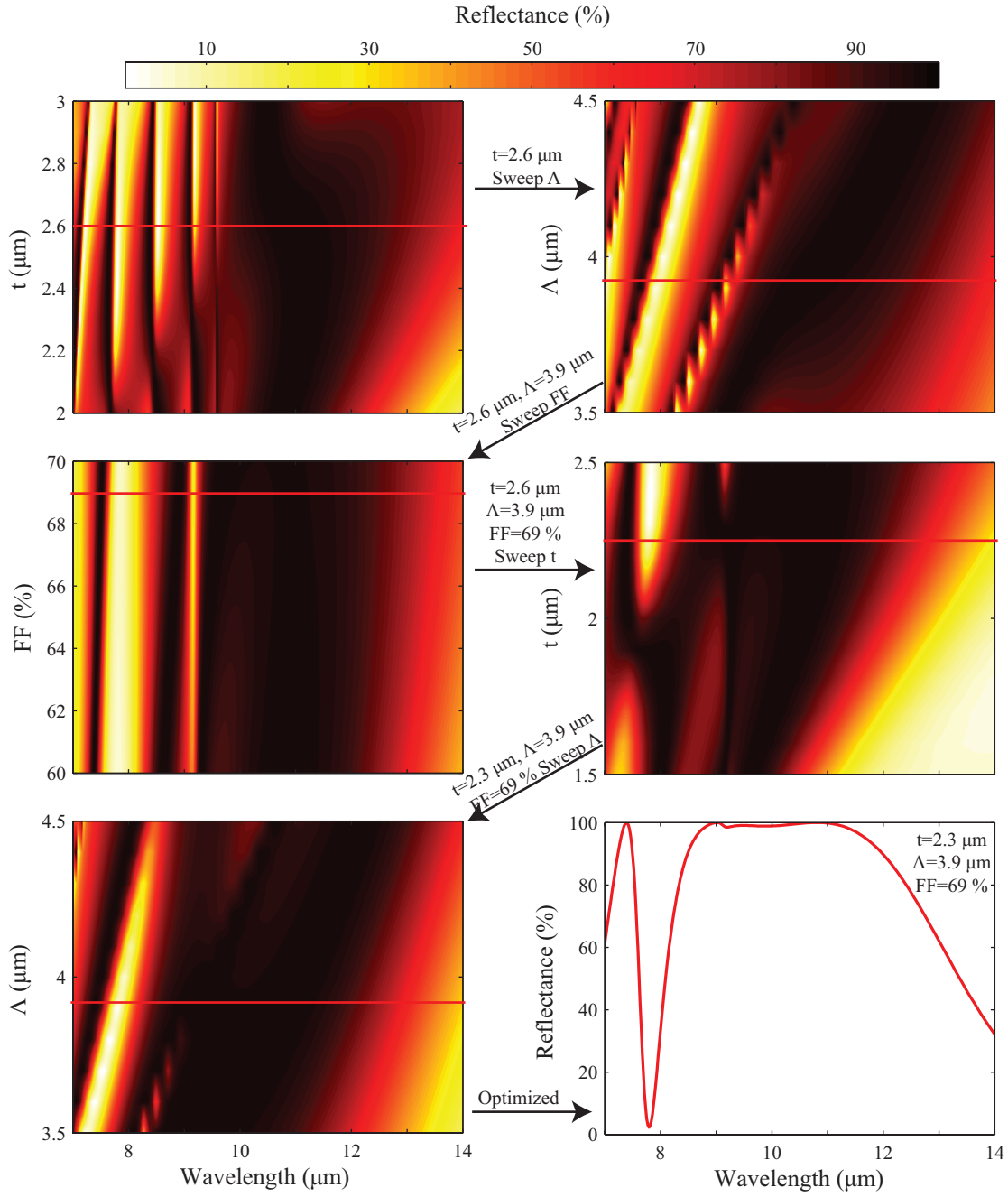


Figure 2.4: Illustration of the iterative optimization procedure used to design the gratings. The series corresponds to the optimization of a germanium grating on a ZnSe substrate.

### 2.1.2 Modal Analysis

We calculated the grating's dispersion relations using FEM to determine the guided modes supported by the grating geometry.[88–90] The computational method used to calculate these modes casts Eqs. (1.14 and 1.17) as a quadratic eigenvalue equation for a complex-valued propagation constant ($k_x$), given a choice of frequency ($\omega$).[90] The resulting weak form of the Helmholtz equation (Eq. 1.14) used for the computational analysis was

$$\int_{\Omega} d^2\boldsymbol{r} \left[ k_x^2 \frac{\mathrm{u}v}{\epsilon} + k_x \frac{i}{\epsilon} \left( \frac{\partial \mathrm{u}}{\partial x} v - \mathrm{u} \frac{\partial v}{\partial x} \right) + \frac{\partial \mathrm{u}}{\partial y} \frac{\partial v}{\partial y} \frac{1}{\epsilon} + \frac{\partial \mathrm{u}}{\partial x} \frac{\partial v}{\partial x} \frac{1}{\epsilon} - \left( \frac{\omega}{c} \right)^2 \mathrm{u}v\mu \right] = 0 \ . \quad (2.9)$$

In this equation, $v$ is a weighting function, u is the Bloch function, $c$ is the speed of light in free space, and $\epsilon$ and $\mu$ are the material relative permitivities and relative permeabilities, respectively. The integral is taken over the unit cell volume, $\Omega$. The two-dimensional computation region consisted of a single grating period with periodic conditions at $x = \pm\Lambda/2$ and perfectly matched layers[90] for the free-space boundaries.

An example of the resulting dispersion relations are shown in Figure 2.5 for a Si/air grating. The bands correspond to the allowable wave vectors supported by the grating and include even (blue) and odd (green) symmetries upon reflection across the $xz$-plane. The modal analysis can determine the eigensolutions of modes with long lifetimes, as their energy is concentrated near the grating region. Solid lines indicate modes that were calculated using the modal analysis, which couple weakly to the continuum. The imaginary components of the propagation constant for the dashed lines were larger than the Brillouin zone preventing them from being accurately determined using this method. Instead these bands were estimated from the reflectance profiles. These modes decay very quickly to the continuum and possess broad resonance features.

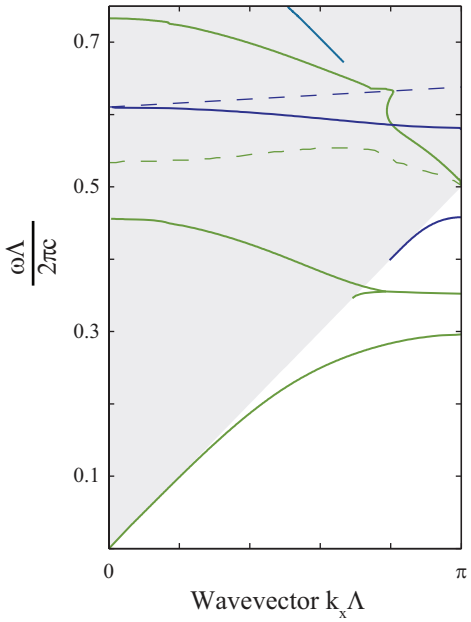


Figure 2.5: Representative TM modal analysis results for a Si/air grating.

## 2.2 Fabrication Procedures

The fabrication of dielectric gratings required photolithographic processing including cleaning the substrates, spinning photoresist, exposing the sample to ultraviolet light, and developing the photoresist. Subsequently, reactive ion etching was used to selectively etch the grating material, and in the case of the Si/air gratings, hydrofluoric (HF) acid etching was used to suspend the gratings.

### 2.2.1 Mask Design

A photolithography mask was designed to provide many combinations of grating periods and fill factors. The mask has elements for fabricating gratings with periods: 2 $\mu$m $< \Lambda <$ 5.5 $\mu$m in steps of 0.1 $\mu$m and fill factors: 50% $< FF <$ 85% in steps of 1%. Because some of the studies included suspending the grating structure, each matrix element, corresponding to a single period and fill factor, was split into two gratings with 250 $\mu$m $\times$ 500 $\mu$m dimensions. This built redundancy into the mask and ensured mechanical stability of the suspended gratings. The lateral extent of

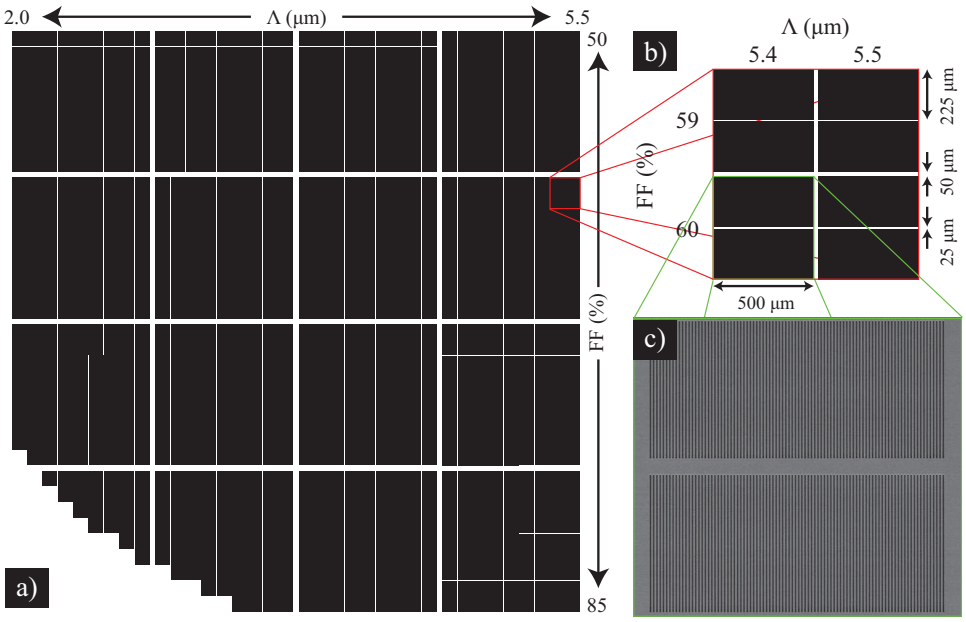


Figure 2.6: Photolithography mask design with grating dimensions. a) Mask layout. b) portion of mask showing dimensions of each grating. c) Fabricated matrix element.

the grating design possesses 250 and 90 periods for the 2 $\mu$m and 5.5 $\mu$m periods, respectively. Figure 2.6 shows the mask design, several matrix elements indicating the grating dimensions, and a corresponding scanning electron microscope (SEM) micrograph of a fabricated matrix element.

### 2.2.2 Photolithography

The gratings were defined on 1.5 cm $\times$ 1.5 cm silicon-on-insulator (SOI) substrates that were cleaned using five minute heated acetone and isopropyl alcohol baths followed by drying at 115° C for 10 minutes. SPR220 3.0 from Shipley Microposit®was spun for 30 s at 5000 rpm and followed by a soft bake at 115° C for 90 s. A GCA Autostepper projection mask aligner was used to expose the sample. The aligner uses an i-line ultraviolet source and a 5$\times$ reduction in the mask. Accordingly, the mask was designed 5$\times$ larger than the final dimensions. We used an exposure time of 0.31 s, a post exposure bake for 90 s at 115° C followed by developing for 60 s in Microposit MF-319. This completed the definition of the grating. Prior to dry-etching

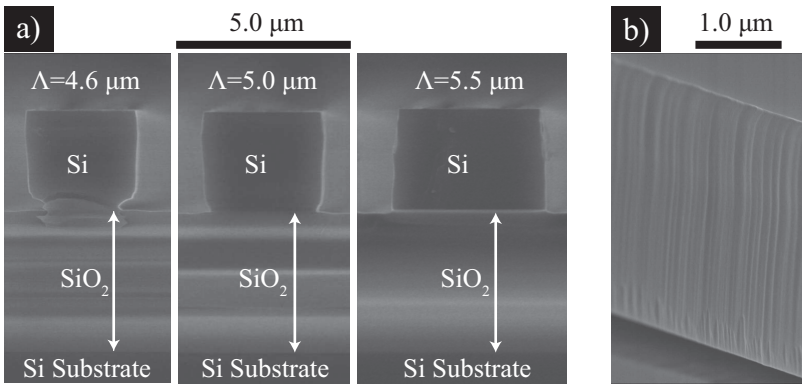


Figure 2.7: SEM micrographs showing He/HBr reactive ion etch profiles. a) Etch rate dependence on open area. Smaller open areas ($\Lambda = 4.6$ $\mu$m) exhibit over etching while larger periods ($\Lambda = 5.0$ $\mu$m and $\Lambda = 5.5$ $\mu$m) exhibit vertical etch profiles. b) Sidewall roughness.

the sample, a 100 W oxygen plasma etch for 90 s was used to descum the open area produced by the photolithography procedure.

### 2.2.3 Reactive Ion Etching and Hydrofluoric Acid Suspension

To selectively etch the silicon over the $SiO_2$, we used a He/HBr etch chemistry in a LAM 9400 reactive ion etching system. The optimized etch for a 3 $\mu$m silicon layer required 29 min of etching with flow rates of 200 sccm and 100 sccm for the He and HBr, respectively. The plasma was inductively coupled using a radio-frequency coupling power of 500 W and a bias power of 60 W. SEM analysis was used to help optimize the etch parameters for each run.

Figure 2.7 illustrates the open area dependence of the He/Hbr etch. For the

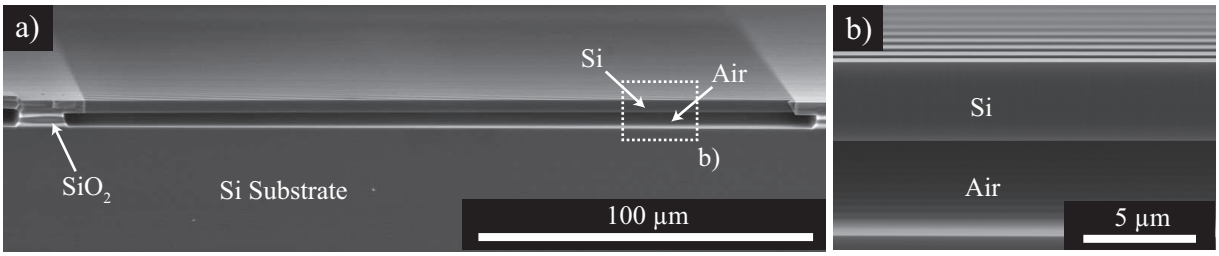


Figure 2.8: SEM images of suspended silicon structures.

smallest period ($\Lambda = 4.6\ \mu$m) the etch time resulted in over etching of the grating, characterized by undercutting at the bottom of the silicon region. This undercutting results from the difference between etch rates for the silicon and $SiO_2$ for the He/HBr chemistry. For larger periods ($\Lambda = 5.0\ \mu$m, $5.5\ \mu$m) the etch profiles become more ideal with nearly vertical sidewalls. Because of this effect, the etch rates for a particular structure had to be optimized to achieve vertical sidewalls for the given dimensions of a grating.

The surface roughness after reactive ion etching is also shown in Figure 2.7. The striations are due to inconsistencies in the photoresist profile and have a pitch of approximately 100 nm. Because these dimensions are much smaller than the operating wavelength (10 $\mu$m) the striations are not expected to influence the grating response off resonance. However, resonant features may be limited by scattering from these imperfections.

Following the He/HBr etch, a 5 minute oxygen plasma etch was used to remove the photoresist. This consisted of an 800 W bias, 80 sccm of $O_2$ and a substrate temperature of 150° C.

The majority of the studies also required suspending the grating by removing the underlying $SiO_2$ layer. This was accomplished with a 5 min, 49% HF acid etch. Figure 2.8 shows a suspended structure. Bowing of the suspended structures was determined to be negligible using image processing in Adobe Photoshop.

## 2.3 Fourier Transform Infrared Spectroscopic Characterization

Fourier transform infrared (FTIR) spectroscopy is an interference-based characterization technique that measures the response of a system to many frequencies simultaneously, in contrast to conventional dispersive spectrometers. For a thorough

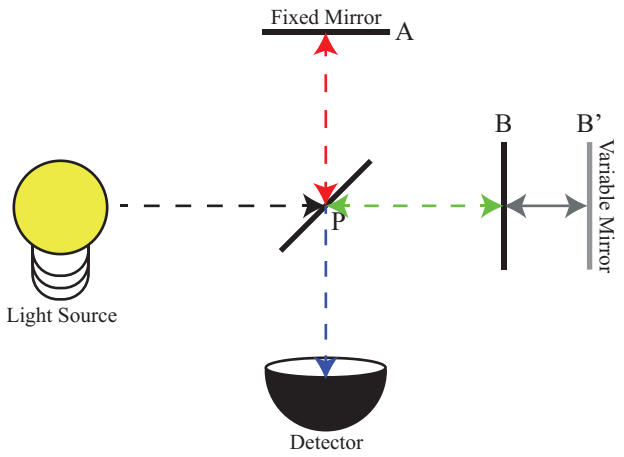


Figure 2.9: Michelson interferometer schematic.

description of FTIR techniques refer to Griffiths.[91] An FTIR spectrometer often utilizes a Michelson interferometer to generate the interference spectrum, or interferogram, required to extract absorption, reflectance, and transmittance information; a schematic of a Michelson interferometer is shown in Figure 2.9. The interferometer includes a light source, a detector, a beam splitter at point $P$ and two mirrors located at points $A$ and $B$. The beam splitter splits the light from the source into two separate paths traveling perpendicular to each other, $PA$ and $PB$. After reflecting off the two mirrors, the beams recombine at the beamsplitter where they interfere. One mirror is fixed at point $A$ while the second mirror's position is variable, shown as $B'$. The movable mirror is used to introduce a path length difference ($\delta = PB' - PA$) between the two interferometer arms. Whether constructive or destructive interference results when the beams recombine depends on $\delta$ and the frequency of light being used.

The requirements for constructive and destructive interference and their resulting output on a detector are illustrated in Figure 2.10a. For monochromatic light with wavelength $\lambda$, when $\delta = n\lambda/2$ ($n = 0, 1, 2..$), the total path length difference is an integral multiple of $\lambda$. Consequently, the two plane waves possess the same phase and, thus, constructively interfere. The detector reads a maximum in intensity for this wavelength. Conversely, when $\delta = \lambda/2(n + 1/2)$ the path length difference is

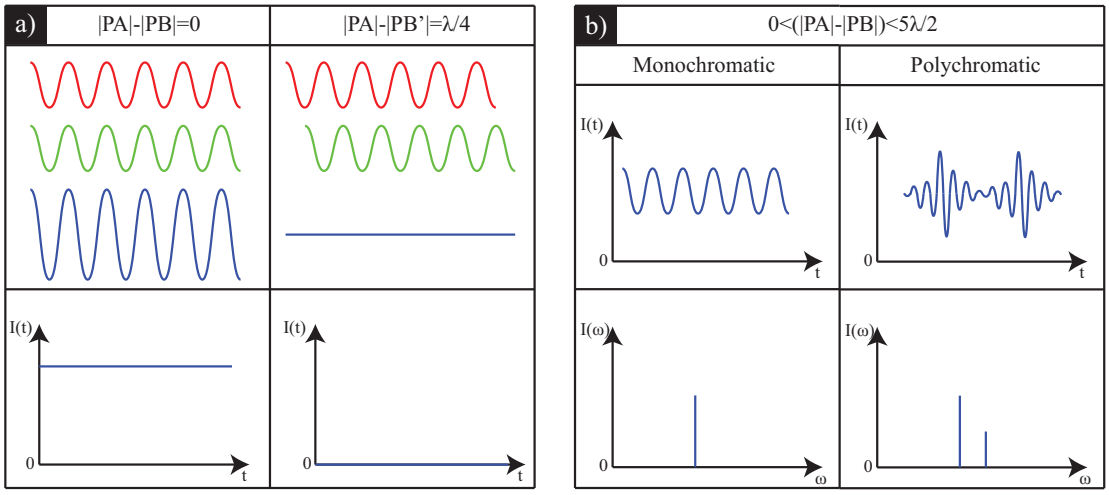


Figure 2.10: The conceptual operation of an FTIR. a) The requirements for constructive and destructive interference and the resulting intensity measured by the detector and b) the interferograms of monochromatic and polychromatic light and their resulting $I(\omega)$ spectra.

$(n + 1/2)\lambda$. In this case the waves are $\pi$ out of phase and destructively interfere, resulting in the detector reading a minimum in intensity.

If mirror $B$'s location is instead scanned at a constant velocity, the resulting interferogram is sinusoidal. This is a consequence of the mirror traveling through locations of constructive and destructive interference. The intensity as a function of time ($I(t)$) interferogram is shown on the top-left of Figure 2.10b. However, we are interested in the intensity measured for a given frequency, $\omega$, which necessitates the use of the Fourier transform,

$$I(\omega) = \int_{-\infty}^{\infty} I(t)e^{-i\omega t}\, dt \ , \tag{2.10}$$

where $\omega$ is the angular frequency, and $t$ is the time. During measurement, the mirror is moved a finite distance, resulting in truncation in the limits of integration that constrains the experimental spectral resolution. The Fourier transform of the

interferogram on the left side of Figure 2.10b yields a single peak $I(\omega)$ at $\omega = 2\pi c/\lambda$.

When performing measurements with a polychromatic light source, the interferogram is a superposition of many sinusoidal responses with different frequencies. A simple interferogram illustrating polychromatic light and the resulting spectrum after Fourier transformation is shown on the right side of Figure 2.10b.

A sample's reflectance and transmittance properties can be determined by placing it in the beam path and measuring its interferogram. To obtain quantitative data, the response is normalized to a reference. For transmittance measurements, standards can include air or an unpatterned substrate. A gold reflectance standard is often used for reflectance measurements.

### 2.3.1 Experimental Setup

Grating characterization was performed using a Perkin Elmer Spectrum GX FTIR spectrometer with an AutoImage microscope attachment; a schematic of an FTIR is illustrated in Figure 2.11. A potassium bromide (KBr) beamsplitter was used for the mid-infrared characterization, and an internal aperture was used to specify the sample area to be characterized. A wire-grid polarizer, with manual orientation specification ($\pm 5^\circ$), was placed in the detected light's path. The system uses a liquid nitrogen ($LN_2$) cooled mercury cadmium telluride (MCT) detector.

Four $cm^{-1}$ resolution was used for all measurements, with a mirror scan velocity of 2 cm/s. This corresponds to a resolution of 40 nm at an operating wavelength of 10 $\mu$m. Consequently, for resonant phenomena, the highest measurable quality factor ($Q = \omega/\Delta\omega$) is 125.

Cassegrain objectives are used to focus and collect light in transmittance and reflectance modes. These high numerical aperture lenses ($NA = 0.6$) provide incident light between 16° and 36°. Schematics of the incident and detected light configurations for reflectance and transmittance measurements are shown in Figure 2.12. In

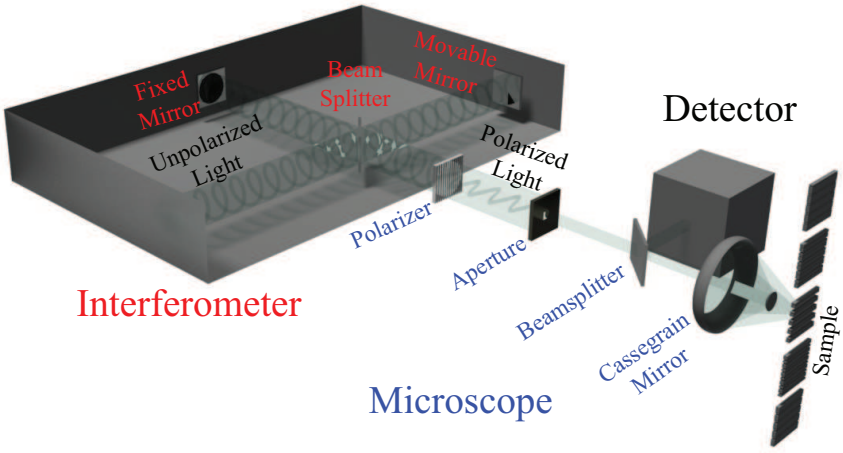


Figure 2.11: Pictorial representation of commercial FTIR spectrometer with microscope attachment operating in reflectance mode with different components of the general characterization method.

reflectance mode, one half of the Cassegrain objective is used for the incident light while the second half is used for detection. This results in $\pi$-radians of incident light between 16° and 36°. Conversely, in transmission mode the entire $2\pi$-radians are used for the incident and detected field. Two studies were conducted in reflectance mode while the others were conducted in transmittance mode using a custom-made sample holder and an aperture placed above the sample to more precisely define the excitation.

The custom sample holder has a 20° tilt relative to the horizontal stage that enables normal incidence characterization. Unfortunately the sample holder is not amenable to reflectance measurements because light cannot reflect to the portion of the Cassegrain objective responsible for detection. Instead, the reflectance was calculated from the sample's transmittance spectrum using $R = 100\% - T$. While this is not strictly true for all materials, silicon has an extinction coefficient less than $4 \times 10^{-4}$ across the LWIR spectrum providing a reasonable basis for this assumption.[87]

An optical iris suspended above the sample was used as an aperture to constrain the Cassegrain objective light. The size of the aperture and height above the sample was dictated by the signal strength. Consequently, to obtain a measurable signal

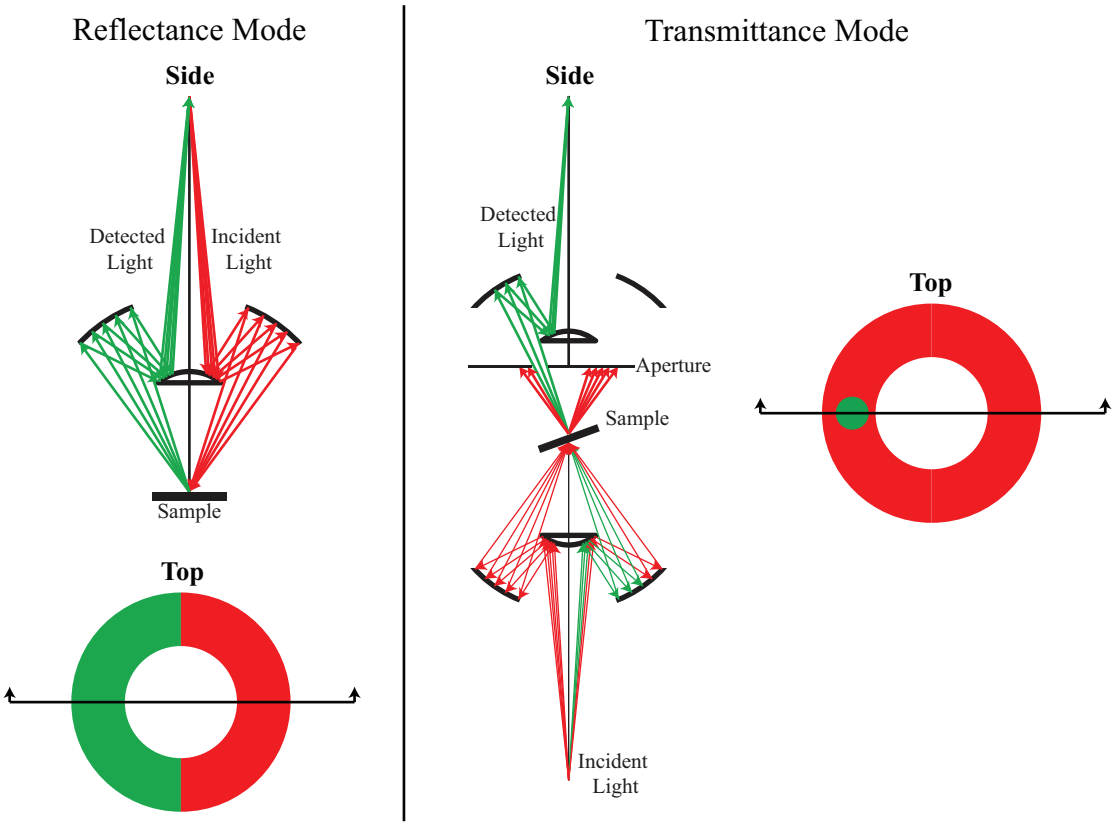


Figure 2.12: Incident light configurations for reflectance and transmittance measurements.

from the globar source, the aperture permitted a range of angles ($\theta \pm 3^{\circ}$). This angular extent results in an effective numerical aperture of $NA \approx 0.05$. The aperture's location was manipulated using an $xyz$-translation stage with micrometer adjustment, which enabled the plane of incident light to be arbitrarily chosen around the azimuth of light. This flexibility in choosing the excitation configuration is shown in the schematic of Figure 2.12.

# CHAPTER III

# Normal Incidence Broadband Reflectors

In this chapter we demonstrate broadband reflectors operating at normal incidence that have potential to be integrated into Fabry-Pérot etalon filters. The first demonstration utilizes a silicon grating on a $SiO_2$ layer. It exhibits broadband reflectance but is limited in the LWIR by absorption in the $SiO_2$ layer. To mitigate this loss, a suspended silicon grating is proposed and demonstrated that exhibits greater than 90% reflectance across the entire LWIR spectral region.

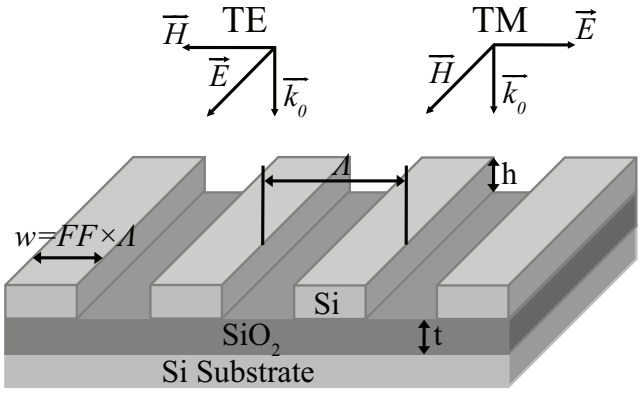


Figure 3.1: Schematic illustration of the dielectric grating geometry with definition of incident field polarization.

## 3.1 Si/$SiO_2$ Grating System

The first grating study focuses on achieving broadband reflectance at normal incidence using a Si/$SiO_2$ material system. This material choice has been previously used in near-infrared demonstrations, making it attractive for scaling to other spectral regions.[18] Figure 3.1 illustrates the design parameters used in the simulation: thickness of silicon ($t$), height of $SiO_2$ ($h$), grating period ($\Lambda$), and ratio of the grating width to $\Lambda$, referred to as the fill factor ($FF$). The benefits of using Si/$SiO_2$ for this structure include the large index contrast (3.42/1.45) and the quality and availability of materials.

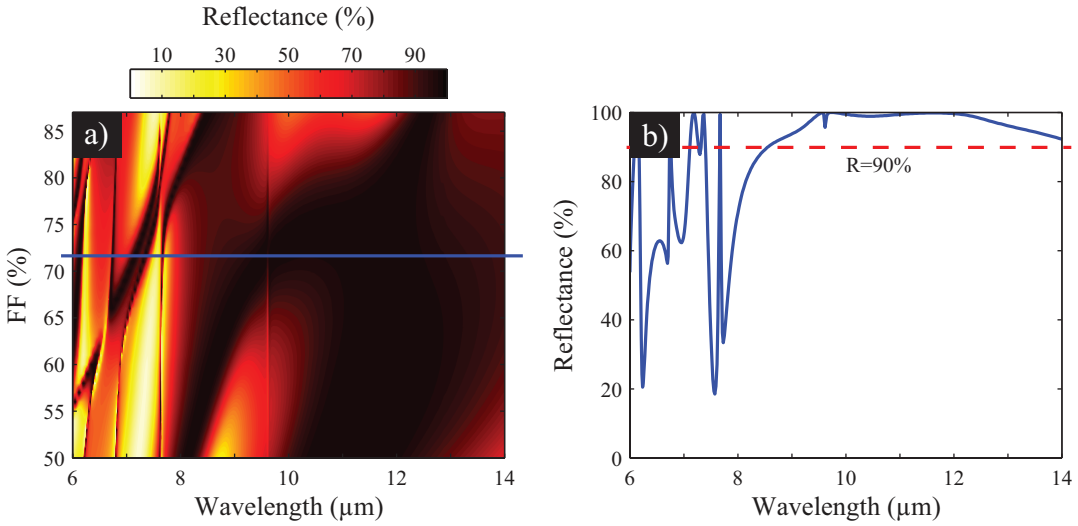


Figure 3.2: a) Simulated reflectance results of the Si/$SiO_2$ grating with $t$ = 3.4 $\mu$m, $h$ = 3.9 $\mu$m, $\Lambda$ = 5.1 $\mu$m varying the fill factor, and b) the corresponding reflectance spectrum for FF=72%.

We used commercial FEM software to optimize the structure for transverse magnetic (TM) excitation (electric field parallel to the grating periodicity) between 4 and 18 $\mu$m by varying the grating parameters ($t$, $h$, $\Lambda$, and $FF$). The indices of refraction for Si/$SiO_2$ were assumed to be constant across the LWIR for the initial design, consistent with previous Si/$SiO_2$ grating studies. The optimized dimensions to achieve high reflectance in the LWIR region were $\Lambda$ = 5.1 $\mu$m, $t$ = 3.4 $\mu$m, $h$ = 3.9 $\mu$m, and

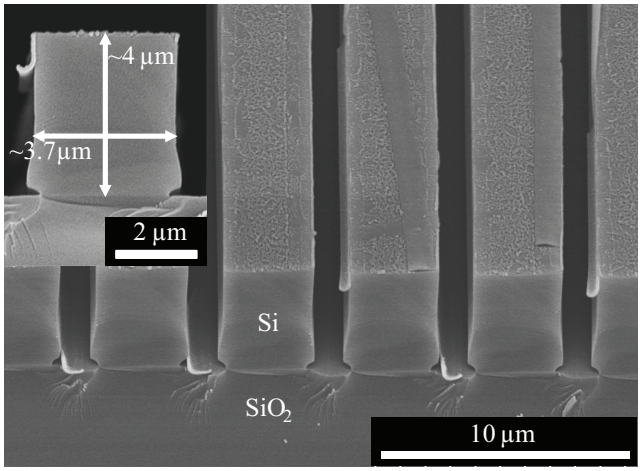


Figure 3.3: SEM micrograph of fabricated $Si/SiO_2$ grating.

$FF = 72\%$. Figure 3.2a illustrates the dependence of the grating reflectance on fill factor, where a small window of fill factors yields high reflectance. Outside this range the reflectance near $\lambda = 10$ $\mu$m begins to decrease. The field response corresponding to the optimized fill factor ($FF = 72\%$) is shown in Figure 3.2b, which exhibits greater than 90% reflectance for $8.5 < \lambda < 14.5$ $\mu$m.

Experimental demonstration was achieved using a commercial SOI substrate. Substrates with the optimized thicknesses could not be obtained, instead commercially available substrates were used (Ultrasil Corp, $< 100 >$, $\rho = 1 - 30$ $\Omega$-cm). The substrates had silicon and $SiO_2$ thicknesses of $4 \pm 0.5$ $\mu$m and $4 \pm 0.2$ $\mu$m, respectively. The grating was defined using projection photolithography techniques and reactive ion etching, resulting in gratings with: $\Lambda = 5.0$ $\mu$m and $FF = 72\%$. An SEM micrograph of a fabricated grating is shown in Figure 3.3.

We used a commercial FTIR spectrometer in conjunction with a microscope attachment to characterize the grating response. Measurements were taken over an area of 200 $\mu$m $\times$ 200 $\mu$m, corresponding to approximately 40 grating periods. The reflectance was normalized to that of a gold standard. The polarization of the reflected wave was controlled with a wire-grid polarizer placed in front of the photodetector.

Figure 3.4 shows the grating reflectance for TM polarization, TE polarization, and

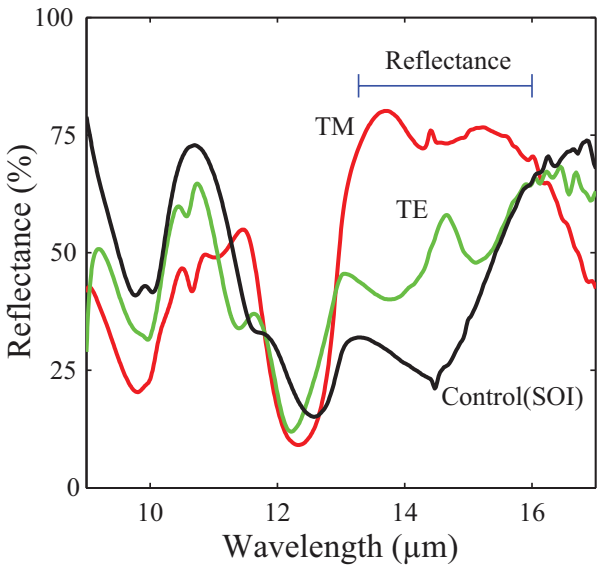


Figure 3.4: Polarization dependent FTIR reflectance of a $Si/SiO_2$ grating with dimensions: $t = 3.9$ $\mu$m, $h = 3.9$ $\mu$m, $\Lambda = 5$ $\mu$m and FF=72%.

the response of an unpatterned portion of the SOI wafer. The grating exhibits broadband reflectance in the spectral range 13-16 $\mu$m for TM polarization. For reflectance greater than 70%, the spectral width of the reflectance band was $\Delta\lambda/\lambda = 18.5\%$. The field-response is polarization dependent: TM polarization exhibits relatively high reflectance, whereas TE polarization (electric field polarized perpendicular to the grating periodicity) exhibits a much lower response over the same spectral range. The average extinction ratio for TE:TM polarizations in the broadband region is 1:1.6 with a maximum contrast of 1:2.0 at $\lambda = 13.7$ $\mu$m and a minimum contrast of 1:1.1 at $\lambda = 15.9$ $\mu$m.

The experimental results demonstrate the expected qualitative broadband reflectance but they deviate significantly from the initial simulations. These deviations are a consequence of the material optical properties, and experimental constraints. The initial design assumed constant indices of refraction for the $Si/SiO_2$ layers, however $SiO_2$ exhibits phonon absorption within the LWIR spectral region.[87,92] The index of refraction and extinction coefficient of $SiO_2$ from literature[87] are shown in Figure

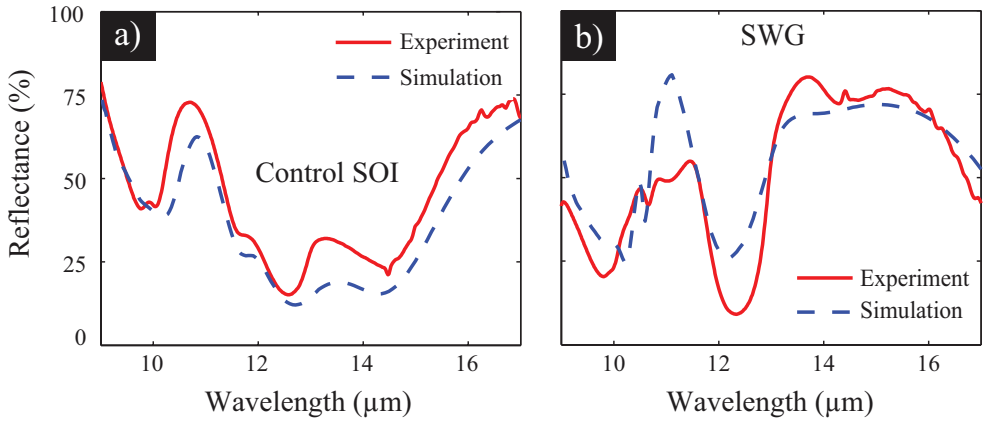


Figure 3.5: Measured and simulated reflectance for a) unpatterned SOI wafer and b) patterned $Si/SiO_2$ grating.

2.1; two absorption bands centered at 9 and 12.5 $\mu$m are evident in the extinction coefficient within the LWIR. These bands are attributed to Si-O-Si asymmetric and symmetric stretching phonons and are responsible, to a large extent, for the deviation of the experimental results from the design.[92]

To evaluate the influence of the wavelength dependent optical properties of silicon and $SiO_2$ on the grating field-response, the reflectance spectrum of an unpatterned region of the SOI wafer was compared to simulation results that incorporated the reported complex dielectric constant spectrum of silicon and $SiO_2$, as shown in Figure 3.5.[87] The spectra possess strong peak location correlation and similar peak intensities. The differences in intensity arise from uncertainty in the reported dielectric constants (particularly for $SiO_2$), intrinsic material differences from the cited literature (bulk vs. thin film, conductivity, etc.), and the uniformity of the layered structure.

In addition to the complex optical properties, the as-built structures were also subjected to fabrication and characterization constraints. The fabricated structure exhibits over etching and layer thicknesses that deviate from the optimized structure. Furthermore, the plane wave incidence of the simulation is limited in its ability to model the incident field from the Cassegrain objective. To account for some of these deviations, the wavelength dependent dielectric constants and fabricated structure

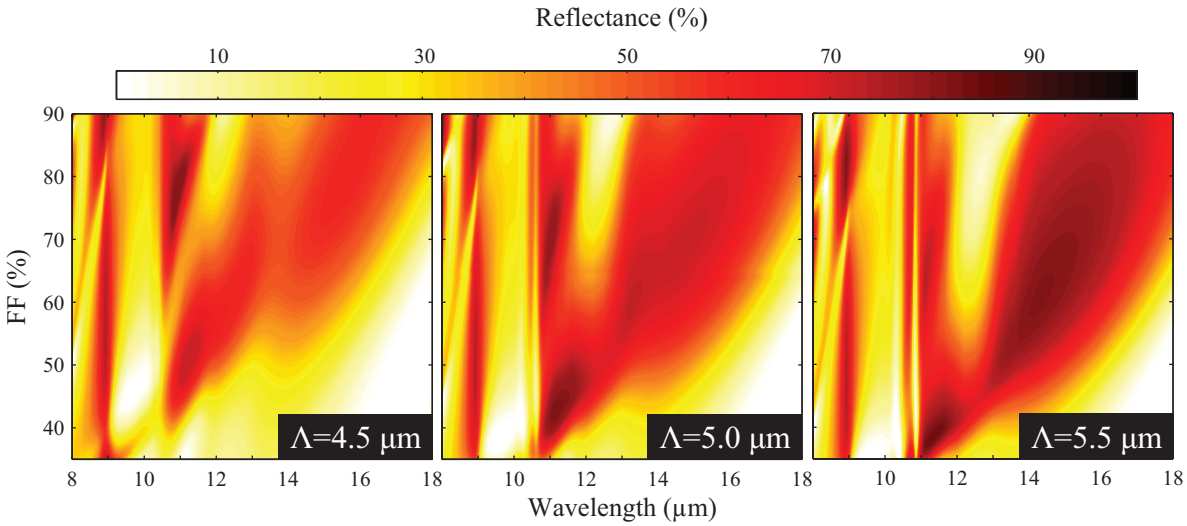


Figure 3.6: Re-optimization of the $Si/SiO_2$ grating integrating complex indices of refraction for the materials.

dimensions, extracted from SEM images, were incorporated into the grating simulation. The measured structure dimensions were: $t = 3.9$ $\mu$m, $h = 3.9$ $\mu$m, $\Lambda = 5.0$ $\mu$m and $FF = 72\%$. Figure 3.5b shows the experimental results and those from simulation after modifying the physical dimensions and optical properties to match the fabricated grating. The agreement between the simulated and experimental spectra is strong. As with the SOI control structure, small deviations are likely due to differences in material properties or imperfections in the grating geometry. There is loss in the experimental spectra compared to the simulation at $\lambda = 11$ $\mu$m that cannot be attributed to differences in the $Si/SiO_2$ properties. This deviation is likely a consequence of the Cassegrain objective, which permits many angles of incident light, instead of the plane wave incidence simulated.

Greater than 99% reflectance was expected for the designed structure while the fabricated grating exhibited less than 80% reflectance due to the strong absorption of $SiO_2$ in the measured spectral range. Subsequent re-optimization of the grating structure incorporating the wavelength dependent optical properties of the materials was ineffective at producing broadband reflectance across the LWIR. Figure 3.6 shows

contour plots varying the fill factor for different grating periods. The loss associated with the asymmetric Si-O-Si phonon band between 9 and 10 $\mu$m dominates the response of all the structures. Thus, to demonstrate broadband reflectance, suspending the grating to remove the lossy $SiO_2$ was pursued.

## 3.2 Suspended Silicon Grating System

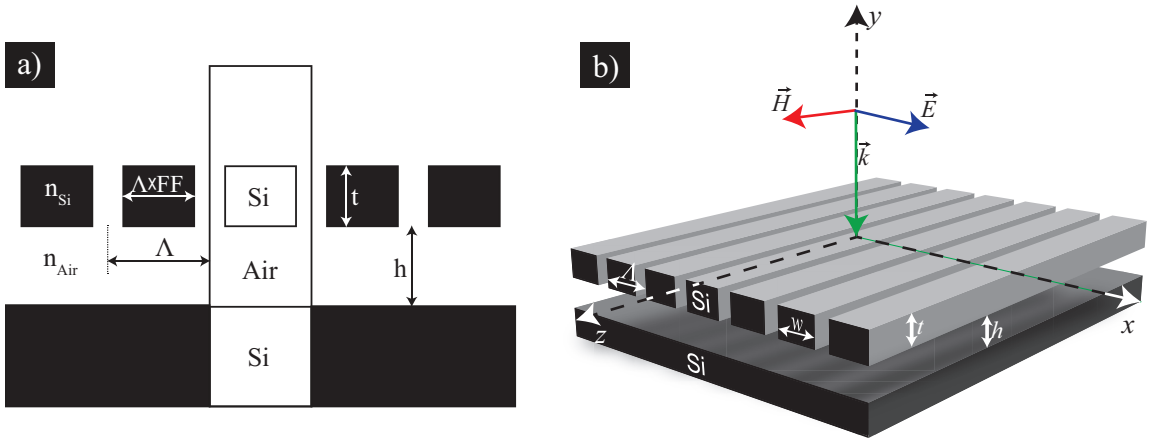


Figure 3.7: A suspended grating schematic including a) a cross section with dimensions and computational domain defined and b) a three-dimensional schematic with field and incident angle defined.

The foundational work of the $Si/SiO_2$ grating reflector was used as the basis for demonstrating broadband reflectance using a suspended silicon grating, where the suspended grating eliminates the loss associated with the underlying $SiO_2$ layer. A Si/air system provides a high-index contrast (3.42/1), crystalline optical properties and ease of fabrication based on commercially available SOI wafers. Additionally, silicon's superior mechanical properties during suspension are attractive for future microelectromechanical (MEMS) actuation studies that could enable tunable filtering capabilities. Figure 3.7a depicts a cross section of the suspended silicon grating structure with its dimensions and the computational domain illustrated. Figure 3.7b shows the grating in three-dimensions with the incident wave and polarization defined. The grating field response is dependent on the period ($\Lambda$), fill factor or duty cycle

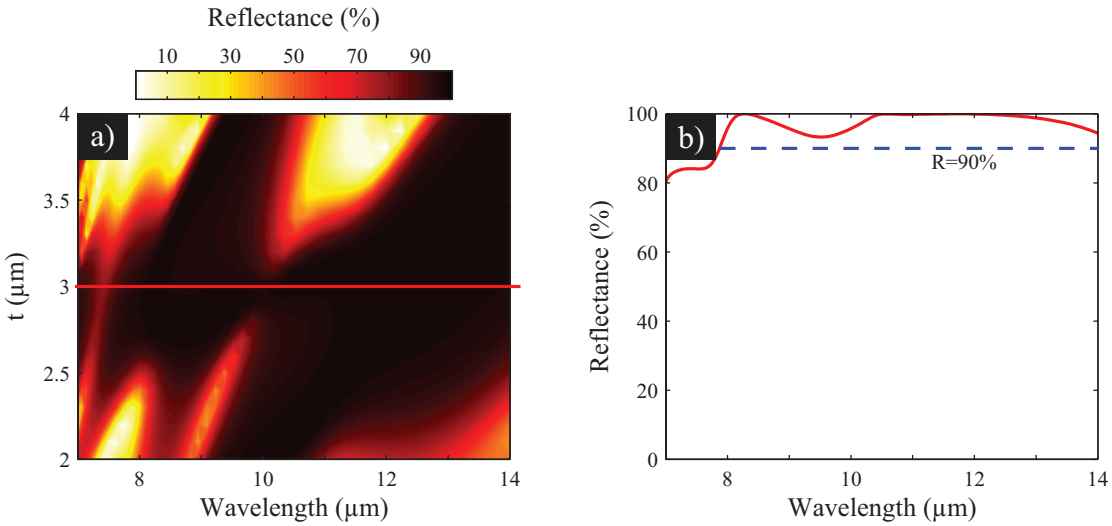


Figure 3.8: a) Reflectance profile dependence on the height of the grating and b) the corresponding optimized normal incidence response: $\Lambda = 5$ $\mu$m, $t = 3$ $\mu$m, $h = 4$ $\mu$m, and $FF = 72\%$.

($FF$), and Si thickness ($t$) with fixed air layer thickness ($h = 4$ $\mu$m).

Iterative dimension optimization was again performed to achieve broadband reflectance centered at 10 $\mu$m (TM polarization). Due to phonon absorption within the LWIR, explicit material dispersion relations were incorporated from literature.[87] Figure 3.8 shows a representative contour plot containing the optimized grating dimensions and the corresponding optimized response for a grating with $\Lambda = 5$ $\mu$m, $t = 3$ $\mu$m, $h = 4$ $\mu$m, and $FF = 72\%$. The response is similar to the designed $Si/SiO_2$ grating response with reflectance greater than 90% between 8 $\mu$m and 14 $\mu$m, making it attractive for LWIR applications.

The photolithography mask with gratings including 2 $\mu$m $< \Lambda <$ 5.5 $\mu$m and $55\% < FF < 85\%$ was used to provide an experimental means of testing the parameter dependent response. The grating fabrication began with the same processing steps used for the $Si/SiO_2$ broadband reflector grating followed by the five minute HF etch to suspend the gratings.

Plan view and cross sectional SEM analysis was used to facilitate silicon etch optimization and to extract as-built dimensions used for response analysis. Figures

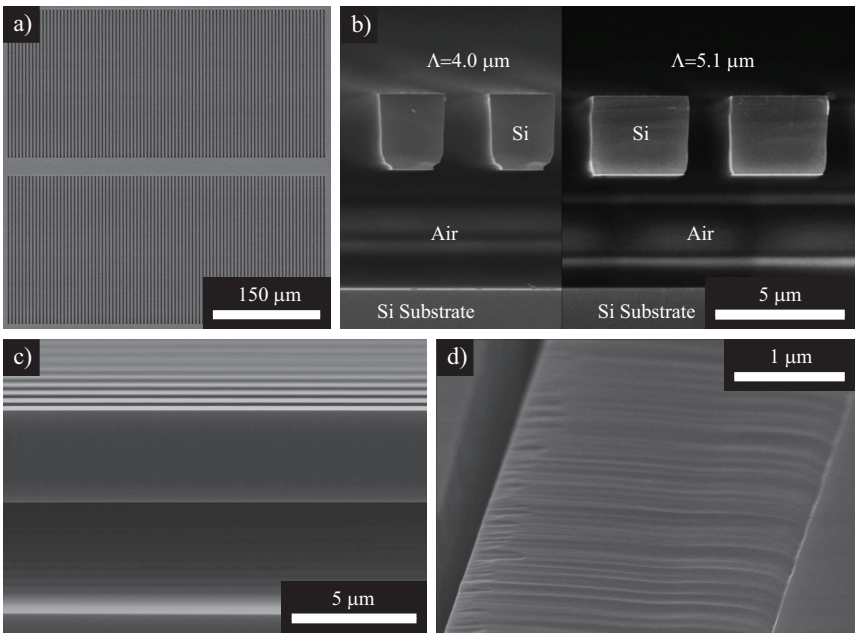


Figure 3.9: a) Fabricated single matrix element. b) Transverse cross sectional SEM micrographs of structures with over etched and optimally etched profiles resulting from open area etch dependence. c) Longitudinal oblique incident cross section of fabricated suspended structure. d) Sidewall roughness with striation pitch <100 nm.

3.9a and 3.9b contain a plan view of a single matrix element showing the redundant grating structure and a transverse cross sectional view of two suspended structures. These transverse cross sectional images were procured by cleaving samples prior to suspension to ensure mechanical stability during sample preparation. Extracted as-built dimensions, $t$ and $h$, were taken from gratings adjacent to those experimentally tested due to the destructive nature of the imaging procedure. The etch rate dependence on open area is evident in Figure 3.9b with over etching for the $\Lambda = 4.0$ $\mu$m period structure while the $\Lambda = 5.1$ $\mu$m structure possesses nearly vertical sidewalls with little over etching. Figures 3.9c and 3.9d show a longitudinal cross sectional image and a representative side surface roughness profile, respectively. Bowing and adhesion of the grating structures were found to be imperceptible using available imaging analysis and the surface roughness striations of Figure 3.9d have less than a 100 nm pitch.

The characterization of these gratings was performed using the same FTIR system

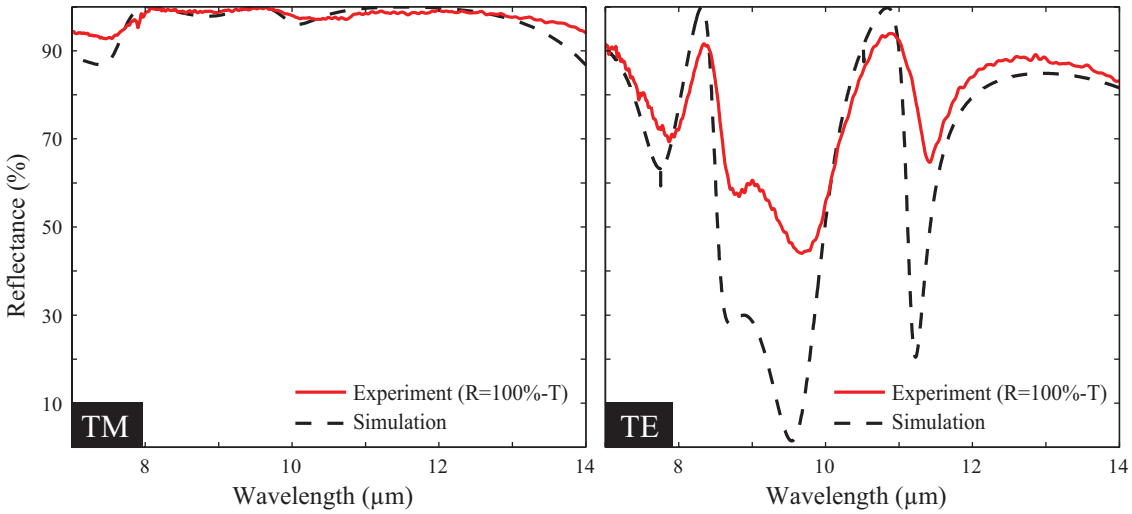


Figure 3.10: Experimental demonstration of broadband reflector at normal incidence for TM polarization and the accompanying response for TE polarization.

used to characterize the $Si/SiO_2$ gratings. The sample was tilted (20°) using a custom sample holder (see Chapter I) to ensure an area of the Cassegrain objective incident light propagated normal to the grating surface. An optical iris was used to constrain the light to nearly normal incidence. The response was 512 scan-averaged over a characterized area of 250 × 150 $\mu$m. Because the reflectance could not be directly measured using the Cassegrain objectives, the reflectance was calculated from the transmittance ($R = 100\% - T$) and compared to the simulated response. Figure 3.10 shows the experimental ($R = 100\% - T$) and simulated TM polarization broadband reflectance, as well as the TE polarization response for a grating with: $\Lambda = 4.9$ $\mu$m, $t = 2.85$ $\mu$m, $h = 4.05$ $\mu$m, and $FF = 78\%$.

For the TM polarization response, the agreement between the simulated reflectance and the experimental response is strong, with reflectance greater than 90% across the entire LWIR. Below 8 $\mu$m and above 13 $\mu$m the experimental reflectance is higher than the simulated response. This is a consequence of the additional reflection at the exit plane of the substrate and the absorption in the 500 $\mu$m thick substrate. The TE response suggests there is higher absorption loss within the substrate than is accounted for in the simulations, which do not include the 500 $\mu$m substrate. However,

because the reflectance for TM polarization is very close to 100%, the total light absorbed is expected to be small. This is corroborated by the strong agreement between the simulated and experimental responses when the reflectance is near 100%, which then deviates as the reflectance drops outside the LWIR spectrum. The strong agreement between simulation and experiment suggests the reflector demonstrates greater than 90% reflectance across the LWIR spectrum.

## 3.3 Summary

In this chapter, we have provided designs, experimental evidence and computational analyses to support the demonstration of broadband LWIR optical reflectors based on $Si/SiO_2$ and Si/air gratings. The $Si/SiO_2$ grating exhibits polarization dependent broadband reflectance across the spectral range 13 $\mu$m $< \lambda <$ 16 $\mu$m with $\Delta\lambda/\lambda = 18.5\%$ for reflectance values greater than 70% and an average extinction ratio of 1:1.6. Computational reflectance spectra incorporating wavelength dependent material optical properties agree well with the experimental results, which is limited by strong absorption in the $SiO_2$ layer. Re-optimization of the grating incorporating the material dispersion relations suggest a different system is required for realizing broadband reflectance in the LWIR above 90%.

Subsequent optimization and fabrication of a Si/air grating, which removes the lossy $SiO_2$ layer, demonstrated normal incidence broadband reflectance greater than 90% across the entire LWIR. These structures are attractive candidates for acting as lossless broadband reflectors in Fabry-Pérot etalons.

# CHAPTER IV

# Oblique Incidence Broadband Reflector

In addition to normal incidence broadband reflectance, high contrast gratings can be optimized to exhibit broadband reflectance away from normal incidence.[44] In this chapter we discuss a broadband reflector operating at oblique incidence. We provide an experimental demonstration of broadband reflectance and investigate its dependence on polarization, fill factor, and over etching.

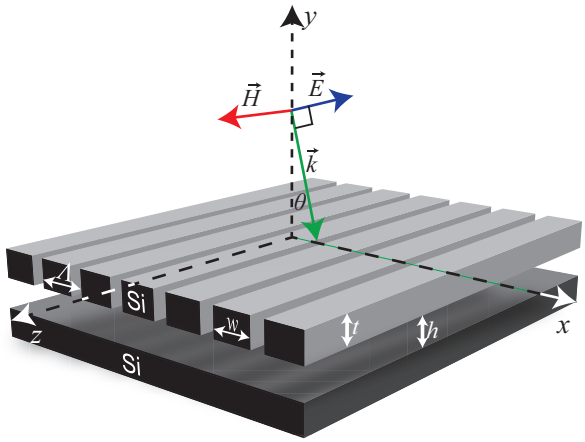


Figure 4.1: A three-dimensional schematic of a suspended silicon grating with field and incident angle ($\theta$) defined.

The suspended silicon grating demonstrating normal incidence broadband reflectance from Chapter IV forms the basis for this study. At oblique incidence, however, the grating dimensions must be changed to accommodate a different set of mode coupling considerations. Figure 4.1 illustrates the grating structure with the

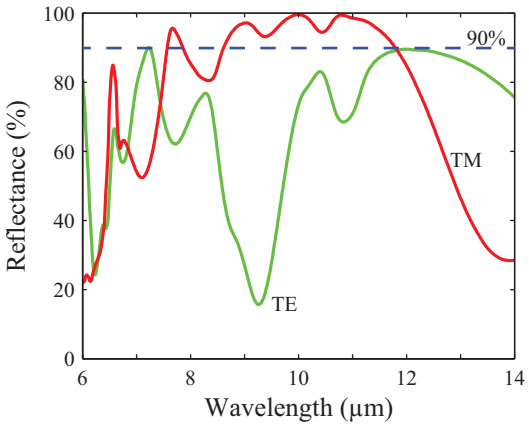


Figure 4.2: Polarization dependent field response of a suspended silicon grating with dimensions: $\Lambda = 4.15$ $\mu$m, $t = 3.05$ $\mu$m, $h = 4.1$ $\mu$m, and $FF = 61\%$.

incident angle ($\theta$) and polarization defined. The oblique incidence reflector, like the previous normal incidence reflectors, operates under TM polarization.

The photolithography mask affords a large array of gratings with different dimensions, which enables many experimental studies to be conducted from a single fabrication run. SEM micrographs of a representative fabricated grating can be seen in Figure 3.9 of Chapter III. To investigate the reflectance away from normal incidence, we leveraged the Cassegrain objective to provide $\pi$-radians of incident light between 16 and 36°. The response was averaged over 32 scans with a characterized area of $200 \times 150$ $\mu$m.

Figure 4.2 shows the measured reflectance for TM and TE polarizations of a grating with: $\Lambda = 4.15$ $\mu$m, $t = 3.05$ $\mu$m, $h = 4.1$ $\mu$m, and $FF = 61\%$. The grating exhibits broadband reflectance greater than 85% between 8.5 $\mu$m and 12 $\mu$m corresponding to a bandwidth of $\Delta\lambda/\lambda = 34\%$. For reflectance greater than 90%, the bandwidth is 31% over the spectral range 8.6 $\mu$m to 11.7 $\mu$m. These reflectance bandwidths and magnitudes are sufficient to produce Fabry-Pérot etalons with narrower than 0.5 $\mu$m full width half maximum (FWHM) transmission bands.

## 4.1 Polarization Dependence

The field response exhibits strong polarization dependence as a consequence of the grating's one-dimensional design. To study this dependence, reflectance measurements with 5° polarizer setting increments were performed where 0° and 90° correspond to TE and TM polarizations, respectively. Figure 4.3a shows a contour plot of the reflectance as a function of the polarizer angle. Figure 4.3b shows a line plot associated with the reflectance at $\lambda = 9.3$ $\mu$m, where the largest discrimination between TE and TM polarization occurs. While large deviations from either TM or TE polarization result in significant changes to the reflectance profile, the response is insensitive to deviations in the alignment of the polarizer as large as 10°. This insensitivity is attractive for applications where alignment of the gratings with a polarizer may be needed.

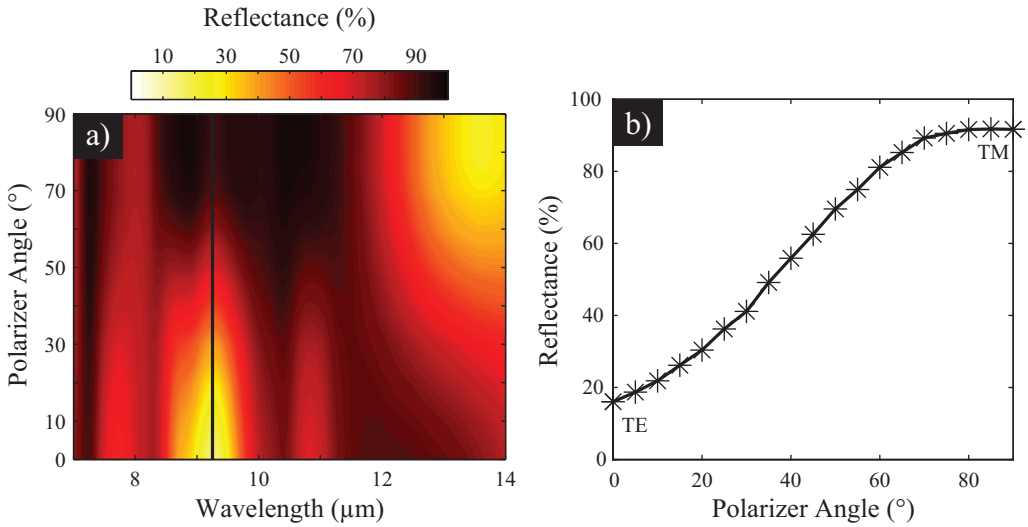


Figure 4.3: Experimental polarization dependent field response of the suspended silicon grating with 0° and 90° corresponding to TE and TM polarizations, respectively and dimensions: $\Lambda = 4.15$ $\mu$m, $t = 3.05$ $\mu$m, $h = 4.1$ $\mu$m, and $FF = 61\%$ for a) the LWIR spectrum and b) the maximum deviation within the LWIR at 9.3 $\mu$m.

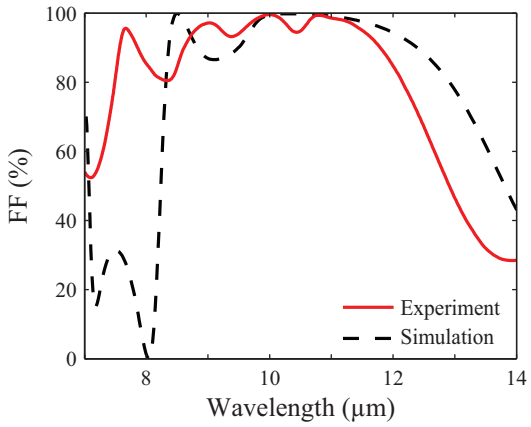


Figure 4.4: Comparison between experiment and as-built simulations at $\theta = 15°$ oblique incidence for a grating with: $\Lambda = 4.15$ $\mu$m, $t = 3.05$ $\mu$m, $h = 4.1$ $\mu$m, and $FF = 61\%$.

## 4.2 Finite Element Simulation Analysis

To analyze the experimental results using finite element simulations, an approximation of the incident light was used as a result of the half azimuth of incident light in reflectance mode. The response was simulated using oblique incidence plane wave excitation at $\theta = 15°$. Figure 4.4 shows the experimental and simulated response of the grating with dimensions: $\Lambda = 4.15$ $\mu$m, $t = 3.05$ $\mu$m, $h = 4.1$ $\mu$m, and $FF = 61\%$. The qualitative agreement between the datasets is strong, with similar reflectance signatures apparent in both datasets. The experimental data, however, is blue-shifted compared to the simulated response, which may be a consequence of the cassegrain objective focussing. An interesting feature is evident in both datasets around 8-9 $\mu$m, where an apparent resonance is present.

This resonance at 8.5 $\mu$m for the simulated response was further studied to elucidate the mechanism responsible for the broadband response. Figure 4.5a shows the dependence of the grating's reflectance as the incident angle is increased. Line plots associated with specific angles, shown in Figure 4.5b, further illustrate the resonant response. Interestingly, at normal incidence ($\theta = 0°$) the response does not exhibit any signature associated with the resonance. The mechanism responsible for this

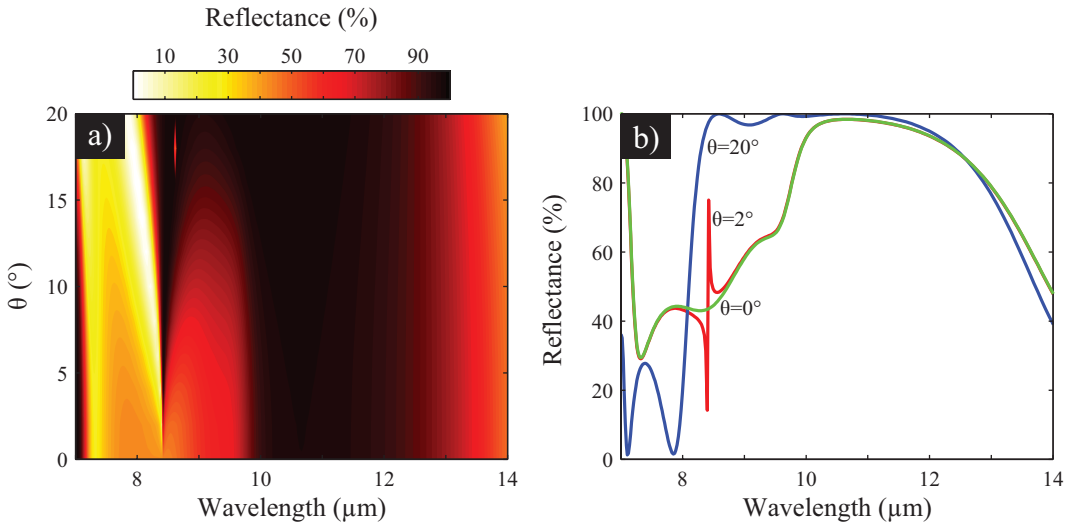


Figure 4.5: Simulated angular dependence of the grating reflectance with a) a contour plot from 0 to 20°, and b) line plots at select angles.

protected mode at normal incidence will be explained in later chapters, where similar modes are leveraged to realize transmission filtering capabilities.

Moving off normal incidence ($\theta = 2°$) results in coupling to this resonance, which broadens as the angle increases ($\theta = 20°$). The broadband reflectance is a consequence of the overlap between this resonance and the reflectance band centered at 11 $\mu$m. This agrees with a previous study on the mechanism of broadband reflectance exhibited by high contrast gratings.[63]

## 4.3 Fabrication Tolerances

To investigate the effects of fabrication tolerances, various over-etched profiles were simulated, including chamfers, circular profiles and the profile extracted from SEM micrographs. Figure 4.6 shows structures that were studied along with the field profile of the circular etched profile (dotted box) as the radius is increased. Over etching for all profiles was found to have little effect on the broadband reflectance for reasonable over etching dimensions, as seen in Figure 4.6b. A radius of 20% of the width of the grating exhibits nearly identical reflectance as the optimized

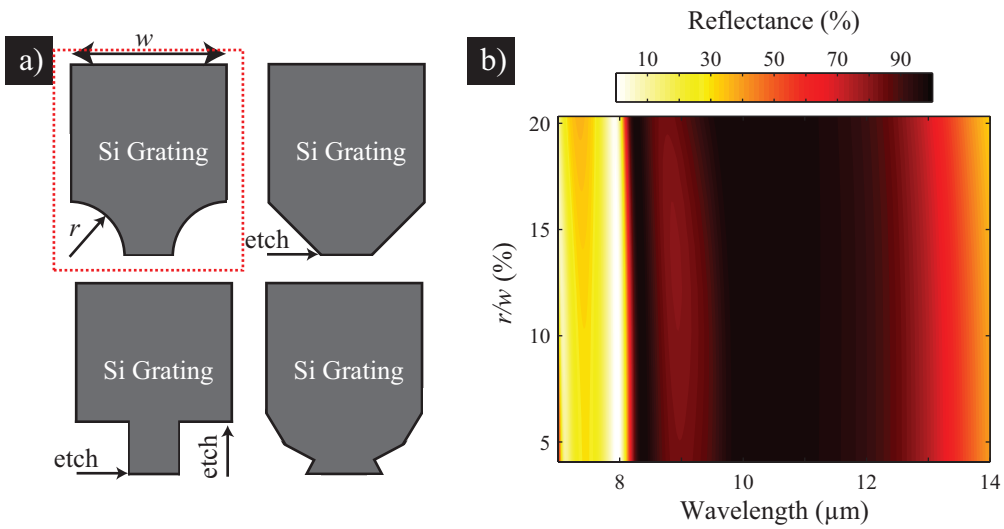


Figure 4.6: a) Representative grating profiles used for over etching analysis. b) Field response dependence on the over etched radius profile ($r/w$).

structure. This tolerance to fabrication inconsistencies is attractive, as it suggests the desired response of many different grating dimensions may be obtained from a single fabrication procedure despite some gratings being over etched.

We further characterized the reflectance by measuring its dependence on the grating fill factor. Figure 4.7 shows simulated and experimental parametric sweeps for fill factors from 59 to 67%. Both datasets exhibit a red-shift with increasing fill factor. However, the experimental response illustrates the effects of fabrication differences across several gratings fabricated from the same wafer at the same time. While broadband reflectance is demonstrated, there are variations in the experimental response that are not expected (i.e. response between $60\% < FF < 64\%$).

## 4.4 Summary

In this chapter we have extended the broadband reflectance operation of a suspended silicon grating to realize oblique incidence broadband reflectance. The TM response possesses greater than 85% reflectance between 8.5 $\mu$m and 12 $\mu$m with a bandwidth of 34%. The reflectance band shows little dependence on small polariza-

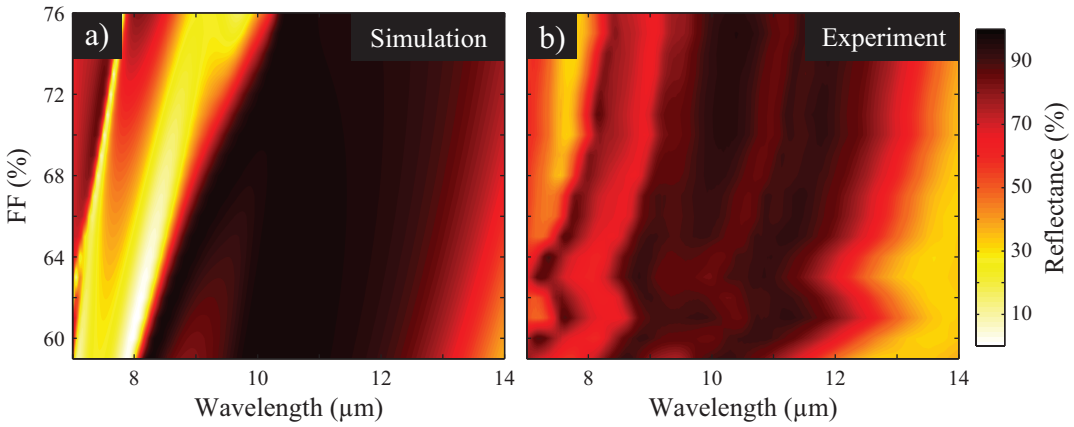


Figure 4.7: a) Simulated and b) experimental grating reflectance with changing fill factor.

tion deviations from TM polarization while large changes yield significant response disparity as expected from a one-dimensional grating. As-built structure simulations agree with experiment and display little dependence on structure over etching. Finally, an angular dependent analysis elucidates the resonant mechanism responsible for the broadband reflectance, where the mode is accessible at off-normal incidence but not at normal incidence.

# CHAPTER V

# Group Theoretical Analysis of Mode Coupling and its Application to Transmission Filtering in Dielectric Gratings

In the previous chapter we demonstrated broadband reflectance at oblique incidence where the response was shown to be a consequence of resonance coupling. In this chapter we use a group theoretical argument to predict mode coupling at normal and off-normal incidence that can be used to optimize the grating response. Anomalous dips in reflectance were recently reported in a single layer dielectric-grating mirror when using high numerical aperture lenses,[34] although a physical explanation was not provided at the time. In this work, we show that these narrowband features are based on two guided modes from the same diffraction order with radically different optical selection rules, requiring slightly off-normal incidence. We use this physical principle to predict a narrowband transmission filter based on a single-layer dielectric grating.

Figure 5.1 shows a schematic of the investigated dielectric grating and its associated Brillouin zone. For this analysis we express the grating parameters in terms of its relative permittivity ($\epsilon_g$), period ($\Lambda$), thickness ($t$), and fill factor ($FF$, defined as the ratio of the grating width to the grating period, $w/\Lambda$), as well as the surrounding material's relative permittivity ($\epsilon_s$), where the relationship between the material

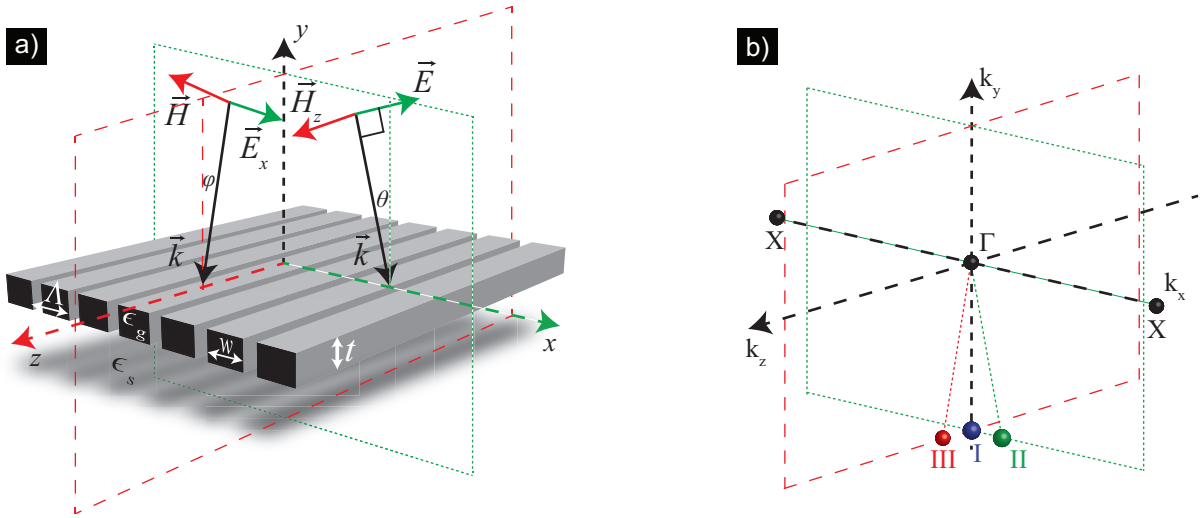


Figure 5.1: a) Grating schematic and b) its corresponding Brillouin zone with incident fields, dimensions, and material properties defined.

index of refraction and permittivity is given by $\epsilon = n^2$. We further assume lossless and non-magnetic materials ($\kappa = 0$, $\mu_g = \mu_s = 1$), where $\kappa$ is the material extinction coefficient and $\mu_g, \mu_s$ are the relative permeabilities of the materials. Plane waves are constrained with the electric field perpendicular to the $z$-axis ($\boldsymbol{E_{xy}}$, green-dotted plane) and the magnetic field perpendicular to the $x$-axis ($\boldsymbol{H_{yz}}$, red-dashed plane). A plane wave's incidence is defined by its angle with respect to the normal in the $xy$-plane ($\theta$) and $yz$-plane ($\varphi$). The grating's periodicity in the $x$-direction limits the extent of the first Brillouin zone in the $k_x$ direction while $k_y$ and $k_z$ remain unbounded. Strictly speaking, $k_y$ is not a good quantum number, as the system lacks translation symmetry in the $y$-direction. We refer here to the far-field (plane-wave) wave vector of incident or radiated fields associated with the resonant modes, defined by $k_y^2 = \omega_{k_x,k_z}^2/c^2 - k_x^2 - k_z^2$. Analyzing the symmetry of the grating's supported modes and incident plane waves can help us leverage selective mode coupling to produce narrowband transmission filters using these structures. We will discuss mode coupling at normal incidence, Point I ($|k_y| > 0$, $\theta = \varphi = 0°$), and off-normal incidence in the $xy$- and $yz$-planes, Point II ($|k_y|, |k_x| > 0$, $\theta > 0°$, $\varphi = 0°$)) and Point III ($|k_y|$,$|k_z| > 0$, $\theta = 0°$, $\varphi > 0°$), respectively.

| $D_{2h}$ | $E$ | $C_{2z}$ | $C_{2y}$ | $C_{2x}$ | $i$ | $\sigma_z$ | $\sigma_y$ | $\sigma_x$ |
|---|---|---|---|---|---|---|---|---|
| $A_g$ | 1 | 1 | 1 | 1 | 1 | 1 | 1 | 1 |
| $B_{1g}$ | 1 | 1 | -1 | -1 | 1 | 1 | -1 | -1 |
| $B_{2g}$ | 1 | -1 | 1 | -1 | 1 | -1 | 1 | -1 |
| $B_{3g}$ | 1 | -1 | -1 | 1 | 1 | -1 | -1 | 1 |
| $A_u$ | 1 | 1 | 1 | 1 | -1 | -1 | -1 | -1 |
| $B_{1u}$ | 1 | 1 | -1 | -1 | -1 | -1 | 1 | 1 |
| $B_{2u}$ | 1 | -1 | 1 | -1 | -1 | 1 | -1 | 1 |
| $B_{3u}$ | 1 | -1 | -1 | 1 | -1 | 1 | 1 | -1 |

Table 5.1: $D_{2h}$ character table corresponding to the Γ-point of the grating's reciprocal lattice.

## 5.1 Group Theoretical Analysis

The grating belongs to the $D_{2h}$ point group, which leaves the grating unchanged for transformations including $\pi$ rotations ($C_{2x}$, $C_{2y}$, $C_{2z}$), reflections ($\sigma_x$, $\sigma_y$, $\sigma_z$), and inversion ($i$). The $D_{2h}$ character table shown in Table 5.1 includes these transformations along with the group's irreducible representations. As a consequence of belonging to the $D_{2h}$ point group, the grating's supported modes at the Γ-point ($\boldsymbol{k} = 0$) have the same symmetry as the point group's irreducible representations.[54] To facilitate a group theoretical analysis, we calculated the dispersion relations for the grating using finite element methods. The modal analysis calculates the complex propagation constant using the weak formulation of the Helmholtz equation expressed as a quadratic eigen-value problem.[88,90] The resulting dispersion relations for TM modes and the associated field profiles for several resonances are shown in Figure 5.2 for a grating with: $\frac{t}{\Lambda} = 0.6$, $FF = 0.72$, $\epsilon_g = 11.7$, and $\epsilon_s = 1$. The dispersion relations show the guided modes, with solid bands representing modes that were calculated using the modal analysis. The dashed bands, in contrast, were estimated from scattering analysis due to their imaginary propagation constants being larger than the Brillouin zone, which makes them difficult to accurately calculate. Because of the grating periodicity in one direction, the dispersion relations are represented in a reduced zone scheme with the index contrast between the grating and surrounding material lifting the de-

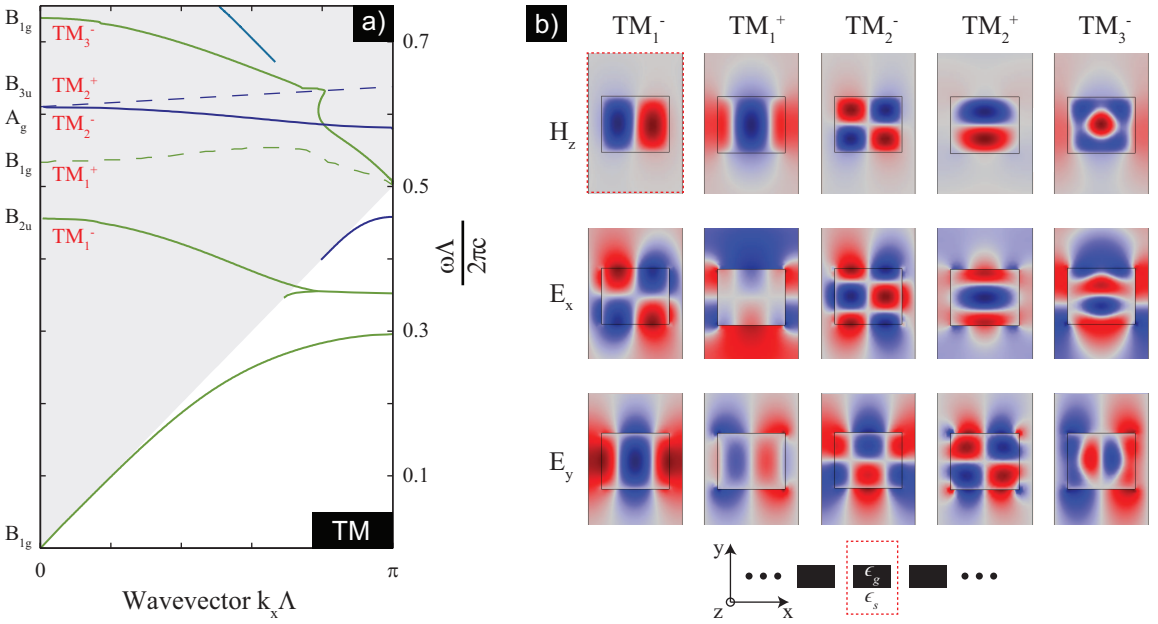


Figure 5.2: TM dispersion relations and field profiles for a grating with $\frac{t}{\Lambda} = 0.6$, $FF = 0.72$, $\epsilon_g = 11.7$, and $\epsilon_s = 1$. a) The dispersion relations include even (blue) and odd (green) bands with respect to a mirror reflection across the $xz$-plane. Solid bands were calculated using finite element modal analysis and dashed bands were estimated from scattering analysis. The modes at $k_x = 0$ are labeled with their $\Gamma$-point ($D_{2h}$ symmetry) irreducible representations and band definitions. The light cone is shown in light gray. b) TM mode field profiles at $k_x = 0$ with a black line indicating the boundary between high and low permittivity regions. Below: grating simulation element, and directions defined.

generacies at the zone boundaries ($k_x = \frac{\pi}{2}$) and zone center ($\boldsymbol{k} = 0$). The modes at zone center ($\boldsymbol{k} = 0$) are labeled with their irreducible representations, determined by using a reduction procedure[54] and by applying the symmetry operations of the $D_{2h}$ point group to the simulated mode field profiles. These modes, with the exception of the zero-frequency mode, lie within the light cone as a consequence of the photonic crystal's slab design. Hence, phase matching is possible between these modes and incident light. The lowest order leaky mode, $\mathrm{TM}_1^-$, belongs to the $B_{2u}$ irreducible representation. This mode is anti-symmetric upon rotation about the $z$-axis ($C_{2z}$) and reflection across the $xz$-plane ($\sigma_y$), and symmetric upon reflection across the $yz$-plane ($\sigma_x$), remembering the magnetic field is a pseudo-vector. We will show that at normal incidence a TM polarized plane wave cannot excite modes of this symmetry.

A normally incident TM polarized plane wave, $|k_y| > 0$, shown as Point I in Figure 5.1b, belongs to the reduced symmetry of the $C_{2v}^{y}$ point group, where the superscript $y$ indicates the symmetric rotation axis. The symmetry operations of this group ($E$, $C_{2y}$, $\sigma_z$, and $\sigma_x$) are summarized with the group's irreducible representations in Table 5.2(a). A wave with this polarization can couple to TM (but not TE) guided modes in the grating. For this coupling to occur, the phase matching condition must be met and the overlap integral between the incident field and the supported mode must be non-zero; this requires the mode and incident wave to belong to the same irreducible representation. The compatibility relations between Point I and the Γ-point, determined by comparing the character tables for the relevant symmetry operations, give their mutual irreducible representations. These relations, summarized in Table 5.2(b), show that each mode at Point I ($C_{2v}$ point group) maps onto two modes at the Γ-point ($D_{2h}$ point group). The incident TM plane wave of Point I belongs to the $B_1$ irreducible representation, which matches the symmetry of the $B_{1g}$ and $B_{3u}$ Γ-point irreducible representations at Point I. This plane wave, thus, can couple to modes that belong to these two irreducible representations at the Γ-point while the other modes are inaccessible or symmetry-protected; explicitly, modes $\mathrm{TM}_1^+$, $\mathrm{TM}_2^+$, and $\mathrm{TM}_3^-$ of Figure 5.2 are all accessible at normal incidence, while modes $\mathrm{TM}_1^-$ and $\mathrm{TM}_2^-$ are symmetry-protected. This symmetry matching is illustrated by the $x$-component of the electric field intensity shown in Figure 5.2b;

(a)

| $C_{2v}$ | $E$ | $C_{2y}$ | $\sigma_z$ | $\sigma_x$ |
|---|---|---|---|---|
| $A_1$ | 1 | 1 | 1 | 1 |
| $A_2$ | 1 | 1 | −1 | −1 |
| $B_1$ | 1 | −1 | 1 | −1 |
| $B_2$ | 1 | −1 | −1 | 1 |

(b)

| Point I | Γ |
|---|---|
| $A_1$ | $A_g$ , $B_{2u}$ |
| $A_2$ | $B_{2g}$ , $A_u$ |
| $B_1$ | $B_{1g}$ , $B_{3u}$ |
| $B_2$ | $B_{3g}$ , $B_{1u}$ |

Table 5.2: a) $C_{2v}^{y}$ character table and b) the compatibility relations between Point I and the Γ-point.

(a)

| $C_s^{xy}$ | $E$ | $\sigma_z$ |
|---|---|---|
| $A'$ | 1 | 1 |
| $A''$ | 1 | -1 |

(b)

| Point II | $\Gamma$ |
|---|---|
| $A'$ | $A_g$ , $B_{1g}$ , $B_{2u}$ , $B_{3u}$ |
| $A''$ | $A_u$ , $B_{2g}$ , $B_{3g}$ , $B_{1u}$ |

Table 5.3: a) $C_s^{xy}$ character table and b) the compatibility relations between Point II and the $\Gamma$-point.

modes $\mathrm{TM}_1^+$, $\mathrm{TM}_2^+$, and $\mathrm{TM}_3^-$ share plane wave symmetry in the $x$-direction while modes $\mathrm{TM}_1^-$ and $\mathrm{TM}_2^-$ are anti-symmetric in comparison.

To access the symmetry-protected modes, the incident wave vector can be moved off the $k_y$ axis to Point II, which is maintained in the $k_xk_y$-plane. Point II has the further reduced symmetry of the $C_s^{xy}$ point group, with symmetry only upon reflection across the $xy$-plane, $\sigma_z$. The $C_s^{xy}$ character table and the compatibility relations between Point II ($C_s^{xy}$ point group) and the $\Gamma$-point ($D_{2h}$ point group) are given in Tables 5.3(a) and 5.3(b). This reduced symmetry relaxes the selection rules, illustrated by the mapping of four $\Gamma$-point irreducible representations onto each irreducible representation at Point II. An incident TM plane wave belongs to the $A'$ irreducible representation. All the TM modes considered at Point II share this irreducible representation. Consequently, the modes that are symmetry-protected at normal incidence can now couple to this off-normal incidence plane wave.

If instead we consider a plane wave with wave vector at Point III of Figure 5.1, we maintain symmetry across the $yz$-plane, $\sigma_x$, and introduce a $y$-component of the magnetic field ($H_y$) to the plane wave. In addition to exciting TM modes, this

(a)

| $C_s^{yz}$ | $E$ | $\sigma_x$ |
|---|---|---|
| $A'$ | 1 | 1 |
| $A''$ | 1 | -1 |

(b)

| Point III | $\Gamma$ |
|---|---|
| $A'$ | $A_g$ , $B_{3g}$ , $B_{1u}$ , $B_{2u}$ |
| $A''$ | $A_u$ , $B_{1g}$ , $B_{2g}$ , $B_{3u}$ |

Table 5.4: a) $C_s^{yz}$ character table and b) the compatibility relations between Point III and the $\Gamma$-point.

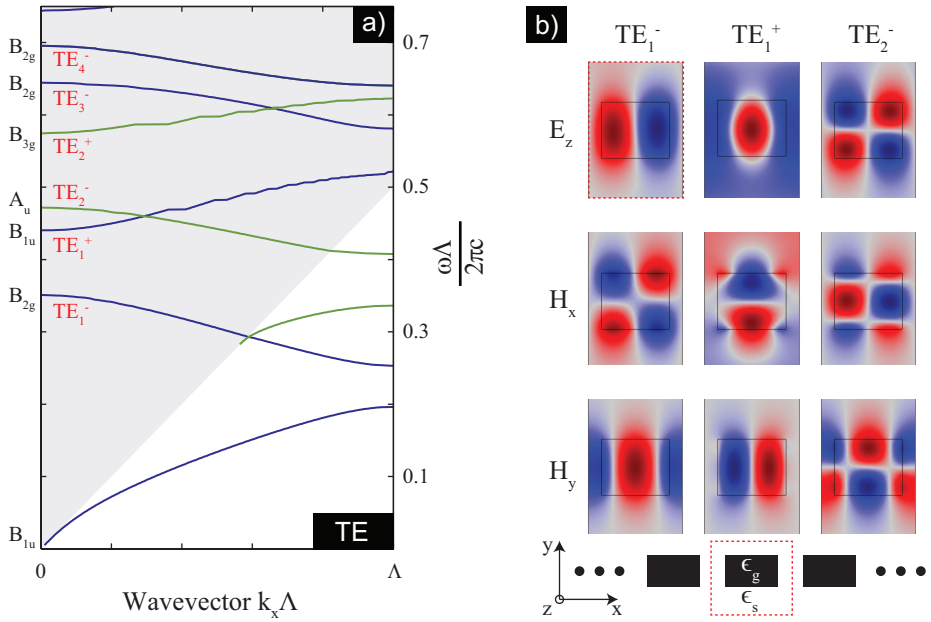


Figure 5.3: TE dispersion relations and select field profiles for a grating with $\frac{t}{\Lambda} = 0.6$, $FF = 0.72$, $\epsilon_g = 11.7$, and $\epsilon_s = 1$. a) The dispersion relations include even (blue) and odd (green) bands with respect to a mirror reflection across the $xz$-plane. The modes at $k_x = 0$ are labeled with their Γ-point ($D_{2h}$ symmetry) irreducible representations and band definitions. The light cone is shown in light gray. b) TE mode field profiles at $k_x = 0$ with a black line indicating the boundary between high and low permittivity regions. Below: grating simulation element, and directions defined.

wave can couple to TE guided modes, provided they have the appropriate symmetry. Accordingly, the grating's TE dispersion relations were calculated using the modal analysis and are shown in Figure 5.3 with field profiles of select modes illustrated. The $C_s^{yz}$ character table and the compatibility relations between Point III ($C_s^{yz}$ point group) and the Γ-point ($D_{2h}$ point group) are shown in Tables 5.4(a) and 5.4(b). At Point III the incident plane wave belongs to the $A''$ irreducible representation of the $C_s^{yz}$ point group. This irreducible representation shares the symmetry of several guided modes at Point III. Thus, coupling to $\mathrm{TE}_1^-$, $\mathrm{TE}_2^-$, $\mathrm{TE}_3^-$, and $\mathrm{TE}_4^-$ is allowed while modes $\mathrm{TE}_1^+$ and $\mathrm{TE}_2^+$ remain symmetry-protected due to their anti-symmetry in $H_y$ across the $yz$-plane. To couple to these additional modes, the $x$-symmetry must also be broken, which could be achieved by introducing an additional $k_x$ component to the wave vector. A summary of the permissible mode coupling for incident plane

| Modes | $TM_1^-$ | $TM_1^+$ | $TM_2^-$ | $TM_2^+$ | $TM_3^-$ | $TE_1^-$ | $TE_1^+$ | $TE_2^-$ | $TE_2^+$ | $TE_3^-$ | $TE_4^-$ |
|---|---|---|---|---|---|---|---|---|---|---|---|
| Point I | | X | | X | x | | | | | | |
| Point II | x | X | x | X | x | | | | | | |
| Point III | | X | | X | x | x | | x | | x | x |

Table 5.5: Summary of the allowable mode coupling for a TM polarized plane wave with various incident wave vectors. 'X' indicates relatively strong coupling, while 'x' indicates relatively weak coupling.

waves with wave vectors at Points I, II and III is given in Table 5.5.

## 5.2 Transmission Filtering Capabilities

This selective mode coupling has been leveraged to realize transmission filters using a dielectric grating. The operating principle, which has also been used in previously proposed dielectric transmission filter designs, involves coupling the incident light to two grating modes that overlap in frequency and have different coupling strengths. The strongly coupled mode produces a broad reflectance resonance, and Fano interference with the weakly coupled mode produces a narrow transmission peak within this high reflectance background. Previous proposals achieved the overlapping strong and weak resonances by coupling modes of different diffractive orders,[75] using asymmetric grating structures,[22] or combining a grating with additional resonant structures.[21,36,67] In contrast to these methods, we exploit symmetry-protected modes of a single diffraction order to achieve the required coupling strength disparity.

Figure 5.4 shows the simulated transmittance profiles in the $k_x$ and $k_z$ directions, or moving towards Points II and III, respectively, for the transmission filter design discussed below. The imaginary part of the propagation constant, determined from the modal analysis, represents the coupling strength to the radiation field; a large (small) value results in fast (slow) decay and consequently a broadband (narrowband) response. The width of a given resonance can be expressed by its quality factor, $Q = \frac{\omega}{\Delta\omega}$, and is related to the energy decay within the mode

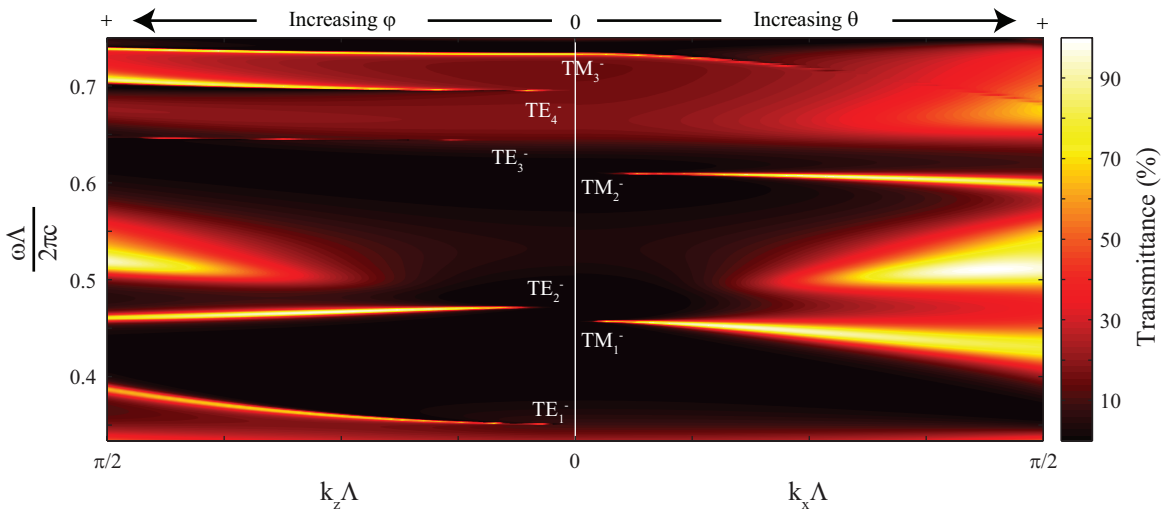


Figure 5.4: Simulated grating transmittance profile at normal and off-normal incidence. $k_x = 0$, $|k_x| > 0$, and $|k_z| > 0$ correlates to Points I, II, and III, respectively. The top scale shows increasing $\theta$ and $\varphi$ directions corresponding to $|k_x| > 0$, and $|k_z| > 0$, respectively. Transmission bands are labeled with the mode associated with the resonance.

given by $U(t) = U(t_0)\exp[-\frac{\omega(t-t_0)}{Q}]$.[54] We iteratively optimized the grating dimensions using finite element simulations to maximize the coupling strength to accessible TM modes at normal incidence, Point I, and consequently achieve a very low-$Q$ response. The structure consequently exhibits broadband reflectance greater than 95% for $0.357 < \frac{\omega\Lambda}{2\pi c} < 0.625$. The optimized structure dimensions are identical to those used for the dispersion relations of Figures 5.2 and 5.3, as well as the optimized broadband reflector of Chapter III: $\frac{t}{\Lambda} = 0.6$ and $FF = 0.72$. To facilitate the experimental demonstration discussed in the next chapter, we also included a substrate in the simulations separated from the grating by an air layer of thickness $\frac{h}{\Lambda} = 0.8$. This thickness is large enough to inhibit energy leakages from the grating. A permittivity of $\epsilon_g = 11.7$ was used for the grating and substrate, consistent with silicon in the infrared regime.[87] At normal incidence the low transmittance background is demonstrated (Figure 5.4) as a result of the optimized coupling to the $TM_1^+$ and $TM_2^+$ modes. From the group theoretical analysis we also expect coupling to mode $TM_3^-$, which is demonstrated as a narrow transmission band as a result of a small overlap

integral between the incident plane wave and mode. This small overlap integral can be inferred from the multiple nodes in the field profiles compared to an incident plane wave.

Away from normal incidence, $|k_x| > 0$ or $|k_z| > 0$, the relaxed selection rules enable coupling to the symmetry-protected modes. The broadband low-transmittance is maintained near $k_x = k_z = 0$ since the overlap integrals with the modes responsible for the response remain nearly constant, $\cos(\theta) \approx 1$. Within this broadband background, narrow transmission bands emerge as a result of weak coupling to the symmetry-protected modes. These transmission bands are labeled with the modes responsible for the resonant response. A perturbation to normal incidence will leave the mode profiles nearly identical to the zone center ($k_x = k_z = 0$) modes, ensuring the overlap integral remains small and the associated coupling is weak. Thus, resonant high-$Q$ transmission peaks are observed near normal incidence, and the peaks widen as $|k_x|$ or $|k_z|$ increases. Interestingly, the overlap integrals for the two sets of modes, TM and TE, result from different mechanisms. For TM mode coupling, the off-normal incidence results in non-zero overlap integrals for each field component, while TE mode coupling results from a small polarization overlap between the incident field and supported modes as a consequence of magnetic field-depolarization when $k_z$ is introduced.

The agreement between the simulated transmittance and the modal analyses is strong. The transmittance bands for $|k_x| > 0$ align exceptionally well with the dispersion relations of Figure 5.2, with deviations only observed for the estimated $\mathrm{TM}_1^+$ and $\mathrm{TM}_2^+$ bands. The transmittance bands associated with the TE modes are also in excellent agreement with the zone center ($\boldsymbol{k} = 0$) frequencies of the TE dispersion relations. Furthermore, the $\mathrm{TM}_3^-$ coupling responsible for the transmittance band at $\frac{\omega\Lambda}{2\pi c} = 0.72$ persists as $|k_z|$ is increased, explicitly showing how the TM mode coupling is maintained while TE mode coupling is introduced. Notably, one would expect the

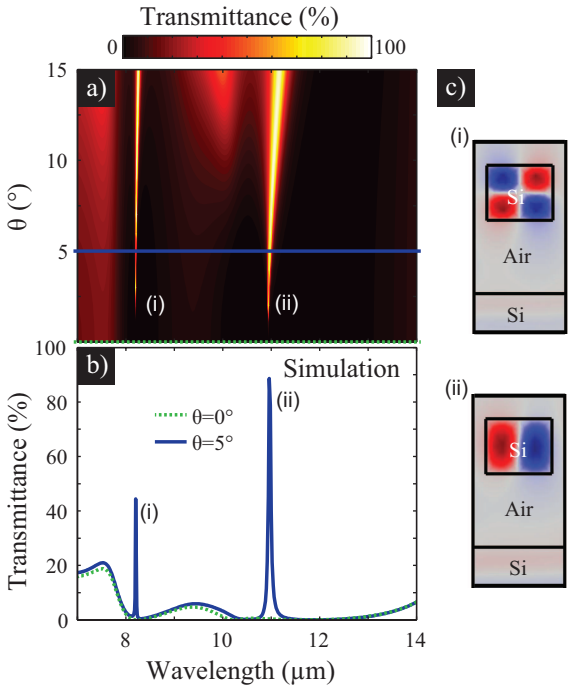


Figure 5.5: Simulated response of the optimized suspended silicon grating: $\Lambda = 5$ $\mu$m, $FF = 72\%$, $t = 3$ $\mu$m and $h = 4$ $\mu$m with a) a contour plot of transmittance as a function of increasing angle from normal, $\theta$ and b) respective line plots at normal incidence and $\theta = 5°$, with transmitted bands designated (i) and (ii). c) Magnetic field profiles, $H_z$, on each resonance showing the supported modes at $\theta = 5°$.

transmission bands for $|k_z| > 0$ to increase in frequency with increasing $|k_z|$ due to the lack of periodicity in the $z$-direction; however, both $\mathrm{TE}_2^-$ and $\mathrm{TE}_4^-$ transmission bands initially decrease in frequency away from normal incidence. We attribute this decrease to avoided crossings between these modes and the $\mathrm{TM}_1^+$ and $\mathrm{TM}_3^-$ modes, which have the same symmetry within the $C_s^{yz}$ point group and are slightly higher in frequency.

To illustrate the transmission filtering capabilities within the LWIR, Figure 5.5 shows the simulated response introducing a nonzero angle $\theta$. The contour plot shows the two transmission bands associated with coupling to the $\mathrm{TM}_1^-$ and $\mathrm{TM}_2^-$ modes. The bandwidths of the resonances increase as the angle increases as a consequence of the larger overlap integral between the guided mode and the incident plane wave. Corresponding line plots are shown in Figure 5.5b for normal incidence and $\theta = 5°$.

The discrimination from background is strong with transmittance expected to be less than 10% across the entire LWIR spectrum. Figure 5.5c shows the magnetic field profiles ($H_z$) associated with each of the transmission bands, which illustrate the eigensolutions responsible for the response.

### 5.2.1 Fano Resonance Fitting

The narrow transmittance bands within the broadband reflectance baseline are a consequence of interference between the guided modes of the dielectric grating. The asymmetric resonance lineshapes fit Fano theory,[62,93] suggesting the observed resonant response results from interference between strongly damped resonances and weakly damped resonances.[94] To better understand the operation of the filters, the resonant response for TM mode filtering was fit with a Fano-lineshape,

$$R = \frac{r^2(\omega - \omega_0)^2 + t^2(1/\tau)^2 \mp 2rt(\omega - \omega_0)(1/\tau)}{(\omega - \omega_0)^2 + (1/\tau)^2} \ , \tag{5.1}$$

where $R = r^2$ is the reflection coefficient ($r^2 + t^2 = 1$), $\omega$ is the frequency, $\omega_0$ is the resonant frequency, and $\tau$ is the resonance lifetime. The fitting parameters used were $\tau$, $\omega_0$ and $r$. The resulting fits with the simulated response are shown in Figure 5.6 for the optimized grating. The transmission bands are labeled with their associated modes ($TM_1^-$, $TM_2^-$, $TM_3^-$), which all exhibit strong agreement between the fit and simulated response. The only perceptible deviation occurs for the transmission band associated with $TM_3^-$ above 43.8 THz. This deviation is a consequence of an adjacent resonance that is affecting the response in the simulation.

Because Fano resonances are asymmetric, they must exhibit nearly perfect transmission as well as perfect reflection over the range of the resonance, assuming the materials are lossless. Consequently, if the resonance occurs in a low transmittance region of the spectrum, the response will yield a transmission filter. If instead, the

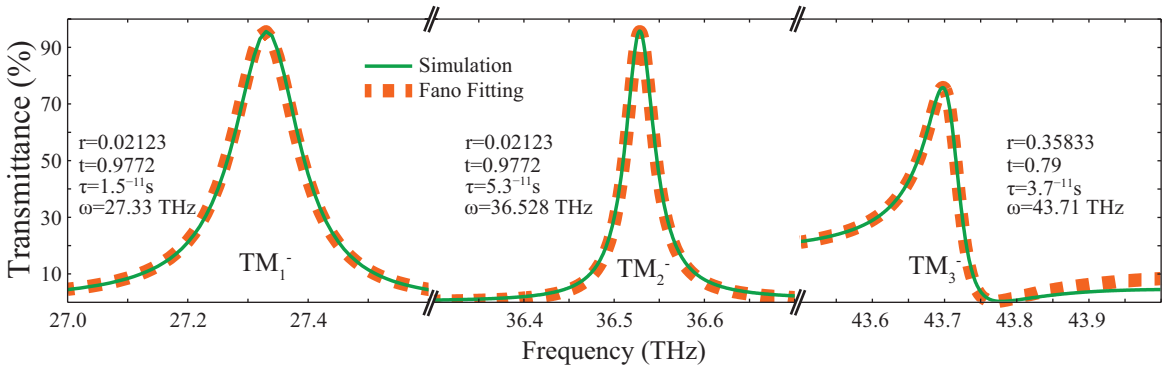


Figure 5.6: TM resonances fit with Fano-lineshapes at 5° from normal incidence.

resonance occurs in a low reflectance region, the resonance will result in a reflection filter.[20] It is because of this phenomenon that transmission filtering capabilities are expected; the optimized broadband reflector establishes the necessary condition for the Fano-resonance to demonstrate a narrow transmission band.

## 5.3 Summary

In this chapter we have introduced a group theoretical argument for plane wave coupling to supported modes of a dielectric grating and we have predicted transmission filtering capabilities through selective coupling to symmetry-protected modes at off-normal incidence. Using a group theoretical analysis, we determined the selection rules that govern plane wave coupling to the grating's supported modes at normal and off-normal incidence. We maximized the coupling strength to modes accessible at normal incidence to provide a low-transmittance background. Introducing a perturbation to normal incidence in the $k_x$ ($\theta > 0°$) or $k_z$ ($\varphi > 0°$) directions was shown to result in weak coupling to TM and TE symmetry protected modes. This weak coupling was shown to result in high-$Q$ transmission peaks within the low-transmittance background. The simulated response was fit to Fano theory, with the strong agreement suggesting the transmission filtering capabilities result from interference between strongly and weakly damped resonances. In the next chapter we will

discuss our experimental demonstration of the transmission filtering capability and characterize its operation.

# CHAPTER VI

# Experimental Demonstration of Transmission Filters

In the previous chapter we predicted transmission filtering capabilities using a group theoretical analysis with an accompanying computational study. At normal incidence, the grating has been optimized to act as a broadband reflector by maximizing the coupling strength to accessible modes. Other modes were shown to be inaccessible at normal incidence due to a mismatch in symmetry between the incident plane wave and the supported modes. Moving off normal incidence breaks the symmetry allowing weak coupling to the previously symmetry-protected modes. This results in narrow transmission peaks within the broadband opaque background. In this chapter we experimentally demonstrate the predicted filtering capabilities, which have potential to be used in LWIR hyperspectral imaging systems.

The experimental demonstration was based on a suspended silicon grating fabricated from an SOI substrate, and was designed to operate in the LWIR spectrum. Figure 6.1 shows SEM micrographs of a grating with $\Lambda = 5.1$ $\mu$m, $t = 2.85$ $\mu$m, $h = 4.05$ $\mu$m and $FF = 76\%$. To characterize the grating's electromagnetic response, we used a commercial FTIR spectrometer with a microscope attachment and a wire grid polarizer. Additionally, we used the custom-made sample holder and aperture to constrain the light from the microscope's Cassegrain objectives. The aperture lo-

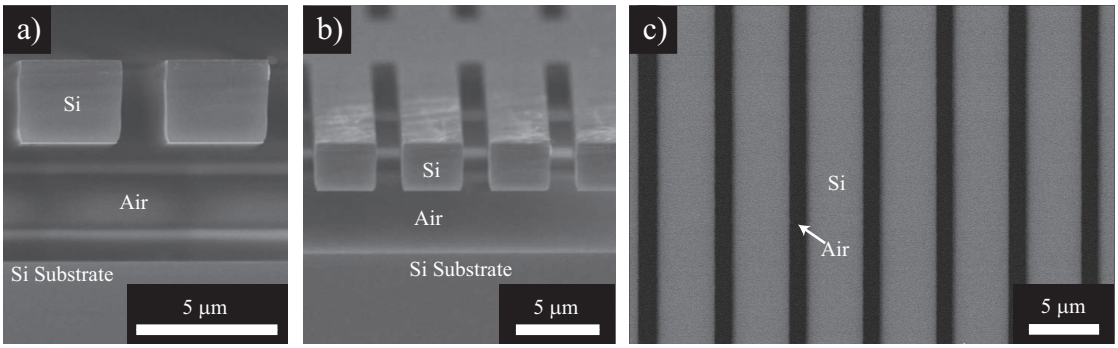


Figure 6.1: SEM micrographs of a suspended silicon grating with $\Lambda = 5.1$ $\mu$m, $t = 2.85$ $\mu$m, $h = 4.05$ $\mu$m and $FF = 76\%$ in a) cross sectional view, b) oblique incidence view, and c) plan view.

cation was manipulated using an $xyz$-translation stage with micrometer adjustment, which enabled independent control of the incident angles $\theta$ and $\varphi$ defined in Figure 5.1a of Chapter V. From the previous chapter, $\theta$ maintains the transversality of the magnetic field in the $z$-direction while $\varphi$ depolarizes the magnetic field and ensures the electric field is maintained the $x$-direction. Normal incidence light is indicated with $\theta = \varphi = 0^\circ$ and is designated as Point I, while off-normal incidence, Point II and Point III, correspond to introducing nonzero $\theta$ and $\varphi$, respectively.

Figure 6.2 shows the experimental and simulated transmittance for a grating with dimensions $\Lambda = 4.9$ $\mu$m, $t = 2.85$ $\mu$m, $h = 4.05$ $\mu$m and $FF = 72\%$ and incident light configurations analyzed in Chapter V: Points I, II, and III , as well as a fourth point, Point IV ($\theta$, $\varphi > 0^\circ$). In contrast to the preceding analyses that defined the incident wave using the wave vector, the experimental demonstration had the incident wave defined by $\theta$ and $\varphi$. As a consequence, the plot labels of Figure 6.2 do not represent a single point in $k$-space, but instead represent a range of incident wave vectors confined to the $k_x k_y$- and $k_y k_z$-planes for Points II and III, respectively.

In the absence of nonradiative losses, the quality factors of the peaks associated with the symmetry-protected modes are expected to increase infinitely as the incident light approaches normal incidence.[54] However, when the radiative coupling becomes less than the nonradiative losses, the peak height begins to decrease without apprecia-

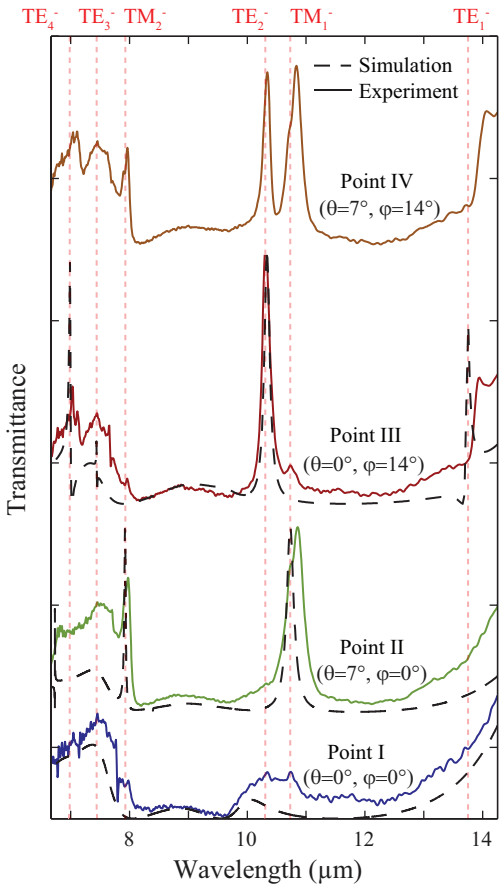


Figure 6.2: Experimental and associated simulated transmittance of a grating with various incident wave configurations. The as-built dimensions were $\Lambda = 4.9$ $\mu$m, $t = 2.85$ $\mu$m, $h = 4.05$ $\mu$m and $FF = 72\%$. Broadband reflectance, TM selective filtering, TE selective filtering and mixed TE and TM filtering associated with the incident wave vector at various points in the Brillouin zone: Point I ($\theta = \varphi = 0°$, Point II ($\theta = 7°$, $\varphi = 0°$), Point III ($\theta = 0°$, $\varphi = 14°$), and Point IV ($\theta = 7°$, $\varphi = 14°$), respectively.

ble further reductions in the peak width. The incidence angles reported in Figure 6.2 are those for which the nonradiative and radiative losses are of the same order of magnitude, as discussed further below.

At normal incidence, Point I ($\theta = \varphi = 0°$), transmittance below 7% is demonstrated between 8 and 13 $\mu$m. This is equivalent to the broadband reflector response of Chapter III. The corresponding simulated response has been reduced to 70% of its original value to account for the reflection loss at the output plane of the substrate, which was not simulated. The agreement between the two datasets is strong, with similar magnitude and features demonstrated for each.

Moving off normal incidence to Point II ($\theta = 7°$, $\varphi = 0°$) demonstrates two transmission bands associated with coupling to modes: $TM_1^-$ and $TM_2^-$. In this case the transmittance has been normalized to the peak transmittance of the experimental

results (26.0%) to accentuate the qualitative agreement between the datasets. The agreement in both the peak locations and line shapes is very strong, with the experimental response exhibiting moderate broadening and a small wavelength shift compared to the simulation that will be explained below.

Similarly, moving to Point III ($\theta = 0°$, $\varphi = 14°$) demonstrates selective coupling to TE modes that results in transmission bands with strong discrimination from background. Transmission bands associated with coupling to Modes $TE_1^-$ and $TE_2^-$ are clearly demonstrated while signatures of coupling to $TE_3^-$ and $TE_4^-$ are observed. The normalized simulated response (36.5%) agrees well with the experimental response.

For both TM and TE demonstrations, the transmission band frequencies are within 1% of those determined from the modal analysis, which is within the experimental error of measuring the grating dimensions. To ensure the resonant response results from two separate mode sets, we took data at Point IV ($\theta = 7°$, $\varphi = 14°$), which introduces $k_x$ and $k_z$ simultaneously. The corresponding data exhibit transmission bands associated with both TM and TE mode sets, confirming the independence of the mode coupling at Points II and III. At this further reduced symmetry of Point IV, we also expect resonant transmission bands associated with modes $TE_1^+$ and $TE_2^+$ as mentioned in Chapter V for TE mode coupling. Unfortunately, due to the small overlap integrals in both the $k_x$ and $k_y$ directions, the resulting quality factors were too high to be resolved experimentally. The line plots associated with Figure 6.2, which include resonance characteristics such as quality factor, peak transmittance, peak wavelength, and FWHM are included at the end of this chapter.

In the following sections we further analyze the filters' angular dependence, wavelength selection, and the effects of material absorption, and we compare the response to commercial LWIR hyperspectral imaging systems.

## 6.1 Angular Dependence

The theoretical analysis predicts angular dependence for the filtering capabilities, which includes both shifts in the filtered wavelength and line-width broadening as the incident angle increases. This angular dependence is a consequence of both the slope of the dispersion curves and changes in the overlap integral between a given supported mode and the continuum. Empirical analyses on the fabricated filters were performed to confirm this expectation and study the capabilities of the as-built structures.

Figure 6.3 illustrates the angular dependence of the filtering response, which was measured by varying the location of the constraining aperture in the $xz$-plane. The four subfigures top-left to bottom-right follow a clockwise analysis as $\theta$ and $\varphi$ are introduced and removed. The coupled modes responsible for the transmission filtering bands are indicated with dotted lines to clarify the modes responsible for the transmission bands. The top-left subfigure shows the grating response as ($\theta$) is increased from 0° while keeping $\varphi = 0°$. As the angle is increased the resonances associated with $\mathrm{TM}_1^-$ and $\mathrm{TM}_2^-$ modes become evident. However, the response does not become well defined until $\theta = 7°$ as a consequence of nonradiative losses within the system. The top-right subfigure maintains $\theta = 14°$ while increasing $\varphi$ from 0°, which similarly results in the introduction of the additional transmission band associated with the $\mathrm{TE}_2^-$ resonance. The bottom-right and bottom-left subfigures then show the response as $\theta \to 0°$, turning off the TM-mode related transmission bands and $\varphi \to 0°$ turning off the transmission bands associated to the TE mode, respectively. These subfigures further demonstrate the independence of the coupling mechanism to the two guided mode sets, TM and TE.

For each dataset of Figure 6.3 the filtered wavelength, resonance quality factor, and resonance FWHM were extracted to further characterize the transmission filtering capabilities. The most attractive transmittance bands for filtering applications are those corresponding to the $\mathrm{TE}_2^-$ and $\mathrm{TM}_1^-$ modes since they have the highest

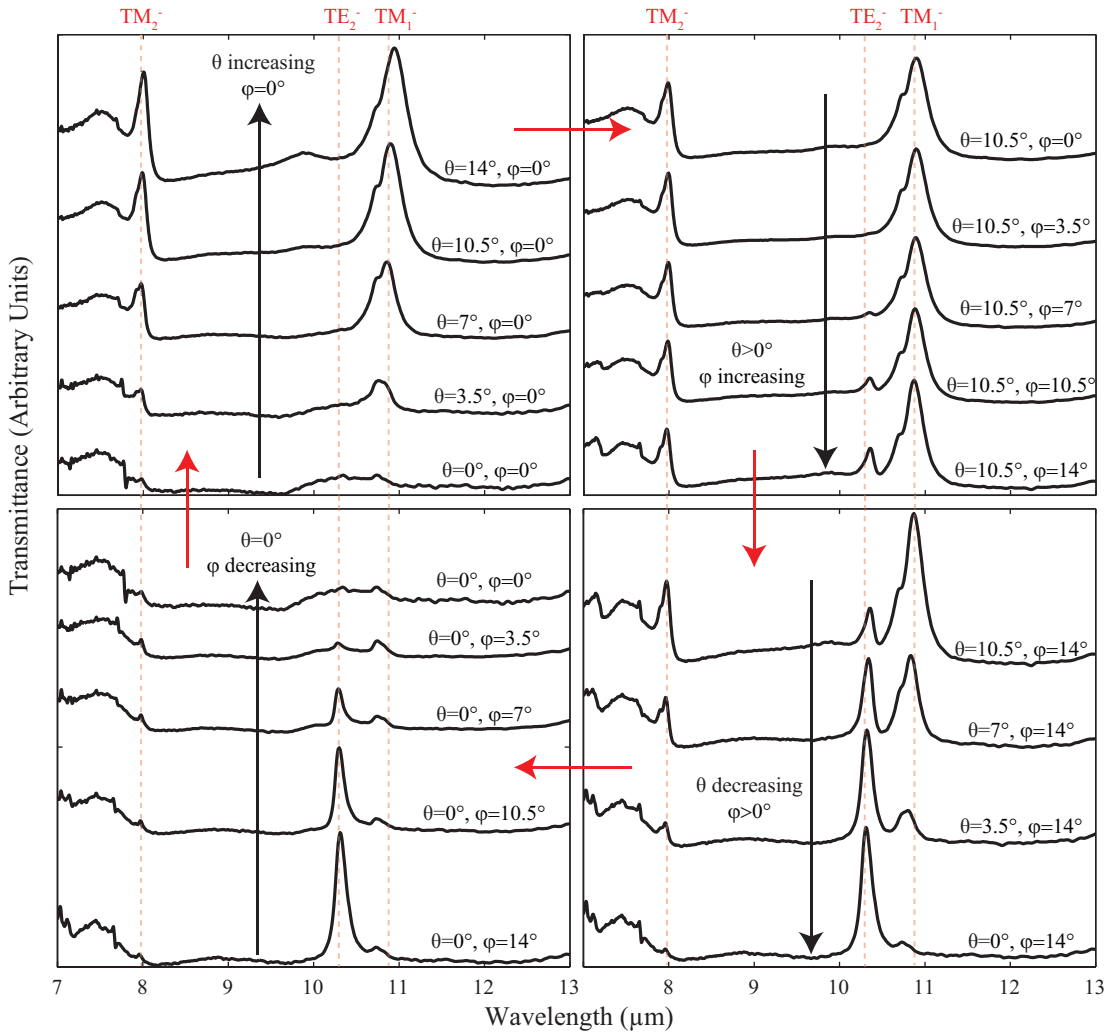


Figure 6.3: Angular dependence of transmission filtering capabilities. The response is shown for (top-left) $\theta$ increasing with $\varphi = 0°$, (top-right) $\theta > 0°$ with increasing $\varphi$, (bottom-right) $\theta$ decreasing with $\varphi > 0°$, and (bottom-left) $\theta = 0°$ with $\varphi$ decreasing. The as-built dimensions were $\Lambda = 4.9$ $\mu$m, $t = 2.85$ $\mu$m, $h = 4.05$ $\mu$m and $FF = 0.72$.

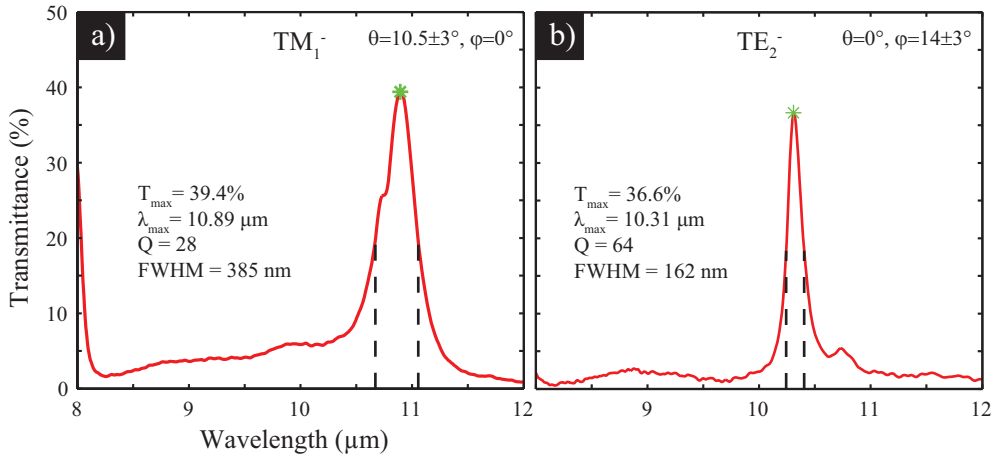


Figure 6.4: Transmission filtering response illustrating the FWHM, peak wavelength and extracted quality factor at a) $\theta = 10.5°$ and $\varphi = 0°$ and b) $\theta = 0°$ and $\varphi = 14°$ for a grating with dimensions $\Lambda = 4.9$ $\mu$m, $t = 2.85$ $\mu$m, $h = 4.05$ $\mu$m and $FF = 0.72$.

transmittance and are centered in the LWIR. Accordingly, these two resonances were studied. Figure 6.4 shows representative resonance profiles for $TM_1^-$ and $TE_2^-$ associated bands with the FWHM, peak wavelength, and quality factor labeled; this data was extracted from each experimental dataset, as well as for the as-built simulations. The transmission band associated with the TE mode exhibits a significantly higher quality factor compared to that associated with the TM mode, despite being characterized at a larger angle. This suggests the symmetry of the $TM_1^-$ mode may be more similar to an incident plane wave than the $TE_2^-$, resulting in a larger overlap integral and thus a broader response.

Figure 6.5 shows the quality factor and peak wavelength dependence on the incident angle for the $TM_1^-$ and $TE_2^-$ designated transmission bands. All data is included at the end of the chapter. Figure 6.5a shows the peak wavelength for each transmission band including the as-built simulated responses (dotted lines). There is strong agreement between the experimental and simulated filtered wavelength for both transmission bands, including peak location and slope of the response. The slope of the response is a consequence of the dispersion relations associated with each resonance (see Figure 5.2 and Figure 5.3). The slope of the $TM_1^-$ mode associated

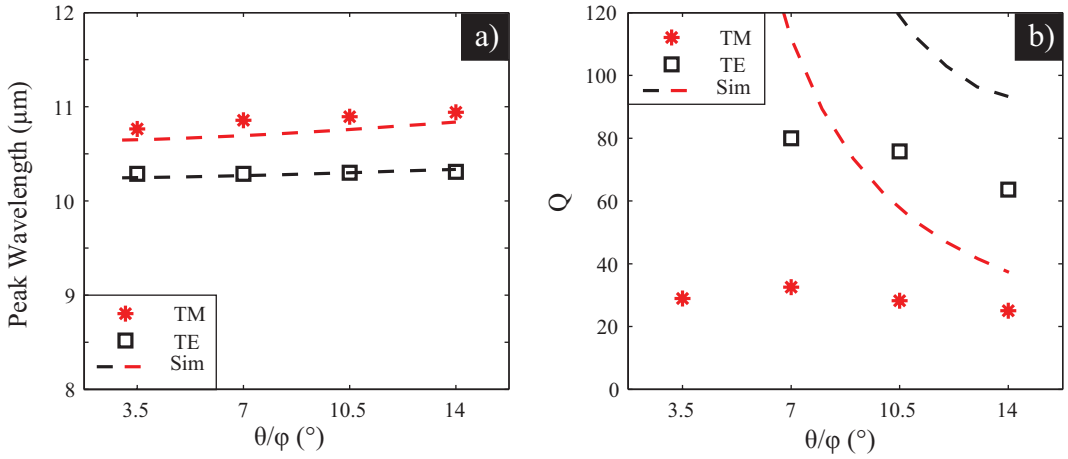


Figure 6.5: a) Peak wavelength and b) quality factor dependence on incident angle for transmission bands associated with $TM_1^-$ and $TE_2^-$ modes. The corresponding simulated parameters are also included for the as-characterized parameters: $\theta = 7°$ and $\varphi = 14°$ and structure dimensions: $\Lambda = 4.9$ $\mu$m, $t = 2.85$ $\mu$m, $h = 4.05$ $\mu$m and $FF = 0.72$.

response is larger than that of the $TE_2^-$ response, which likely has a consequence on the demonstrated quality factors associated with each resonance.

## 6.2 Quality Factor Analysis

The resonance quality factors are shown in Figure 6.5b as a function of incident angle, including both simulated and experimental results. At small angles the simulated quality factors diverge towards infinity as the overlap integrals between the incident plane wave and supported modes go to to zero. At larger angles there is qualitative agreement between the simulated and experimental responses, where both indicate decreasing quality factors as $\theta, \varphi$ increases. As the angle increases, the overlap between the incident field and guided mode increases, which results in stronger coupling and consequently a broader resonance.

The maximum demonstrated quality factors for the two dominant transmission bands centered in the opaque background, associated with coupling to $TM_1^-$ and $TE_2^-$ modes, were $Q_{exp}(\theta = 7°) = 33$, and $Q_{exp}(\varphi = 14°) = 64$, respectively. These are

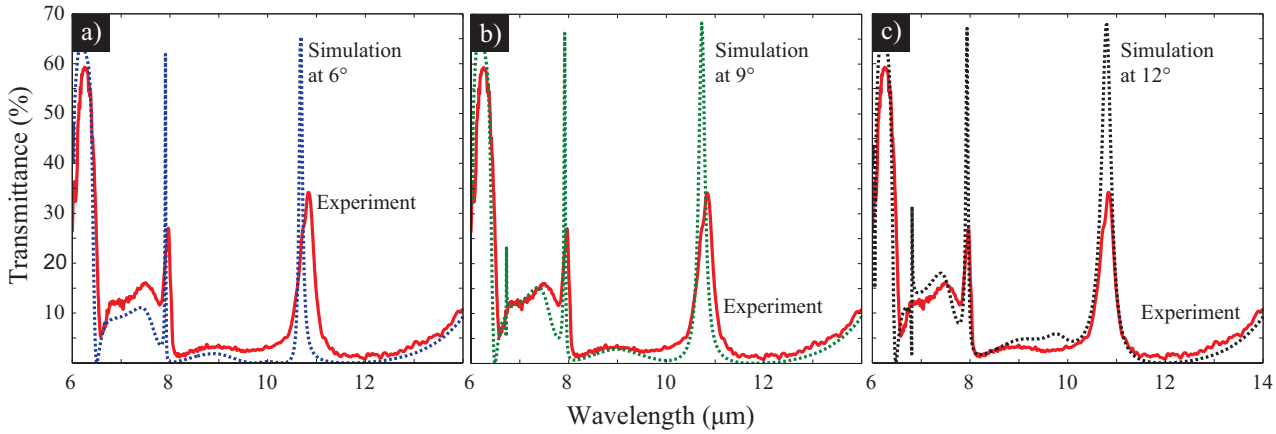


Figure 6.6: Effects of angular extent ($\theta \pm 3°$) allowed by iris. The experimental demonstration at $\theta = 9°$ is shown with the corresponding simulated response at a) $\theta = 6°$, b) $\theta = 9°$, and c) $\theta = 12°$ for a grating with dimensions: $\Lambda = 4.9$ $\mu$m, $t = 2.85$ $\mu$m, $h = 4.05$ $\mu$m and $FF = 0.72$.

smaller than their expected quality factors due to resonance broadening, $Q_r(\theta = 7°) = 113$, and $Q_r(\varphi = 14°) = 107$, for the TM and TE associated bands, respectively. The reduction in the quality factor can be attributed to the angular extent allowed by the aperture, nonradiative losses that can dominate the response at lower angles, and the finite grating size.

The $\pm 3°$ angular uncertainty allowed by the iris setup, discussed in Chapter II, is expected to significantly affect the resonant response. A range of angles probes different $k_x$ or $k_z$ values, which due to the slope of the transmission bands of Figure 5.4 is expected to result in a broader observed peak. This angular dependence is evident in the experimental data, where the transmission peak corresponding to the $TE_2^-$ mode is narrower and more symmetrical than the peak corresponding to the $TM_1^-$ mode. Figure 6.6 shows the experimental transmission bands for $\theta = 9°$ with simulated response at $\theta = 6°$, 9°, and 12°. The simulated response shows both a shift in resonant wavelength, as discussed, and broadening of the bandwidth, which both contribute to the broadening in the experimental demonstration. The highest possible measured quality factors allowed by the iris angular extent are $Q_i(\theta = 7 \pm 3°) \approx 110$, and $Q_i(\varphi = 14 \pm 3°) \approx 175$, for TM and TE modes respectively. These were calculated

using

$$Q_{max} = \frac{\omega_{\theta,\varphi}}{\omega_{\theta,\varphi+3^\circ} - \omega_{\theta,\varphi-3^\circ}} \ , \tag{6.1}$$

which provides an upper limit to the expected $Q_{max}$ since the bandwidth at each angle is not taken into account. Although the experimental values are well below these limits, the effect is likely contributing to the broadening in each of the resonances. Further constraining the incident light is expected to increase the experimental quality factor.

Even with better angular control of the incident light, material absorption and inhomogeneous broadening due to disorder scattering are still expected to put an upper bound on the achievable quality factor as $\theta, \varphi \to 0^\circ$. Using optical properties from literature for silicon in this frequency range,[87] the maximum quality factor due to nonradiative losses is on the order $Q_{nr} \sim 10^4$. This estimate serves as an upper bound, and does not include additional absorption losses due to dopants or impurities introduced during the fabrication process, nor does it include scattering losses due to manufacturing imperfections. Using the relation

$$1/Q_{tot} = 1/Q_r + 1/Q_{nr} \tag{6.2}$$

we estimate the nonradiative quality factor in our samples to be $Q_{nr} \sim 100$. Optimizing the fabrication further to reduce surface roughness and improve sidewall profiles may increase the transmittance and quality factor.

It is also known that the grating size affects the attainable quality factor and peak transmittance on resonance.[95,96] Since our grating was limited to approximately 100 periods, this could further limit our peak transmittance and quality factor.

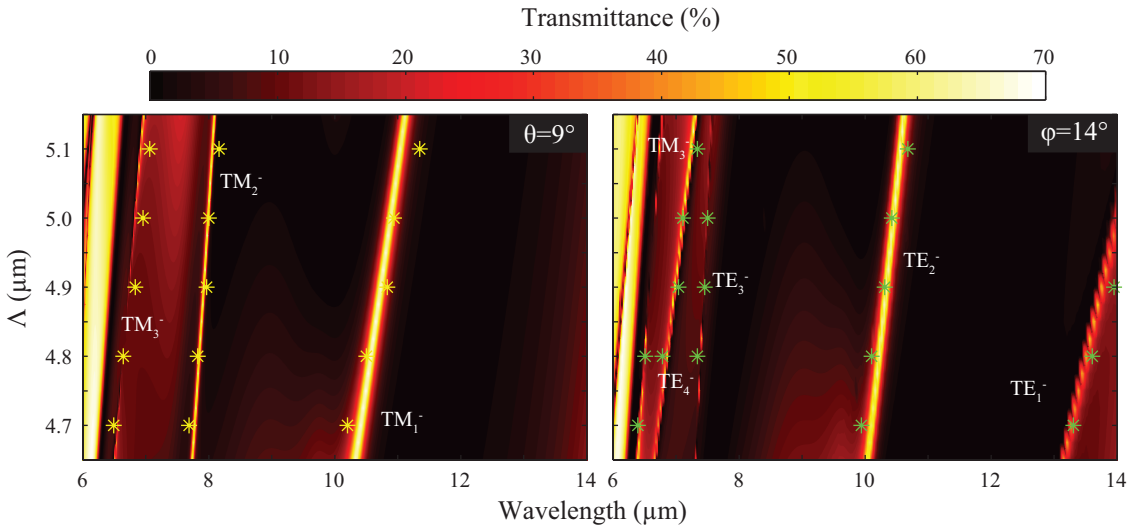


Figure 6.7: Simulated contour plots with experimental peak wavelength locations overlaid (*) for suspended silicon gratings with $FF = 72\%$, $t = 2.85$ $\mu$m and $h = 4.05$ $\mu$m and 4.7 $\mu$m$\leq \Lambda \leq 5.1$ $\mu$m with (left) $\theta = 7^{\circ}$ and (right) $\varphi = 14^{\circ}$.

## 6.3 Wavelength Selection

The filtered wavelength can be selected by simply varying the grating period or fill factor while keeping the other dimensions constant, which is attractive for use in applications such as hyperspectral imaging. To illustrate the ease with which the filtered wavelength can be chosen, we characterized a series of gratings with periods between 4.7 $\mu$m and 5.1 $\mu$m while holding the grating thickness and fill factor constant. The experimental peak wavelengths are overlaid (*) on the simulated response in Figure 6.7, for the experimental conditions $\theta = 9^{\circ}$ and $\varphi = 14^{\circ}$. The transmission bands are labeled with the guided modes responsible for the response. The experimental and simulated filtering peaks agree well with both similar slopes and peak locations. For the two dominant filtering bands there is an apparent difference between the slopes as the period is changed. This difference is illustrated in Figure 6.8 with the peak wavelengths for each resonance plotted. The TE associated band has a smaller slope than that associated with the TM mode, which provides finer wavelength selection capabilities. In contrast, the operating range of the TM mode

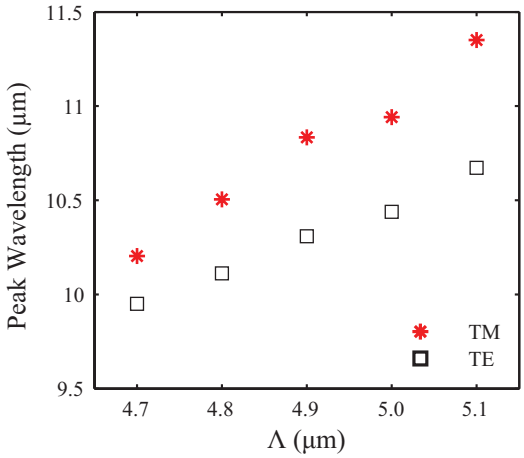


Figure 6.8: Comparison of wavelength selection between $TM_1^-$ and $TE_2^-$ associated transmission bands as a function of grating period. The grating dimensions were $FF = 72\%$, $t = 2.85$ $\mu$m and $h = 4.05$ $\mu$m and 4.7 $\mu$m$\leq \Lambda \leq 5.1$ $\mu$m with data collected at $\theta = 9°$ and $\varphi = 14°$ for the TM and TE datasets, respectively.

associated band is larger than that of the TE associated mode. Depending on the application, either finer tuning or a larger operation bandwidth may be desired, and separately chosen. The raw data associated with Figure 6.7 are included at the end of this chapter.

## 6.4 Material Absorption

To better understand the disparity between the expected peak transmittance and experimental transmittance on resonance, simulations were performed accounting for the silicon substrate and possible increases in silicon's extinction coefficient compared to those used from literature.[87] The simulations included 500 $\mu$m of silicon but did not include the exit interface, which results in interference fringes that are not observed experimentally. Figure 6.9 shows the effects of absorption on the peak transmittance of the transmission band associated with the $TM_1^-$ resonance, accounting for the grating alone as well as accounting for the grating with the 500 $\mu$m thick substrate. The transmittance is plotted as a function of the extinction coefficient multiplier, which changes the literature values by that factor.

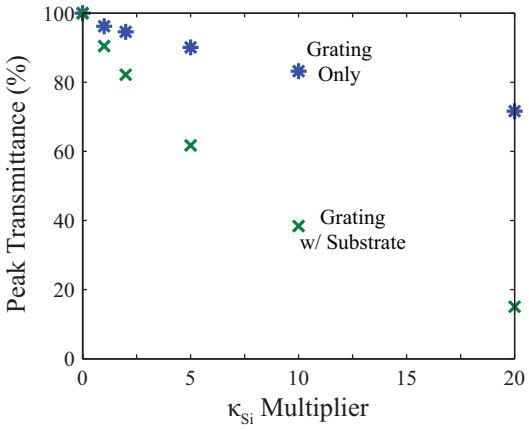


Figure 6.9: Simulated peak transmittance dependence on extinction coefficients for the grating and the grating with underlying substrate. The simulations were performed on a grating with: $\Lambda = 4.9$ $\mu$m, $t = 2.85$ $\mu$m, $h = 4.05$ $\mu$m and $FF = 0.72$ and an angle of $\theta = 7°$.

With moderate increases in the extinction coefficient, the peak transmittance is significantly reduced by absorption in the substrate. Unfortunately ellipsometry measurements to extract the material characteristics of the SOI wafer could not be performed, making it challenging to draw definite conclusions on the deviation between the literature and experimentally used materials. However, the absorption due to impurities is expected to have a significant effect on the extinction coefficient,[97] which may account for the relatively low (40%) transmittance demonstrated.

The loss is much less significant if the grating alone is used to achieve the filtering capabilities, regardless of the extinction coefficient. Thus, removing the substrate is expected to significantly improve the transmittance on resonance.

## 6.5 Further Discussion

This is the first demonstration of a narrowband transmission filter using a single layer dielectric structure. While the demonstration was performed in the LWIR, the dimensions of the grating can be scaled to enable filtering capabilities in any spectrum, assuming similarly lossless materials can be obtained. Consequently, their use may

have many additional applications not mentioned in the introduction.

Commercial LWIR hyperspectral cameras have spectral resolution as high as 100 nm, while others have 400 nm or lower resolution.[12] The demonstrated dielectric grating resolution is comparable to these commercial products, which may suggest their utility beyond the research lab. For staring applications where precise angular control is possible, such as surveillance and remote sensing, the undesirable angular dependence of the filtered wavelength can be mitigated. The resolution is also expected to increase for this type of application, where the incident light is plane-wave-like, in contrast to the focusing demonstrated above. Furthermore, the polarization dependence can be addressed by integrating a polarizer into the imaging system. While filter integration into imaging systems has yet to be performed, there is potential for them to augment current LWIR hyperspectral imaging capabilities.

Additionally, it is worthwhile to compare our design to a previously proposed transmission filter strategy using weakly periodic gratings at normal incidence that is also based on the interference between a strongly-coupled and weakly-coupled guided mode.[75,76] In that proposal, the requisite difference in coupling strength is achieved by overlapping modes corresponding to different diffraction orders, leveraging the observation that light diffracts more strongly into lower orders than higher orders. In contrast, we have shown unique optical selection rules of a single diffraction order arising in a high-contrast grating near normal incidence make the use of multiple diffraction orders unnecessary for achieving narrowband filtering abilities and result in a wider operating range.

## 6.6 Summary

In this chapter we have experimentally demonstrated and characterized transmission filters using a single layer dielectric grating. We leveraged the group theoretical analysis presented in Chapter V to predict the transmission filtering capabilities when

off-normal incidence in the $xy$- and $xz$-planes is introduced. The experimental transmittance bands associated with both TM and TE modes possess strong discrimination from the background. Wavelength selection was demonstrated by changing the grating period and the filters angular dependence agrees well with simulated response. While the spectral resolution is currently limited by experimental constraints, it is still comparable to commercial hyperspectral imaging systems, which make them attractive candidates for integration into imaging systems.

## 6.7 Filter Appendix

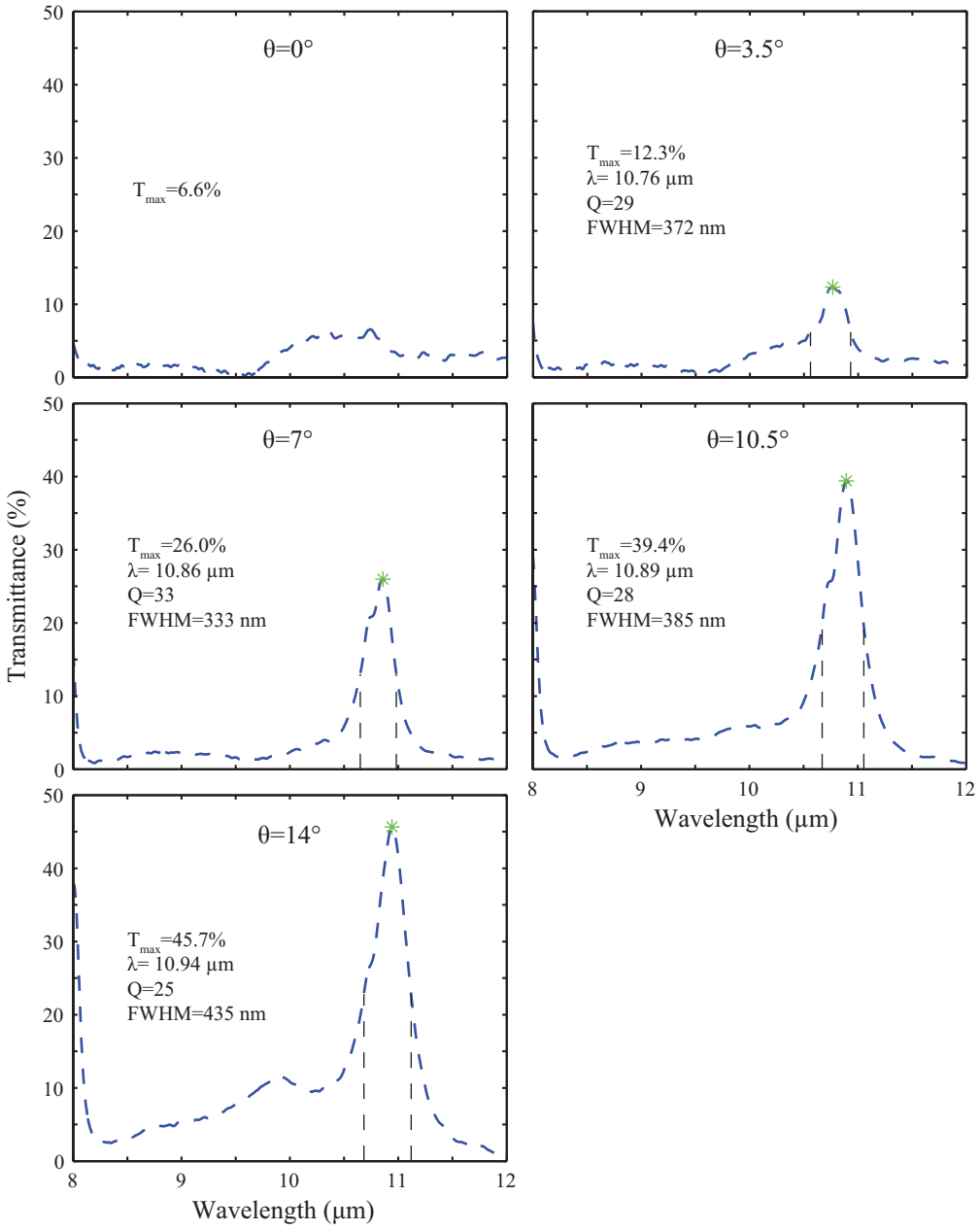


Figure 6.10: Line plots for TM modes increasing the incident angle $\theta$ with extracted peak transmittance, peak wavelength, resonance quality factor, and resonance FWHM.

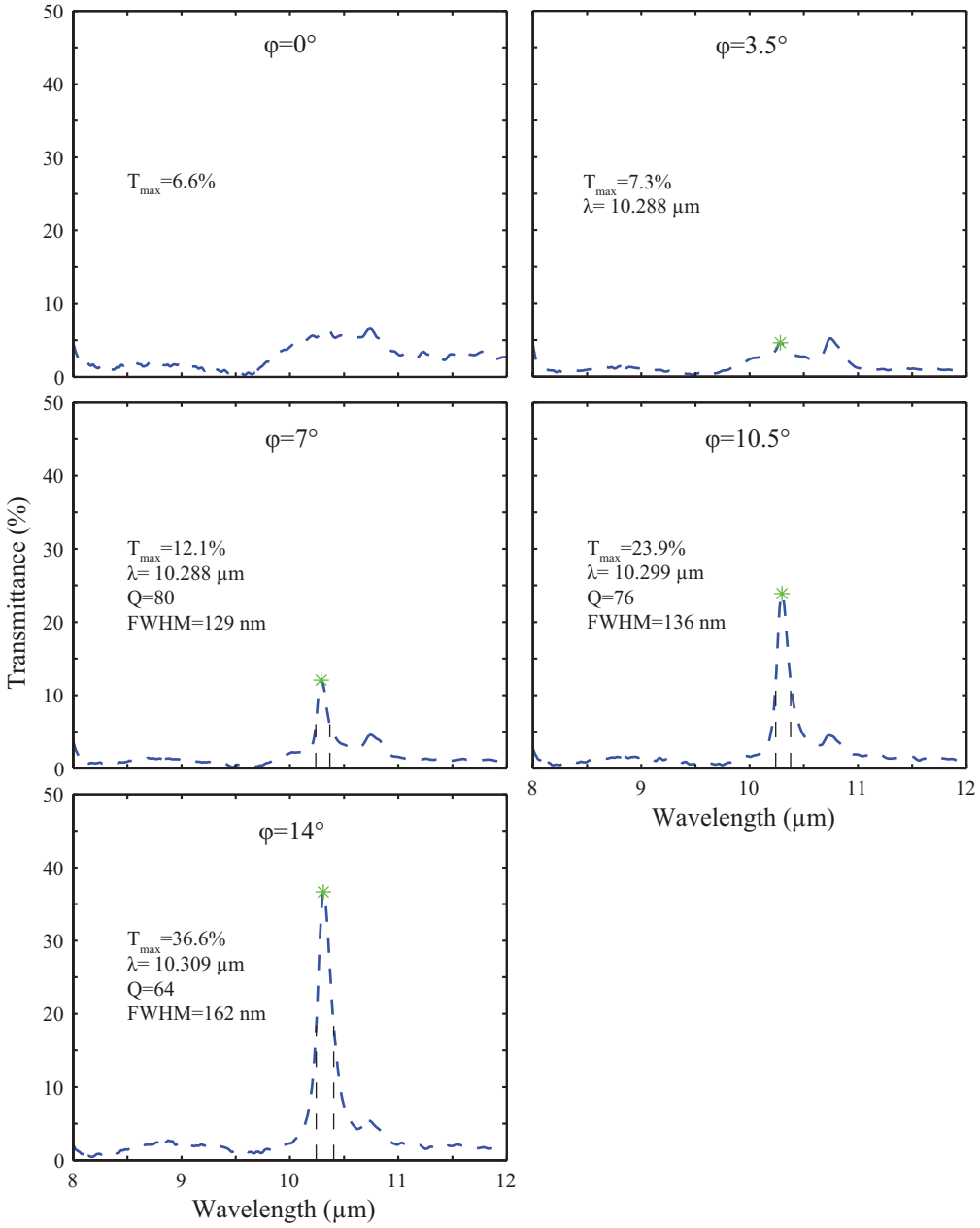


Figure 6.11: Line plots for TE modes increasing the incident angle $\varphi$ with extracted peak transmittance, peak wavelength, resonance quality factor, and resonance FWHM.

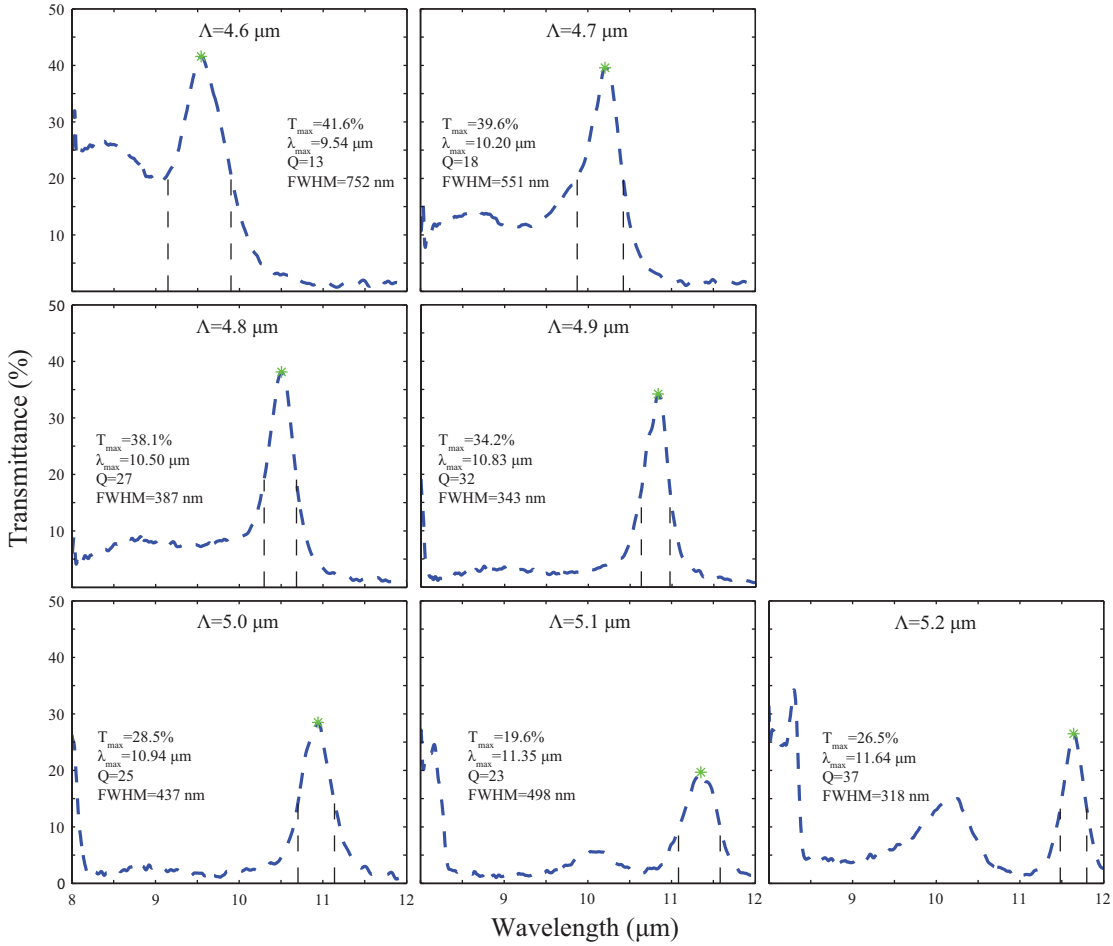


Figure 6.12: Line plots for TM modes at $\theta = 9°$ for gratings with different periods with extracted peak transmittance, peak wavelength, resonance quality factor, and resonance FWHM.

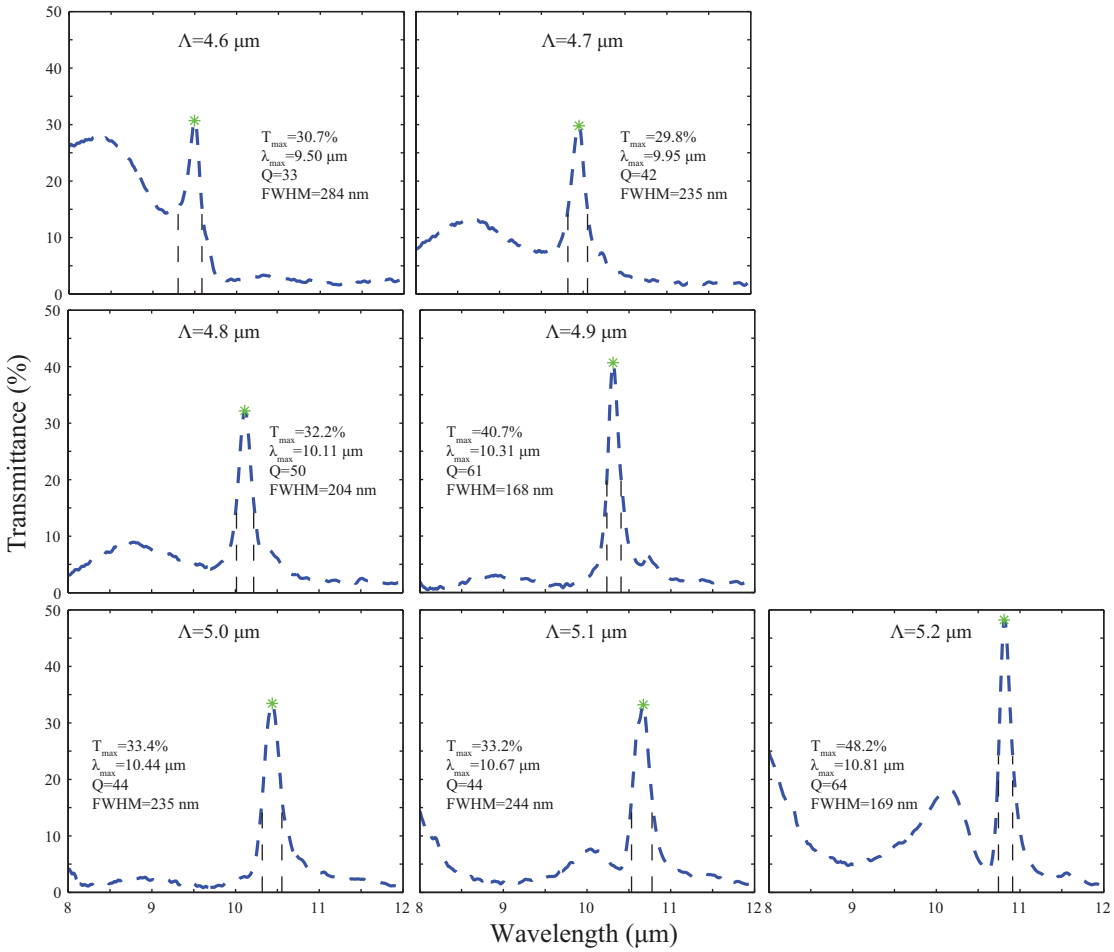


Figure 6.13: Line plots for TE modes at $\varphi = 14°$ for gratings with different periods with extracted peak transmittance, peak wavelength, resonance quality factor, and resonance FWHM.

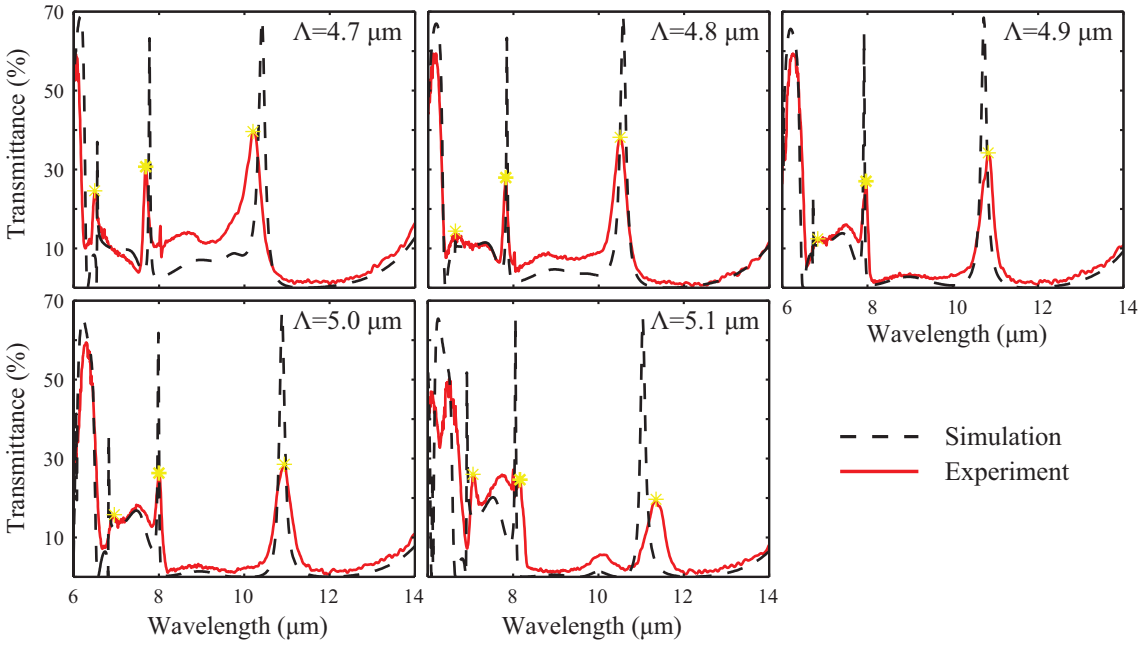


Figure 6.14: Experimental and simulated responses at $\theta = 9°$ with peak experimental wavelength indicated.

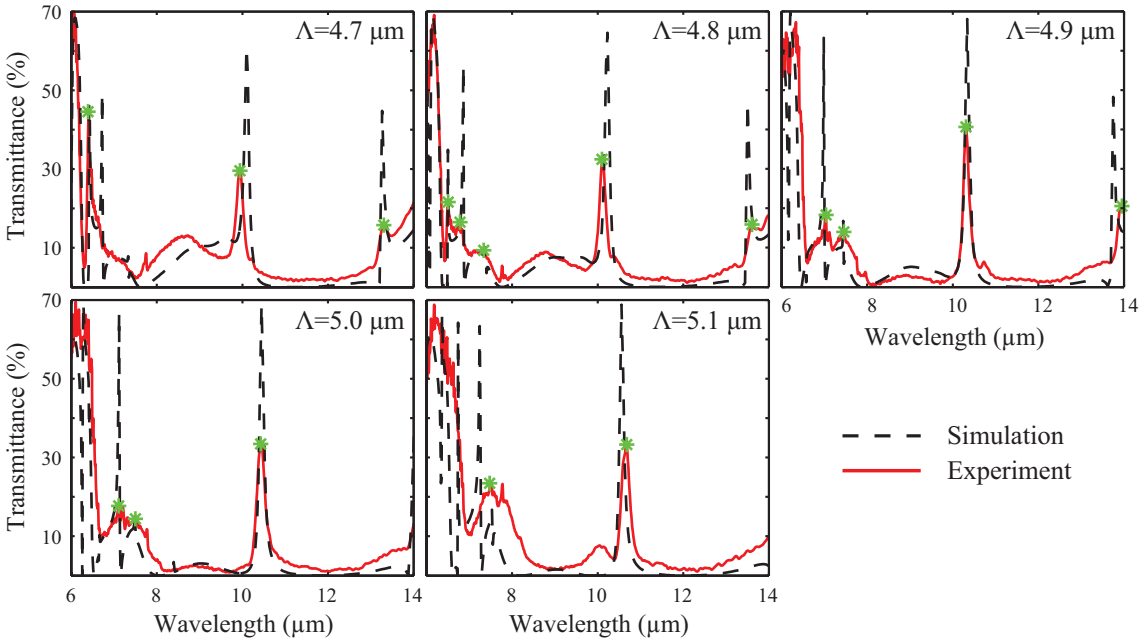


Figure 6.15: Experimental and simulated responses at $\varphi = 14°$ with peak experimental wavelength indicated.

# CHAPTER VII

# Future Work and Conclusions

## 7.1 Future Studies

Several studies can build on this work to better understand system operation and integration, making it more attractive for commercial applications. In particular future studies may include: improving characterization capabilities, developing normal incidence narrowband transmission filters, either through Fabry-Pérot etalons or using a grating alone, developing polarization insensitive elements, and integrating the gratings into imaging systems.

### 7.1.1 Improved Characterization Capabilities

The characterization techniques used in the presented studies included transmittance and reflectance measurements using a benchtop FTIR system. The constraints of the system include their use of high numerical aperture lenses, which limit attainable quality factors, as well as a limited ability to measure reflectance capabilities for various structures.

Using a coherent light source, such as a tunable laser, to characterize the gratings would lead to higher quality factors and responses that would agree better with simulations. More accurate angular characterization could be performed, and the losses due to fabrication tolerances and absorption could be more readily analyzed.

Although the operating bandwidth of tunable lasers is generally reduced compared to FTIR spectrometers, the precise angular definition would enable significantly improved characterization capabilities that would help us better understand the limitations of resonant responses.

### 7.1.2 Normal Incidence Filters

In the presented research, to realize transmission filtering capabilities from the dielectric grating, the symmetry of the incident light was broken. This enabled plane waves to couple to modes that were symmetry protected at normal incidence. If instead, the symmetry of the grating is broken, normal incidence transmission filtering capabilities may be realized. Figure 7.1 shows several prospective structures that break the $x$-symmetry of the grating and their respective responses, in analogy to introducing $\theta$ to the incident light. Each grating uses a different profile to break the symmetry, but all require only a small change from their rectangular shape.

Figure 7.1a shows a blazed type grating that may be realized using gray-scale lithography techniques.[98] This structure is characterized by a vertical cut on the top surface of the grating, where transmittance filtering response can be realized with as little as 200 nm of cut, or $< 10\%$ of the total height of the grating.

The other two subfigures, Figure 7.1b and Figure 7.1c possess triangular cuts on the vertical sidewalls of the grating. Fabrication of these structures may entail tilting the sample during the reactive ion etch to achieve non-vertical sidewalls. To achieve similar filtering capabilities from these structures larger cuts are required. However, they are still $10 - 15\%$ of the total width of the structure. More thorough analysis and experimental demonstration are attractive next studies that have potential for achieving high quality factor transmission filtering response at normal incidence.

While the above structures enable static wavelength selection for potential imaging applications, integrating the demonstrated broadband reflectors into Fabry-Pérot

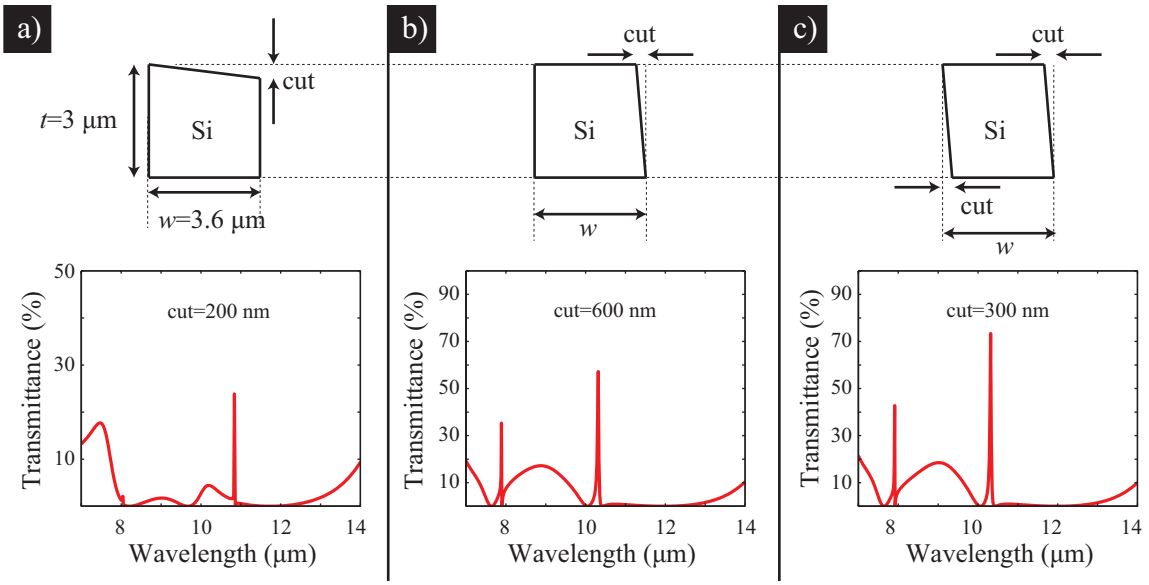


Figure 7.1: Possible cross-sections that break the $x$-symmetry of the grating to enable normal incidence filtering and accompanying simulated transmittance. The simulated grating dimensions were $\Lambda = 5$ $\mu$m, $t = 3$ $\mu$m, $h = 4.0$ $\mu$m and $FF = 0.72$.

etalons would enable tunable filtering capabilities. By integrating micro-electromechanical actuation, the distance between the two mirrors can be varied, changing the filtered wavelength. In similar micro-cavities, continuous wavelength selection between 8 and 11 $\mu$m has been realized.[28] This type of filter would enable broader tuning ranges and more control over the filtered wavelength, which would be attractive for spectrometer-on-a-chip applications.

### 7.1.3 Polarization Independent Broadband Reflectors

The polarization dependence exhibited by the grating elements may be leveraged in some instances, while other applications may require polarization independent capabilities. Two-dimensional gratings have been demonstrated to afford broadband reflectance responses that are independent of the incident polarization.[19,99] A schematic of an InP two-dimensional grating reflector operating at the telecommunications wavelength is shown in Figure 7.2, which is reproduced from a previous study.[19]

While these two-dimensional gratings can be polarization independent, their oper-

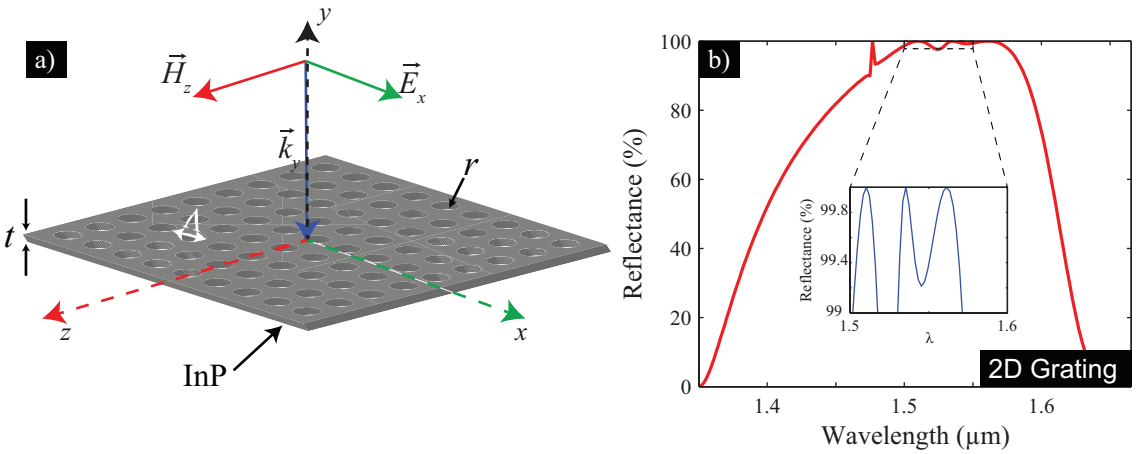


Figure 7.2: a) A schematic of a prospective two-dimensional grating reflector and b) corresponding preliminary reflectance for an InP two-dimensional grating with dimensions $\Lambda = 1.2$ $\mu$m, $t = 420$ nm, and $r = 400$ nm.[19]

ating bandwidth is reduced compared to one-dimensional gratings. This is a tradeoff that may make one system more attractive than another for specific applications. Designing and fabricating polarization independent gratings would provide different capabilities that may be useful in various applications.

### 7.1.4 System Integration

Lastly, while the demonstration of transmission filters is very important, system integration is equally important. Figure 7.3 shows a schematic of a possible configuration for integrating the filters into an imaging system. It includes an array of gratings positioned above detector pixels.

For system integration, important considerations include the incident light configurations, such as polarization and incident angle, as well as signal strength and discrimination in spectral regions outside the broad reflectance spectrum. The incident angle for staring applications, including remote sensing and aerial surveillance, can be chosen very precisely. Unfortunately, stray light from areas not being imaged may affect such a system's response. Constraining the incident light will be paramount to understanding the potential of these systems. Collimating the light

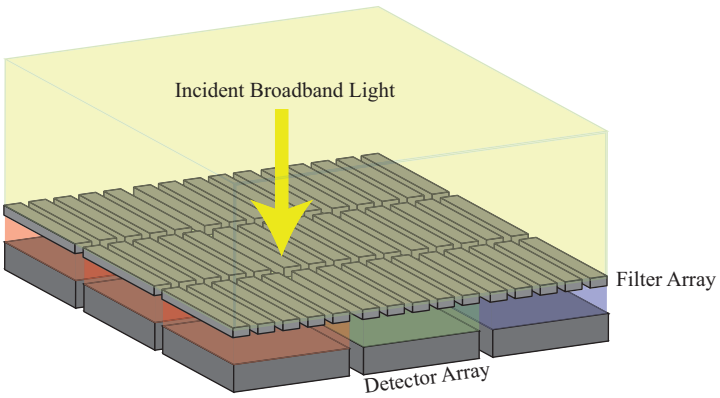


Figure 7.3: A schematic of possible filter integration in a focal plane array.

prior to spectral filtering is one method that may be used to precisely define the incident angle, which will require significant engineering considerations.

## 7.2 Conclusion

In this dissertation several studies have been presented on dielectric grating-based optical elements that operate in the LWIR spectral region. We began with the intent of integrating broadband, lossless reflectors into a Fabry-Pérot etalon to enable filtering capabilities for LWIR imaging applications. Accordingly, we demonstrated a broadband reflector based on a $Si/SiO_2$ grating system that unfortunately, was limited by phonon absorption in the $SiO_2$ layer. Subsequently we pursued a suspended silicon grating that improved the index contrast and removed the lossy $SiO_2$ layer. We demonstrated both normal incidence and oblique incidence broadband reflectors with reflectance greater than 90% and 85%, respectively, across the LWIR spectrum.

Subsequently, a group theoretical analysis was used to explain selection rules for coupling an incident plane wave to the gratings' supported modes. At normal incidence several modes were shown to be accessible, while others possessed symmetry mismatch with the incident plane wave. Moving off normal incidence broke this symmetry, permitting weak coupling to the previously symmetry-protected modes. We used this analysis to predict transmission filtering capabilities of a dielectric grat-

ing. By leveraging the normally incident broadband reflector to provide the opaque background, we predicted transmission filtering characteristics by moving off normal incidence in two different incident planes. Independent mode sets, TM and TE resulted in separate transmission bands, as a consequence of the chosen incident plane.

Experimental demonstration of the predicted filtering capabilities followed, which was shown to agree well with the simulated transmittance as well as the grating modal analysis. The filters' angular dependence was characterized, which demonstrated shifts in the resonant frequency and line width broadening as expected from theory. The filters demonstrated quality factors as high as $Q = 64$, which were limited by the characterization method that allowed a range of incident angles. Wavelength selection was demonstrated by changing the period of the grating. The ease of wavelength selection make them attractive for commercial applications, where the demonstrated quality factors are comparable to commercial hyperspectral imaging systems. While the experimental demonstration was performed in the LWIR spectral region, the operating principle is scale independent, making application in other wavelength ranges, including the visible spectrum, possible.

Lastly, this work provides a foundation for several subsequent studies including a filter operating at normal incidence, which breaks the symmetry of the grating structure instead of the incident light. Integration of the demonstrated optical elements into Fabry-Pérot etalons and imaging systems will further elucidate their potential for commercial viability.

# BIBLIOGRAPHY

# BIBLIOGRAPHY


[1] M. Lipson, "Guiding, modulating, and emitting light on silicon-challenges and opportunities," *Journal of Lightwave Technology*, vol. 23, no. 12, pp. 4222–4238, Dec 2005.

[2] S. Choi, M. Goryll, L. Sin, P. Wong, and J. Chae, "Microfluidic-based biosensors toward point-of-care detection of nucleic acids and proteins," *Microfluidics and Nanofluidics*, vol. 10, no. 2, pp. 231–247, 2011.

[3] L. Gervais, N. de Rooij, and E. Delamarche, "Microfluidic chips for point-of-care immunodiagnostics," *Advanced Materials*, vol. 23, no. 24, pp. H151–H176, 2011.

[4] X. Hou and B. T. Jones, "Field instrumentation in atomic spectroscopy," *Microchemical Journal*, vol. 66, no. 13, pp. 115 – 145, 2000.

[5] P. T. Lin, S. W. Kwok, H.-Y. G. Lin, V. Singh, L. C. Kimerling, G. M. Whitesides, and A. Agarwal, "Mid-infrared spectrometer using opto-nanofluidic slot-waveguide for label-free on-chip chemical sensing," *Nano Letters*, vol. 14, no. 1, pp. 231–238, 2014.

[6] A. Keating, K. Silva, J. Dell, C. Musca, and L. Faraone, "Optical characterization of Fabry-Pérot MEMS filters integrated on tunable short-wave IR detectors," *IEEE Photonics Technology Letters*, vol. 18, no. 9, pp. 1079–1081, May 2006.

[7] N. Quack, S. Blunier, J. Dual, F. Felder, M. Arnold, and H. Zogg, "Mid-infrared tunable resonant cavity enhanced detectors," *Sensors*, vol. 8, no. 9, pp. 5466–5478, 2008.

[8] A. T. Pritt, P. N. Kupferman, S. J. Young, and R. A. Keller, "Imaging LWIR spectrometers for remote sensing applications," in *Conference on Infrared Imaging Systems - Design, Analysis, Modeling, and Testing VIII*, vol. 3063, 1997, Conference Proceedings, pp. 138–149.

[9] M. T. Eismann, *Hyperspectral Remote Sensing*. Bellingham, Washington: SPIE Press, 2012.

[10] Y. Z. Feng and D. W. Sun, "Application of hyperspectral imaging in food safety inspection and control: a review," *Critical Reviews in Food Science and Nutrition*, vol. 52, no. 11, pp. 1039–1058, 2012.

[11] C. M. Gittins, W. J. Marinelli, and J. O. Jensen, "Remote sensing and selective detection of chemical vapor plumes by LWIR imaging Fabry-Pérot spectrometry," pp. 63–71, 2002.

[12] H. Holma, A.-J. Mattila, T. Hyvrinen, and O. Weatherbee, "Advances in hyperspectral LWIR pushbroom imagers," pp. 80 320X–80 320X–14, 2011.

[13] M. Vollmer and K. Mollmann, *Infrared Thermal Imaging: Fundamentals, Research and Applications*. Wiley, 2011.

[14] M. Z. Tidrow and W. R. Dyer, "Infrared sensors for ballistic missile defense," *Infrared Physics & Technology*, vol. 42, no. 3-5, pp. 333–336, 2001.

[15] M. Munzberg, R. Breiter, W. Cabanski, H. Lutz, J. Wendler, J. Ziegler, R. Rehm, and M. Walther, "Multi spectral IR detection modules and applications," in *32nd Conference on Infrared Technology and Applications*, vol. 6206. SPIE-International Society of Optical Engineering, Conference Proceedings, pp. 20 627–20 627.

[16] S. Khare and S. S. Negi, "Thermal (Infrared) imaging sensors," *Defence Science Journal*, vol. 57, no. 3, pp. 173–183, 2007.

[17] W. J. Marinelli, C. M. Gittins, A. H. Gelb, and B. D. Green, "Tunable Fabry-Pérot etalon-based long-wavelength infrared imaging spectroradiometer," *Applied Optics*, vol. 38, no. 12, pp. 2594–2604, Apr 1999.

[18] C. Mateus, M. Huang, Y. Deng, A. Neureuther, and C. Chang-Hasnain, "Ultrabroadband mirror using low-index cladded subwavelength grating," *IEEE Photonics Technology Letters*, vol. 16, no. 2, pp. 518–520, 2004.

[19] S. Boutami, B. Ben Bakir, H. T. Hattori, X. Letartre, J. L. Leclercq, P. Rojo-Romeo, M. Garrigues, C. Seassal, and P. Viktorovitch, "Broadband and compact 2-D photonic crystal reflectors with controllable polarization dependence," *IEEE Photonics Technology Letters*, vol. 18, no. 5-8, pp. 835–837, 2006.

[20] R. Magnusson and S. S. Wang, "New principle for optical filters," *Applied Physics Letters*, vol. 61, no. 9, pp. 1022–1024, 1992.

[21] S. Boutami, B. Benbakir, X. Letartre, J. L. Leclercq, P. Regreny, and P. Viktorovitch, "Ultimate vertical Fabry-Pérot cavity based on single-layer photonic crystal mirrors," *Optics Express*, vol. 15, no. 19, pp. 12 443–12 449, 2007.

[22] Y. Ding and R. Magnusson, "Use of nondegenerate resonant leaky modes to fashion diverse optical spectra," *Optics Express*, vol. 12, no. 9, pp. 1885–1891, 2004.

[23] M. C. Y. Huang, Y. Zhou, and C. J. Chang-Hasnain, "Nano electro-mechanical optoelectronic tunable VCSEL," *Optics Express*, vol. 15, no. 3, pp. 1222–1227, 2007.

[24] C. F. R. Mateus, M. C. Y. Huang, and C. J. Chang-Hasnain, "Micromechanical tunable optical filters: general design rules for wavelengths from near-IR up to 10 $\mu$m," *Sensors and Actuators A-Physical*, vol. 119, no. 1, pp. 57–62, 2005.

[25] Y. Wang, B. J. Potter, and J. J. Talghader, "Coupled absorption filters for thermal detectors," *Optics Letters*, vol. 31, no. 13, pp. 1945–1947, Jul 2006.

[26] J. Jackson, *Classical Electrodynamics*. Wiley, 1998.

[27] M. Born and E. Wolf, *Principles of Optics: Electromagnetic Theory of Propagation, Interference and Diffraction of Light*. Cambridge University Press, 1997.

[28] M. Ebermann, N. Neumann, K. Hiller, E. Gittler, M. Meinig, and S. Kurth, "Widely tunable Fabry-Pérot filter based MWIR and LWIR microspectrometers," pp. 83 740X–83 740X–9, 2012.

[29] U. Kemiktarak, M. Metcalfe, M. Durand, and J. Lawall, "Mechanically compliant grating reflectors for optomechanics," *Applied Physics Letters*, vol. 100, no. 6, p. 3, 2012.

[30] M. C. Y. Huang, Y. Zhou, and C. J. Chang-Hasnain, "A surface-emitting laser incorporating a high-index-contrast subwavelength grating," *Nature Photonics*, vol. 1, no. 2, pp. 119–122, 2007.

[31] L. Rayleigh, "On the reflection of light from a regularly stratified medium," *Proceedings of the Royal Society of London. Series A*, vol. 93, no. 655, pp. 565–577, 1917.

[32] J. D. Joannopoulos, S. G. Johnson, J. N. Winn, and R. D. Meade, *Photonic Crystals: Molding the Flow of Light* , 2nd ed. Princeton University Press, 2008.

[33] C. Mateus, M. Huang, L. Chen, C. Chang-Hasnain, and Y. Suzuki, "Broadband mirror (1.12-1.62 $\mu$m) using a subwavelength grating," *IEEE Photonics Technology Letters*, vol. 16, no. 7, pp. 1676–1678, 2004.

[34] L. Chen, M. C. Y. Huang, C. F. R. Mateus, C. J. Chang-Hasnain, and Y. Suzuki, "Fabrication and design of an integrable subwavelength ultrabroadband dielectric mirror," *Applied Physics Letters*, vol. 88, no. 3, 2006.

[35] J. M. Foley, A. M. Itsuno, T. Das, S. Velicu, and J. D. Phillips, "Broadband long-wavelength infrared $Si/SiO_2$ subwavelength grating reflector," *Optics Letters*, vol. 37, no. 9, pp. 1523–1525, 2012.

[36] L. Pilozzi, D. Schiumarini, N. Tomassini, and A. D'Andrea, "Giant reflection band and anomalous negative transmission in a resonant dielectric grating slab: application to a planar cavity," *Physical Review B*, vol. 86, no. 4, 2012.

[37] C. Xu, L. M. Xu, Y. H. Qiang, Y. B. Zhu, J. T. Liu, and J. Y. Ma, "Excellent polarization-independent reflector based on guided mode resonance effect," *Chinese Physics B*, vol. 20, no. 10, 2011.

[38] J. M. Kontio, J. Simonen, K. Leinonen, M. Kuittinen, and T. Niemi, "Broadband infrared mirror using guided-mode resonance in a subwavelength germanium grating," *Optics Letters*, vol. 35, no. 15, pp. 2564–2566, 2010.

[39] D. Fattal, J. J. Li, Z. Peng, M. Fiorentino, and R. G. Beausoleil, "Flat dielectric grating reflectors with focusing abilities," *Nature Photonics*, vol. 4, no. 7, pp. 466–470, 2010.

[40] F. L. Lu, F. G. Sedgwick, V. Karagodsky, C. Chase, and C. J. Chang-Hasnain, "Planar high-numerical-aperture low-loss focusing reflectors and lenses using subwavelength high contrast gratings," *Optics Express*, vol. 18, no. 12, pp. 12 606–12 614, 2010.

[41] Y. Zhou, M. C. Y. Huang, and C. J. Chang-Hasnain, "Tunable VCSEL with ultra-thin high contrast grating for high-speed tuning," *Optics Express*, vol. 16, no. 18, pp. 14 221–14 226, 2008.

[42] V. Karagodsky and C. J. Chang-Hasnain, "Physics of near-wavelength high contrast gratings," *Optics Express*, vol. 20, no. 10, pp. 10 888–10 895, 2012.

[43] Y. Zhou, M. Moewe, J. Kern, M. C. Y. Huang, and C. J. Chang-Hasnain, "Surface-normal emission of a high-Q resonator using a subwavelength high-contrast grating," *Optics Express*, vol. 16, no. 22, pp. 17 282–17 287, 2008.

[44] Y. Zhou, M. C. Y. Huang, C. Chase, V. Karagodsky, M. Moewe, B. Pesala, F. G. Sedgwick, and C. J. Chang-Hasnain, "High-index-contrast grating (HCG) and its applications in optoelectronic devices," *IEEE Journal of Selected Topics in Quantum Electronics*, vol. 15, no. 5, pp. 1485–1499, 2009.

[45] M. Mutlu, A. E. Akosman, G. Kurt, M. Gokkavas, and E. Ozbay, "Experimental realization of a high-contrast grating based broadband quarter-wave plate," *Optics Express*, vol. 20, no. 25, pp. 27 966–27 973, 2012.

[46] M. Mutlu, A. E. Akosman, and E. Ozbay, "Broadband circular polarizer based on high-contrast gratings," *Optics Letters*, vol. 37, no. 11, pp. 2094–2096, 2012.

[47] V. Karagodsky, B. Pesala, C. Chase, W. Hofmann, F. Koyama, and C. J. Chang-Hasnain, "Monolithically integrated multi-wavelength VCSEL arrays sing high-contrast gratings," *Optics Express*, vol. 18, no. 2, pp. 694–699, 2010.

[48] Y. Zhou, M. C. Y. Huang, and C. J. Chang-Hasnain, "Large fabrication tolerance for VCSELs using high-contrast grating," *IEEE Photonics Technology Letters*, vol. 20, no. 5-8, pp. 434–436, 2008.

[49] C. Chase, Y. Zhou, and C. J. Chang-Hasnain, "Size effect of high contrast gratings in VCSELs," *Optics Express*, vol. 17, no. 26, pp. 24 002–24 007, 2009.

[50] C. Chase, Y. Rao, W. Hofmann, and C. J. Chang-Hasnain, "1550 nm high contrast grating VCSEL," *Optics Express*, vol. 18, no. 15, pp. 15 461–15 466, 2010.

[51] S. L. Chua, Y. D. Chong, A. D. Stone, M. Soljacic, and J. Bravo-Abad, "Low-threshold lasing action in photonic crystal slabs enabled by Fano resonances," *Optics Express*, vol. 19, no. 2, pp. 1539–1562, 2011.

[52] M. C. Y. Huang, Y. Zhou, and C. J. Chang-Hasnain, "A nanoelectromechanical tunable laser," *Nature Photonics*, vol. 2, no. 3, pp. 180–184, 2008.

[53] V. Karagodsky, F. G. Sedgwick, and C. J. Chang-Hasnain, "Theoretical analysis of subwavelength high contrast grating reflectors," *Optics Express*, vol. 18, no. 16, pp. 16 973–16 988, 2010.

[54] K. Sakoda, *Optical Properties of Photonic Crystals*. Bellingham, Washington: Springer, 2005.

[55] E. Yablonovitch, "Inhibited spontaneous emission in solid-state physics and electronics," *Physical Review Letters*, vol. 58, pp. 2059–2062, May 1987.

[56] E. Yablonovitch and T. J. Gmitter, "Photonic band structure: The face-centered-cubic case," *Physical Review Letters*, vol. 63, pp. 1950–1953, Oct 1989.

[57] R. W. Wood, "On a remarkable case of uneven distribution of light in a diffraction grating spectrum," *Philosophical Magazine*, vol. 4, no. 19-24, pp. 396–402, 1902.

[58] Rayleigh, "On the dynamical theory of gratings," *Proceedings of the Royal Society of London Series a-Containing Papers of a Mathematical and Physical Character*, vol. 79, no. 532, pp. 399–416, 1907.

[59] A. Hessel and A. A. Oliner, "A new theory of woods anomalies on optical gratings," *Applied Optics*, vol. 4, no. 10, 1965.

[60] S. T. Peng, T. Tamir, and H. L. Bertoni, "Theory of periodic dielectric waveguides," *IEEE Transactions on Microwave Theory and Techniques*, vol. MT23, no. 1, pp. 123–133, 1975.

[61] S. H. Fan and J. D. Joannopoulos, "Analysis of guided resonances in photonic crystal slabs," *Physical Review B*, vol. 65, no. 23, 2002.

[62] S. H. Fan, W. Suh, and J. D. Joannopoulos, "Temporal coupled-mode theory for the fano resonance in optical resonators," *Journal of the Optical Society of America A-Optics Image Science and Vision*, vol. 20, no. 3, pp. 569–572, 2003.

[63] R. Magnusson and M. Shokooh-Saremi, "Physical basis for wideband resonant reflectors," *Optics Express*, vol. 16, no. 5, pp. 3456–3462, 2008.

[64] P. Pottier, L. N. Shi, and Y. A. Peter, "Evolution of modes of Fabry-Pérot cavity based on photonic crystal guided-mode resonance mirrors," *Journal of the Optical Society of America B-Optical Physics*, vol. 29, no. 10, pp. 2698–2703, 2012.

[65] R. Magnusson and M. Shokooh-Saremi, "Tunable leaky-mode MEMS filters for multispectral imaging applications," in *2008 IEEE Aerospace Conference*. IEEE, 2008, Conference Proceedings, pp. 1509–1515.

[66] G. Vincent, E. Sakat, P. Ghenuche, S. Collin, N. Bardou, S. Rommeluere, J. Primot, J. Deschamps, F. Pardo, J. L. Pelouard, and R. Haidar, "Spectral filtering with subwavelength gratings: overview and latest advances," in *Conference on Quantum Sensing and Nanophotonic Devices IX*, vol. 8268, 2012, Conference Proceedings.

[67] S. Tibuleac and R. Magnusson, "Narrow-linewidth bandpass filters with diffractive thin-film layers," *Optics Letters*, vol. 26, no. 9, pp. 584–586, 2001.

[68] J. S. Ye, N. Matsuyama, Y. Kanamori, and K. Hane, "Silicon suspended resonant grating filters fabricated from a silicon-on-insulator wafer," *IEEE Photonics Technology Letters*, vol. 20, no. 9-12, pp. 851–853, 2008.

[69] Y. Kanamori, M. Shimono, and K. Hane, "Fabrication of transmission color filters using silicon subwavelength gratings on quartz substrates," *IEEE Photonics Technology Letters*, vol. 18, no. 17-20, pp. 2126–2128, 2006.

[70] R. Magnusson, S. S. Wang, T. D. Black, and A. Sohn, "Resonance properties of dielectric wave-guide gratings - theory and experiments at 4-18 GHz," *IEEE Transactions on Antennas and Propagation*, vol. 42, no. 4, pp. 567–569, 1994.

[71] R. Magnusson and S. S. Wang, "Transmission bandpass guided-mode resonance filters," *Applied Optics*, vol. 34, no. 35, pp. 8106–8109, 1995.

[72] S. Tibuleac and R. Magnusson, "Reflection and transmission guided-mode resonance filters," *Journal of the Optical Society of America A-Optics Image Science and Vision*, vol. 14, no. 7, pp. 1617–1626, 1997.

[73] S. Tibuleac, P. P. Young, R. Magnusson, and T. R. Holzheimer, "Experimental verification of waveguide-mode resonant transmission filters," *IEEE Microwave and Guided Wave Letters*, vol. 9, no. 1, pp. 19–21, 1999.

[74] R. Magnusson, M. Shokooh-Saremi, Y. Hu, K. J. Lee, S. J. W. Platzer, A. K. Nebioglu, S. Zimmerman, and D. Wawro, "Fabrication of guided-mode resonance elements by nanoimprint lithography," *Journal of Nanoscience and Nanotechnology*, vol. 10, no. 3, pp. 1606–1615, 2010.

[75] Y. Ding and R. Magnusson, "Doubly resonant single-layer bandpass optical filters," *Optics Letters*, vol. 29, no. 10, pp. 1135–1137, 2004.

[76] M. Shyiq Amin, J. Woong Yoon, and R. Magnusson, "Optical transmission filters with coexisting guided-mode resonance and Rayleigh anomaly," *Applied Physics Letters*, vol. 103, no. 13, 2013.

[77] J. M. Foley, S. M. Young, and J. D. Phillips, "Narrowband mid-infrared transmission filtering of a single layer dielectric grating," *Applied Physics Letters*, vol. 103, no. 7, p. 5, 2013.

[78] T. W. Ebbesen, H. J. Lezec, H. F. Ghaemi, T. Thio, and P. A. Wolff, "Extraordinary optical transmission through sub-wavelength hole arrays," *Nature*, vol. 391, no. 6668, pp. 667–669, 1998.

[79] F. J. Garcia-Vidal, L. Martin-Moreno, T. W. Ebbesen, and L. Kuipers, "Light passing through subwavelength apertures," *Reviews of Modern Physics*, vol. 82, no. 1, pp. 729–787, 2010.

[80] A. K. Azad, J. F. O'Hara, R. Singh, H. T. Chen, and A. J. Taylor, "A review of terahertz plasmonics in subwavelength holes on conducting films," *IEEE Journal of Selected Topics in Quantum Electronics*, vol. 19, no. 1, 2013.

[81] J. V. Coe, J. M. Heer, S. Teeters-Kennedy, H. Tian, and K. R. Rodriguez, "Extraordinary transmission of metal films with arrays of subwavelength holes," *Annual Review of Physical Chemistry*, vol. 59, pp. 179–202, 2008.

[82] H. A. Bethe, "Theory of diffraction by small holes," *Physical Review*, vol. 66, no. 7/8, pp. 163–182, 1944.

[83] J. Zhou and L. J. Guo, "Transition from a spectrum filter to a polarizer in a metallic nano-slit array," *Scientific Reports*, vol. 4, 2014.

[84] F. Pardo, P. Bouchon, R. Haïdar, and J.-L. Pelouard, "Light funneling mechanism explained by magnetoelectric interference," *Phys. Rev. Lett.*, vol. 107, p. 093902, Aug 2011.

[85] R. Ortuno, C. Garcia-Meca, F. J. Rodriguez-Fortuno, A. Hakansson, A. Griol, J. Hurtado, J. A. Ayucar, L. Bellieres, P. J. Rodriguez, F. Lopez-Royo, J. Marti, and A. Martinez, "Midinfrared filters based on extraordinary optical transmission through subwavelength structured gold films," *Journal of Applied Physics*, vol. 106, no. 12, p. 6, 2009.

[86] J. Jin, *The Finite Element Method in Electromagnetics*. Wiley, 1993.

[87] E. Palik, *Handbook of Optical Constants of Solids*. Elsevier Science, 1998.

[88] M. Davanco, Y. Urzhumov, and G. Shvets, "The complex bloch bands of a 2D plasmonic crystal displaying isotropic negative refraction," *Optics Express*, vol. 15, no. 15, pp. 9681–9691, 2007.

[89] C. Fietz, Y. Urzhumov, and G. Shvets, "Complex k band diagrams of 3D metamaterial/photonic crystals," *Optics Express*, vol. 19, no. 20, pp. 19 027–19 041, 2011.

[90] G. Parisi, P. Zilio, and F. Romanato, "Complex Bloch-modes calculation of plasmonic crystal slabs by means of finite elements method," *Optics Express*, vol. 20, no. 15, pp. 16 690–16 703, 2012.

[91] P. Griffiths and J. De Haseth, *Fourier Transform Infrared Spectrometry.* Wiley, 2007.

[92] R. Kitamura, L. Pilon, and M. Jonasz, "Optical constants of silica glass from extreme ultraviolet to far infrared at near room temperature," *Applied Optics*, vol. 46, no. 33, pp. 8118–8133, 2007.

[93] U. Fano, "Effects of configuration interaction on intensities and phase shifts," *Physical Review*, vol. 124, no. 6, p. 1866, 1961.

[94] A. S. Barker and J. J. Hopfield, "Coupled-optical-phonon-mode theory of infrared dispersion in $BaTiO_3$, $SrTiO_3$, + $KTaO_3$," *Physical Review A-General Physics*, vol. 135, no. 6A, p. 1732, 1964.

[95] D. K. Jacob, S. C. Dunn, and M. G. Moharam, "Design considerations for narrow-band dielectric resonant grating reflection filters of finite length," *Journal of the Optical Society of America A-Optics Image Science and Vision*, vol. 17, no. 7, pp. 1241–1249, 2000.

[96] J. O. Grepstad, M. M. Greve, B. Holst, I. R. Johansen, O. Solgaard, and A. Sudbo, "Finite-size limitations on quality factor of guided resonance modes in 2D photonic crystals," *Optics Express*, vol. 21, no. 20, pp. 23 640–23 654, 2013.

[97] W. Spitzer and H. Y. Fan, "Infrared absorption in $n$-type silicon," *Physical Review*, vol. 108, pp. 268–271, Oct 1957.

[98] C. Waits, B. Morgan, M. Kastantin, and R. Ghodssi, "Microfabrication of 3D silicon MEMS structures using gray-scale lithography and deep reactive ion etching," *Sensors and Actuators A: Physical*, vol. 119, no. 1, pp. 245 – 253, 2005.

[99] Y. C. Shuai, D. Y. Zhao, W. Q. Yang, W. D. Zhou, J. H. Seo, Z. Q. Ma, G. Medhi, R. Peale, W. Buchwald, and R. Soref, "Fano resonance membrane reflectors from mid-infrared to far-infrared," *2011 IEEE Photonics Conference*, pp. 787–788, 2011.